
Development of simulation tools and analysis of a ^{48}Sc and ^{46}Sc calibration source in liquid scintillator based experiments

Diplomarbeit
zur Erlangung des akademischen Grades
Diplom-Physiker

vorgelegt von

Marc Reinhard
geboren am 20.07.1987 in Dresden



Institut für Kern- und Teilchenphysik
Technische Universität Dresden
2014

Eingereicht am 29.08.2014

1. Gutachter: Prof. Dr. Kai Zuber
2. Gutachter: Prof. Dr. Arno Straessner
Betreuerin: Dr. Valentina Lozza

Kurzfassung

Das SNO+ Experiment nutzt den selben Detektor wie das Vorgängerexperiment SNO (Sudbury Neutrino Observatory). Der Detektor besteht aus einer Acrylkugel mit einem Durchmesser von 12 m, die mit 780 Tonnen Flüssigszintillator gefüllt und von etwa 9500 Photomultipliern (PMTs) umgeben ist. Der Ort des Experiments ist eine Nickelmine in Sudbury, Ontario, Kanada. Aufgrund der Lage in 2 km Tiefe (entspricht 6 km Wasser Abschirmung) ist der Myonenfluss deutlich geringer als an der Oberfläche. In dieser Umgebung sind Messungen physikalischer Prozesse mit schwach radioaktivem Untergrund möglich.

Das wichtigste Ziel von SNO+ ist die Suche nach dem neutrinolosen doppelten Betazerfall von ^{130}Te . Dazu wird der Flüssigszintillator mit 0.3% natürlichem Tellur versetzt. Um die Detektoreigenschaften zu untersuchen, ist eine Kalibrierung des Detektors notwendig. Ein Isotop, das für die Kalibrierung verwendet werden soll, ist ^{48}Sc . Die ^{48}Sc Kalibrierquelle wird durch eine (n,p) Reaktion an einem reinen Titanzyylinder mit natürlicher Isotopenzusammensetzung produziert. Für die Neutronenbestrahlung wird ein DT-Generator der TU Dresden verwendet.

Die Kalibrierung des SNO+-Detektors erfolgt durch die 3 Photonen mit einer Summenenergie von 3.3 MeV, die dem Betazerfall von ^{48}Sc folgen. Die Halbwertszeit von 44 h erfordert einen knappen Zeitplan für die Produktion und den Transport der Quelle. Das Design der Quelle wird stark von Anforderungen an Sicherheit und Sauberkeit während des Transports und des Einsatzes beeinflusst.

In dieser Diplomarbeit wird die Produktion von Scandiumisotopen an natürlichem Titan durchgeführt und ausgewertet. Das Quellendesign wird abgeschlossen und mithilfe von Prototypen die Dichtheit der Kapseln, sowie die Durchführbarkeit der Reinigungsverfahren untersucht. Die Kalibrierquelle wird im SNO+-Detektor simuliert, um verschiedene Detektoreigenschaften zu erforschen und die Physik des Detektors besser zu verstehen.

Abstract

The SNO+ experiment uses the same location and detector as SNO (Sudbury Neutrino Observatory). The detector consists of 780 tonnes of liquid scintillator placed in an acrylic sphere of 12 m diameter and is surrounded by about 9500 photomultipliers (PMTs). It is situated in a nickel mine in Sudbury, Ontario, Canada. Due to the location 2 km underground (equivalent to 6 km water shielding) the muon flux is significantly lower compared to surface level. This environment gives the opportunity to measure low background physics processes.

The main goal of SNO+ is the search for the neutrino-less double beta decay of ^{130}Te . For this scope, the liquid scintillator will be loaded with 0.3% natural tellurium.

A calibration is necessary to study the detector response. One of the isotopes that will be used for the calibration is ^{48}Sc . The ^{48}Sc calibration source will be produced by an (n,p) reaction on a natural titanium cylinder. A DT-generator of TU Dresden will be used for the neutron irradiation.

For the calibration of the SNO+ detector the 3 gamma rays with a sum energy of 3.3 MeV following the beta decay of ^{48}Sc will be used. Due to the half life of 44 h a tight schedule for the production and shipping is required. The design of the source is greatly affected by safety and cleanliness requirements when shipping and deploying the source.

In this thesis the production of scandium isotopes in natural titanium are tested and evaluated. The design of the source container is finalized and prototypes are examined to ensure safety and test cleaning procedures. The calibration source is simulated inside the SNO+ detector to study the response for diverse use cases and better understand the physics processes.

Contents

1	Neutrinos	1
1.1	History	1
1.2	Neutrino Oscillations	3
1.3	Dirac and Majorana neutrinos	5
1.4	Beta decay	5
1.5	Double beta decay	8
1.6	Neutrinoless double beta decay	10
1.7	Solar Neutrinos	12
2	The SNO+ Experiment	15
2.1	The SNO+ detector	15
2.2	SNO+ calibration system	19
2.3	Scientific Goals	20
2.4	SNO+ timetable	27
3	Production of scandium isotopes via neutron activation of a titanium target	29
3.1	Motivation and experimental setup	29
3.2	Germanium-detector calibration	31
3.3	Scandium isotopes	35
3.4	Titanium target	37
3.5	Results of the neutron activation campaign	39
4	Test and production of the source container components	47
4.1	Scandium container design and production	47
4.2	Cleaning procedure	50
4.3	Pressure tests	55
4.4	Ink tests	60
5	Calibration source implementation in RAT	63
5.1	SNO+ software: RAT	63
5.2	Development of a geometry tool for the scandium source	65
5.3	Development of a generator tool for the scandium source	69
6	Analysis of simulation data	71
6.1	Simulation of scandium isotopes	71
6.2	^{46}Sc as additional calibration source	74

6.3	Shadowing of ^{46}Sc	77
6.4	Quenching	79
6.5	Birks constant and light yield	82
6.6	Source holder tests	90
6.7	Position dependence	92
7	Conclusion and Outlook	99
A	Appendix	101

List of Figures

1.1	Beta spectrum of tritium. The Q value is 18589.8 ± 1.2 eV [N ⁺ 06].	7
1.2	High energy tail of the tritium beta spectrum. The expected curves for three values of $m_{\nu_e} = (0, 0.3, 1)$ eV are shown.	7
1.3	Mass excess as a function of Z for A=even nuclei. The single and double beta decay for some selected isotopes is shown (masses from [AWT03]).	9
1.4	Feynman graphs for $2\nu 2\beta$ (left) and $0\nu 2\beta$ (right).	10
1.5	Schematic 2 electron energy spectrum for $2\nu 2\beta$ decay (solid line) and $0\nu 2\beta$ decay (dashed line). The $0\nu 2\beta$ peak is not to scale.	11
1.6	On the left frame the proton-proton chain with branching percentages is shown. The right frame shows the CNO cycle (adapted from [A ⁺ 09]).	12
1.7	Solar neutrino fluxes from the proton-proton chain based on the SSM [BPG04].	13
2.1	Sketch of the detector structure of SNO+. The inner and outer H ₂ O shieldings, the PSUP and the AV with the liquid scintillator (LAB) are shown [A ⁺ 13b].	16
2.2	Schematic representation of the calibration source deployment hardware. The deck clean room with umbilical, source tube and glove box above the neck of the AV are shown. Inside the AV, the ropes and anchor blocks with an attached calibration source are indicated (based on [Hel11]).	17
2.3	Drawing of the hold down rope system for the AV filled with LAB [Loz11].	18
2.4	Picture of the SNO+ vessel from May 2014. The neck, the vessel, the hold down rope system and the PMTs are visible [Sin14].	18
2.5	Expected energy spectrum in the $0\nu 2\beta$ peak region with backgrounds in SNO+. The counts are estimated for a 20 % fiducial volume cut, measurement time of 5 years, background tag efficiency of > 99.99 % for ²¹⁴ Bi and 98 % ²⁰⁸ Tl, factor 50 mitigation of ²¹² Bi and ²¹² Po, negligible cosmogenic activation and $m_{0\nu 2\beta} = 200$ meV [Win14].	21
2.6	Relative absorbance of scintillation light by Nd and Te cocktail in LAB as a function of wavelength. The PMT response is added for comparison [FG14].	22
2.7	Expected half life sensitivities for a 0.3 % loading with ^{nat} Te at 90 % CL [FG14].	22

2.8	Survival probability of ν_e over energy. Vacuum and matter dominated energy regions of the solar neutrino spectrum are indicated. The region of the expected pep neutrino signal is shown as a vertical area [A ⁺ 13b] [Loz14b].	23
2.9	Expected number of events / kT-year from pep (blue), CNO (green), ⁷ Be (red) and ⁸ B (orange) solar neutrinos in SNO+ compared to expected backgrounds [Gan12].	24
2.10	Expected rates from geo (yellow) and reactor (green) antineutrinos in SNO+. The geo antineutrinos originate from U (blue line) and Th (red line) decay chains [Dye12].	25
2.11	Simulated energy spectrum from reactor antineutrinos in SNO+. The spectrum is divided into that from all reactors (blue), all except Bruce Nuclear Generating Station (red) and reactors with distances larger than 700 km (yellow). Dotted lines show the spectra without oscillation [Gan12].	26
3.1	Titanium cylinder and probes in position for the irradiation. On the left side the end of the vacuum pipe with the tritium target inside is shown. On the right side another experiment for neutron irradiation was placed. . .	29
3.2	Titanium cylinder placed in a plastic holder before the activation. The number I marks the first niobium probe and below the motor is visible. .	30
3.3	The three aluminum probes (stripes, left) and two niobium probes (disks, middle) for the neutron flux measurement. On the right side the titanium cylinder is shown.	31
3.4	Germanium detector for calibration and measurement. The lead bricks, the black detector cap and the plastic holder for distance adjustments are visible.	32
3.5	Full energy peak efficiency function for a general germanium detector in double logarithmic scale. The germanium detector used for the measurements should follow the trend of this efficiency curve [N ⁺ 08].	33
3.6	Full energy peak efficiency function for 30 mm distance from the detector cap in double logarithmic scale. Hollow data points are without TCS correction (¹³⁷ Cs has a full point because it does not need TCS correction). .	34
3.7	Decay scheme of ⁴⁸ Sc to ⁴⁸ Ti with a half life of 43.7 h [NND14].	36
3.8	Decay scheme of ⁴⁶ Sc to ⁴⁶ Ti with a half life of 83.8 d [NND14].	36
3.9	Decay scheme of ⁴⁷ Sc to ⁴⁷ Ti with a half life of 3.35 d [NND14].	36
3.10	Neutron flux measured in counts of the silicon detector in the neutron hall during the irradiation of the titanium cylinder on 11.04.2014.	37

3.11	Energy dependent intensity of the neutron flux obtained from measurements and simulations. The maximum intensity is at around 15 MeV [Kan14].	38
3.12	Obtained activities for the 889 keV (blue) and 1121 keV (red) gamma line of ^{46}Sc in the three measurements. The expected exponential function for an initial activity of 23.3 Bq (cf. Table 3.8) is shown for comparison.	42
4.1	Prototypes of the outer container (left) and inner container (middle) for the titanium cylinder (right). The sealing O-rings are shown.	47
4.2	Absorbance spectra of pure LAB (blue) compared to O-ring inside LAB (red) after one month of exposure [Ans12].	48
4.3	Drawing of the main components of the calibration source.	48
4.4	Photo of a cross dowel [PV14].	49
4.5	Broken samples after the first ethanol test.	51
4.6	Acrylic sample 3 of Stock TUD before (left) and after the test (right). An increase of opacity is visible.	53
4.7	Sketch of the first design of the pressure chamber [Dom13].	55
4.8	Decrease of the pressure in the chamber over time.	56
4.9	Open pressure chamber with LAB mixture containing PPO and bisMSB. At the center the acrylic outer container is shown.	57
4.10	LAB+PPO+bisMSB on top of the outer container under UV light.	58
4.11	Spots that are seen show the fluorescence light of LAB+PPO+bisMSB on a paper towel under UV light.	58
4.12	Outer container body part with O-ring. Highlights are the O-ring edge, the thread for the lid and the inner edge.	58
4.13	Outer container body part with O-ring and piece of paper towel. No fluorescence is visible on the paper.	58
4.14	Outer container body after the pressure test. The O-ring edge is wet with LAB but all other parts are dry.	59
4.15	Outer container lid after the pressure test. The O-ring edge is wet with LAB but all other parts are dry.	59
4.16	Inner container filled with ink in water.	61
4.17	Inner container lid with slit (left) and plastic rod used for screwing it (right).	61
5.1	Simulated tracks of scintillation photons (green lines) for a 10 keV gamma event inside the LAB filled AV (blue lines).	64

5.2	Scheme of source, containers and holder for illustration. Adjustable position parameters are shown as well. The labels are according to the names in the source code.	66
5.3	Source geometry in 3D projection (left) and view from distance with weight cylinder (right).	67
5.4	Top view (left) and side view (right) of the source container and holder.	69
6.1	Simulated Nhits (PMT hits) spectrum for ^{46}Sc (2.01 MeV), ^{47}Sc (0.16 MeV) and ^{48}Sc (3.33 MeV). 300,000 events were simulated in LAB 6 days after activation.	71
6.2	Simulated Nhits (PMT hits) spectrum for ^{46}Sc (2.01 MeV), ^{47}Sc (0.16 MeV) and ^{48}Sc (3.33 MeV). 300,000 events were simulated in LAB loaded with 0.3 % of natural tellurium 6 days after activation.	72
6.3	^{48}Sc peak with the double Gaussian fit (red) and the two single Gaussians (dashed black) in pure LAB.	73
6.4	Nhits outside the full energy peak with total scintillation energy deposition of less than 3.1 MeV.	73
6.5	^{46}Sc peak with the fit of a linear function and Gaussian (dashed black) as well as their sum (red) in pure LAB.	73
6.6	Simulation of 300,000 events with all scandium isotopes 13 days after activation in LAB. The peak of ^{48}Sc is small compared to ^{46}Sc	75
6.7	Simulation of 300,000 events with all scandium isotopes 13 days after activation in 0.3 % tellurium loaded LAB. The peak of ^{48}Sc is small compared to ^{46}Sc	75
6.8	Comparison of the ^{46}Sc peak position with and without ^{48}Sc background in pure LAB 13 days after the activation.	76
6.9	Simulated ^{46}Sc as point source and with full container. All events from the point source are inside the full energy peak and no shadowing occurred there.	78
6.10	The upper figure shows the simulated ^{46}Sc inside the container with (red) and without screws and cross dowels (blue). In the lower figure the difference of the two spectra is shown for better comparison (the spectrum with screws/cross dowels is subtracted from the one without).	78
6.11	Fitted peak position of the 3 gammas of Sc48 with a sum energy of 3.333 MeV.	79
6.12	Fitted peak position of a single 3.333 MeV gamma.	79

6.13	Fitted peak positions of the 2 gammas of ^{46}Sc compared to that of one hypothetical 2.010 MeV gamma in a contained source in LAB.	81
6.14	Fitted peak positions of the 2 gammas of ^{46}Sc compared to that of one hypothetical 2.010 MeV gamma as a point source in LAB.	81
6.15	Fitted peak positions of the 2 gammas of ^{46}Sc compared to that of one hypothetical 2.010 MeV gamma in a contained source in 0.3 % tellurium loaded LAB.	81
6.16	Fitted peak positions of the 2 gammas of ^{46}Sc compared to that of one hypothetical 2.010 MeV gamma as a point source in 0.3 % tellurium loaded LAB.	81
6.17	Data and fits of the peak of ^{48}Sc with the corrected Nhits. The blue function in the middle is the fit with standard values for the Birks constant and light yield.	83
6.18	Birks constant dependent peak positions with light yield increasing from bottom to top.	84
6.19	Light yield dependent peak positions with the Birks constant increasing from top to bottom.	84
6.20	Linear fit of peak positions over light yield from 0 MeV^{-1} to 11948 MeV^{-1} with a Birks constant of 0.0798 mm / MeV	85
6.21	Linear fit of FWHM over LY with a Birks constant of 0.0798 mm/MeV and 100,000 events per point.	86
6.22	Linear fit of resolution over LY with a Birks constant of 0.0798 mm/MeV and 100,000 events per point.	86
6.23	^{48}Sc peak area of the simulations with minimum (red) and maximum (blue) Birks constant and fit function.	88
6.24	^{46}Sc peak area of the simulations with minimum (red) and maximum (blue) Birks constant and fit function.	88
6.25	^{47}Sc peak area of the simulations with minimum (red) and maximum (blue) Birks constant and fit function.	89
6.26	Nhits spectra of the simulations with minimum (red) and maximum (blue) Birks constant.	89
6.27	Source geometry with holder and weight cylinder.	90
6.28	Peak values relative to the one obtained for a source at (0,0,0) in the Nhits spectra. Results are obtained for different source positions in the detector. Changes along X (top), Y (middle) and Z axis (bottom) for ^{48}Sc and ^{46}Sc in LAB and 0.3 % tellurium loaded LAB are shown.	93

6.29 Peak values relative to the one obtained for a source at (0,0,0) in the reconstructed energy spectra. Results are obtained for different source positions in the detector. Changes along X (top), Y (middle) and Z axis (bottom) for ^{48}Sc and ^{46}Sc in LAB and 0.3 % tellurium loaded LAB are shown.	95
6.30 Deviations of reconstructed peak values from simulated source positions in the detector. Changes along X (top), Y (middle) and Z axis (bottom) for ^{48}Sc and ^{46}Sc in LAB and 0.3 % tellurium loaded LAB are shown. . .	96
A.1 Spectrum of the activated titanium sample measured on 14.04.14. The peaks of the main isotopes are indicated.	101
A.2 Detailed cleaning procedure for the scandium calibration source parts. . .	102

List of Tables

1.1	Best fit result for the oscillation parameters and squared mass differences for normal hierarchy [GG ⁺ 12].	4
1.2	Candidates for double beta decay [Zub12].	9
2.1	Radioactive calibration sources for the SNO+ experiment [Pee13].	19
3.1	Activities of the calibration sources.	33
3.2	Isotopes of natural titanium and their abundances [NND14].	37
3.3	Half lives and gamma energies, with intensities, for the activated isotopes visible to the SNO+ detector [NND14].	38
3.4	Half lives and main gamma energies with intensities for the activated isotopes for the neutron flux measurement [NND14].	39
3.5	Activities for each gamma line of the activated nuclides. The detector live time was 60.62 min. Measurement date: 14.04.14.	40
3.6	Activities for each gamma line of the activated nuclides. The detector live time was 121.17 h. Measurement started: 17.04.14.	41
3.7	Activities for each gamma line of ⁴⁶ Sc. The nuclides ⁴⁸ Sc, ⁴⁷ Sc and ⁴⁷ Ca were already decayed or the peak areas showed high statistical uncertainties 29 days after the activation. The detector live time was 167.02 h. Measurement started: 08.05.14.	41
3.8	Average activities combining all three measurements of the titanium cylinder and all available gamma energies for each nuclide. The 175 keV line of ⁴⁸ Sc was not included.	43
3.9	Average activities at a hypothetical 7 cm distance from the detector cap. Expected activities after 6 days are shown as well (see text).	43
3.10	Specific activities of the aluminum and niobium probes calculated for the end of irradiation (11.04.). Measurement date: 14.04.14.	44
3.11	Total neutron intensities obtained with the aluminum and niobium probes.	45
4.1	Results of the first test samples for different possible cleaning steps.	51
4.2	Results of the second test samples (14 mm diameter and 3 mm thickness) with different cleaning conditions.	52
4.3	Fit parameters for the double exponential fit function of the measured pressure decrease.	56
4.4	Results of the pressure tests.	59
6.1	Fit parameters with errors for the function in Equation 6.2 and χ^2 / ndf. The function fits the ⁴⁶ Sc peak in Figure 6.5.	74

6.2	Fit parameters with errors for the function in Equation 6.1 and χ^2 / ndf . The function fits the ^{48}Sc peak in Figure 6.3.	74
6.3	Peak positions and FWHMs obtained from the simulations of a point source and a contained source with and without screws and cross dowels.	77
6.4	Fit results of Sc48 compared to a hypothetical 3.333 MeV gamma.	80
6.5	Peak positions and FWHMs of the Nhits spectra of ^{46}Sc as point and contained source in LAB and 0.3 % tellurium loaded LAB for quenching study.	80
6.6	Birks constant and light yield values for the simulations.	82
6.7	Parameters from linear fits of peak positions over light yield in the ranges $(0 - 11948) / \text{MeV}^{-1}$ and $(9652 - 11948) / \text{MeV}^{-1}$	85
6.8	Birks constant and light yield values with calculated and fitted peak positions for the three scandium isotopes. The peaks are calculated from the linear functions in Figure 6.19 (peak _c).	87
6.9	Energy deposition, peak positions and FWHMs for different holder lengths.	91
6.10	Fraction of Nhits inside the two full energy peaks of ^{48}Sc	91
6.11	Distances from the center of the detector along X, Y and Z axis for the position simulations. The center position at $(0.0, 0.0, 0.0)$ was simulated as well.	92
6.12	Absolute peak value in the Nhits and energy reconstruction spectra for central source position in the detector.	94
6.13	Deviations of reconstructed peak values from simulated source positions in the center of the detector at $(0,0,0)$	97

1 Neutrinos

1.1 History

At the beginning of the 20th century three types of radioactive decay were known. The alpha, beta and gamma decay were all expected to be a two body decay, where the energy of the emitted particles corresponds to the energy level difference between the two involved nuclei. Experimental results met the expectation for the alpha and gamma decay. The measured spectra showed discrete lines broadened by the detector resolution. However, the measurements of the beta decay showed a continuum ranging from zero up to the endpoint energy of the specific nuclide. In addition the spin of the nucleus changed by an integer value while it was known that the electron released in the decay has a spin of $1/2$. The experiments seemed to break the fundamental rules of energy and angular momentum conservation.

Many unsuccessful attempts were made to solve that problem e.g. by trying to measure the missing energy or claiming that the energy conservation law is only statistically valid for beta decay. In 1930 Pauli postulated an electrically neutral and very weakly interacting particle that was emitted together with the electron in the beta decay. He called this particle neutron [Pau30]. The beta decay is then a three body decay, consisting of nucleus, electron and the newly postulated almost undetectable particle with a spin of $1/2$. The three body decay can explain the measured spectral shape and the angular momentum was also conserved. Fermi developed a theory for the beta decay four years later [Fer34], where Pauli's new particle is considered massless as well as chargeless and called by its final name "neutrino" which is Italian for "little neutral one". The original name "neutron" is today used for a heavier neutral particle discovered in 1932 by Chadwick [Cha32].

Cowan and Reines were the first to succeed in the direct detection of the neutrino in 1956 [J+56]. They used the unique signature of a neutron and a positron following the inverse beta decay of antineutrinos on the protons of hydrogen. In todays notation the reaction at nuclear level is:

$$\bar{\nu}_e + p \rightarrow n + e^+ \quad (1.1)$$

with $\bar{\nu}_e$ being the electron antineutrino. A nuclear reactor was used as a strong source for $\bar{\nu}_e$. Shortly after that another kind of neutrino was discovered by Lederman, Schwartz and Steinberger which is today known as the muon neutrino [D+62]. With the discovery of the third heavy lepton in 1975 [P+75] called the tauon, a third neutrino type was

expected to exist. The tau neutrino was discovered in 2000 [Kod01]. A total of three known neutrino flavors exist, matching the three known charged leptons.

Neutrinos are constantly created by nuclear fusion reactions in the Sun. Among the several reactions happening, one that emits high energetic neutrinos with energies up to around 15 MeV, is the following:



The emitted neutrinos are called ${}^8\text{B}$ neutrinos. Solar neutrinos have been used to test the prediction of the Standard Solar Model (SSM). The main difficulty in the measurement of neutrinos is the small interaction cross section with matter. Large detector volume and masses as well as background suppression were necessary to discriminate the expected signal from the background. Detectors were generally placed in mines or tunnels to reduce the muon induced background.

The first results e.g. from the Homestake experiment showed a neutrino flux smaller than predicted by the SSM. The discrepancy between the SSM predictions and the experimental results became known as the solar neutrino problem.

A crucial experiment contributing to the solution was the Sudbury Neutrino Observatory (SNO). The detector consisted of 1 kt D_2O and is located in the Creighton nickel mine in Ontario (Canada) at a depth of 2 km. ${}^8\text{B}$ neutrinos were detected in the heavy water by three different reactions. A neutral current reaction (NC) where a neutrino dissociates the deuterium nucleus:

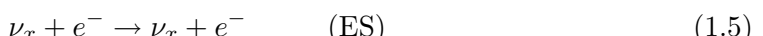


The reaction is equally sensitive to all 3 flavor neutrinos.

A charged current reaction (CC), induced only by an electron neutrino, in which the neutron of the deuterium is converted into an electron and proton:



and an electron scattering reaction (ES):



The cross section of the ES reaction is larger for the ν_e than for ν_μ or ν_τ by a factor of about 6.

The flux measured by the NC reaction was consistent with the SSM prediction, however the ratio of CC/NC was found equal to around 0.3 [Che11]. It was clear that something

happened to the ν_e while travelling from the source to the detector. The same results were obtained by the Super-Kamiokande (SK) experiment with ES reactions. Among the theories developed to explain the solar neutrino problem and the results of SNO and SK, the preferred one was the neutrino oscillation. In neutrino oscillation theory neutrinos can arrive at the Earth with a different flavor with respect to their production.

1.2 Neutrino Oscillations

After SNO and SK, other experiments confirmed that neutrinos oscillate from source to detector. An important consequence of this behavior is that neutrinos must have a non-negligible mass, unlike what is predicted by the standard model of particle physics where they are considered massless.

In the oscillation scenario the flavor and mass eigenstates are connected by a mixing matrix. This was already known for the quark sector. When a neutrino originates in a decay, it has a well defined flavor eigenstate, which is obtained as superposition of its mass eigenstates:

$$|\nu_\alpha\rangle = \sum_i U_{\alpha i} |\nu_i\rangle \quad (1.6)$$

where $|\nu_i\rangle$ ($i = 1, 2, 3$) is the mass eigenstate, $|\nu_\alpha\rangle$ ($\alpha = e, \mu, \tau$) is the flavor eigenstate and $U_{\alpha i}$ is the mixing matrix. The Pontecorvo-Maki-Nakagawa-Sakata (PMNS) matrix is a 3×3 unitary matrix [Zub12]:

$$U = \begin{pmatrix} c_{12}c_{13} & s_{12}c_{13} & s_{13}e^{-i\delta} \\ -s_{12}c_{23} - c_{12}s_{23}s_{13}e^{i\delta} & c_{12}c_{23} - s_{12}s_{23}s_{13}e^{i\delta} & s_{23}c_{13} \\ s_{12}s_{23} - c_{12}s_{23}s_{13}e^{i\delta} & -c_{12}s_{23} - s_{12}c_{23}s_{13}e^{i\delta} & c_{23}c_{13} \end{pmatrix} \quad (1.7)$$

with $c_{ij} \triangleq \cos(\theta_{ij})$, $s_{ij} \triangleq \sin(\theta_{ij})$ and δ the CP-violating phase.

It depends on three mixing angles (θ_{12} , θ_{13} and θ_{23}) and a CP-violating phase (δ) that is non-zero if neutrino oscillations violate the CP symmetry. Generally, experimental observations are explained by a 2×2 matrix with an error of up to a few percent [Zub12]. In this case only one mixing angle θ remains and there is no CP-violating phase:

$$\begin{pmatrix} \nu_\alpha \\ \nu_\beta \end{pmatrix} = \begin{pmatrix} \cos \theta & \sin \theta \\ -\sin \theta & \cos \theta \end{pmatrix} \begin{pmatrix} \nu_1 \\ \nu_2 \end{pmatrix}. \quad (1.8)$$

The probability that a neutrino is detected with a flavor different from the original one depends on its energy E and the distance L between source and detector ($\hbar = c = 1$) [Zub12]:

$$P(\nu_\alpha \rightarrow \nu_\beta) \cong \sin^2 \left(\frac{\Delta m_{ij}^2}{4} \frac{L}{E} \right) \cdot \sin^2(2\theta) \quad (1.9)$$

where $\Delta m_{ij}^2 = |m_i^2 - m_j^2|$ is the difference of the squared masses of the two mass eigenstates, which must be greater than zero to allow oscillation. In equation 1.9 the first term describes the oscillation while the second term describes the amplitude of the oscillation.

The location of the maxima and minima of the oscillation depends on the value of Δm_{ij}^2 and the ratio of L/E . Experiments are generally - if possible - located at a maximum or minimum in order to study the oscillation parameters.

Diverse neutrino sources are used to constrain the parameters: Solar ν_e , atmospheric ν_μ , nuclear reactor $\bar{\nu}_e$, accelerator ν_μ and $\bar{\nu}_\mu$. Solar electron neutrinos are generally used to study the (1,2) sector, atmospheric neutrinos for the (2,3) sector and reactor antineutrinos for the (1,3) sector. Since only mass differences and no absolute masses are known from the oscillation studies, there are two possible mass hierarchies for the neutrino masses, which cannot be distinguished yet. In the normal hierarchy the order is $m_1 < m_2 < m_3$ and in the inverted hierarchy it is $m_3 < m_1 < m_2$. The mixing angles and Δm_{ij}^2 for the normal hierarchy case are given in Table 1.1:

Table 1.1: Best fit result for the oscillation parameters and squared mass differences for normal hierarchy [GG⁺12].

Parameter	Best fit	1σ range
$\sin^2 \theta_{12}$	0.302	0.290 - 0.315
$\sin^2 \theta_{23}$	0.413 or 0.594	0.388 - 0.450 or 0.572 - 0.615
$\sin^2 \theta_{31}$	0.0227	0.0203 - 0.0250
$\frac{\Delta m_{21}^2}{10^{-5} eV^2}$	7.50	7.31 - 7.68
$\frac{\Delta m_{31}^2}{10^{-3} eV^2}$	2.473	2.406 - 2.543
$\frac{\Delta m_{32}^2}{10^{-3} eV^2}$	-2.427	-2.492 - -2.380

Since θ_{13} was found to be small but non-zero, it will be difficult but possible to measure δ , the CP-violating phase, as well. The Tokai to Kamioka (T2K) experiment is aiming for that.

1.3 Dirac and Majorana neutrinos

Most standard model particles are Dirac particles. For Dirac particles a transformation under C-conjugation inverts the charge (Q) which allows a distinction of particle and antiparticle. Such a distinction is not obvious for the neutrino, which means that it could be its own antiparticle. A theory for particles that are their own antiparticles was proposed in 1937 by Majorana [Maj37] and particles with this property are called Majorana particles.

For Majorana neutrinos there are two additional phases α and β appearing in the PMNS matrix (1.7):

$$U_{Maj} = U_{PMNS} \cdot \begin{pmatrix} 1 & & \\ & e^{i\alpha} & \\ & & e^{i\beta} \end{pmatrix} \quad (1.10)$$

From neutrino oscillations we know that neutrinos have a mass, which can only be described by theories beyond the standard model. If the neutrino is a Majorana particle it could help understanding why the neutrino mass is so much smaller than that of the lightest charged lepton. Another effect is lepton number violation occurring in the neutrinoless double beta decay (see section 1.6).

A direct measurement of that decay would determine the Dirac or Majorana nature of the neutrino.

1.4 Beta decay

The radioactive beta decay describes the process of an unstable nucleus emitting an electron (positron) together with an antineutrino (neutrino). Depending on a neutron excess or deficit compared to stable isotopes, two kinds of beta decay, namely β^- and β^+ , are possible. In the case of β^- decay one of the neutrons (n) of the mother nucleus (N) decays into a proton (p), decreasing the neutron number and increasing the proton number (Z) of the daughter nucleus (N') by one. The Q value of the decay is the mass difference between the neutron and the proton and the binding energy difference of the two atoms. With this energy the electron (e^-) and the electron antineutrino ($\bar{\nu}_e$) are produced and the rest is transformed into their kinetic energy. The mass number (A) stays the same. Considering the negligible $\bar{\nu}_e$ -mass this reads as:

$$Q_{\beta^-} = m(A, Z) - m(A, Z + 1) - m(e^-) \quad (1.11)$$

On the parton level, one of the down quarks (d) of the neutron changes into an up quark (u) which becomes part of the proton. The notations of β^- decay at the nucleus (a), nucleon (b) and parton (c) level are:

$${}_{\text{Z}}^{\text{A}}\text{N} \rightarrow {}_{\text{Z}+1}^{\text{A}}\text{N}' + e^- + \bar{\nu}_e \quad (1.12\text{a})$$

$$\text{n} \rightarrow \text{p} + e^- + \bar{\nu}_e \quad (1.12\text{b})$$

$$\text{d} \rightarrow \text{u} + e^- + \bar{\nu}_e \quad (1.12\text{c})$$

In the β^+ decay a proton decays into a neutron, a positron (e^+) and an electron neutrino (ν_e). At the parton level, the up quark of the proton changes into a down quark for the neutron. The notations of β^+ decay at the nucleus (a), nucleon (b) and parton (c) level are:

$${}_{\text{Z}}^{\text{A}}\text{N} \rightarrow {}_{\text{Z}-1}^{\text{A}}\text{N}' + e^+ + \nu_e \quad (1.13\text{a})$$

$$\text{p} \rightarrow \text{n} + e^+ + \nu_e \quad (1.13\text{b})$$

$$\text{u} \rightarrow \text{d} + e^+ + \nu_e \quad (1.13\text{c})$$

In contrast to the free neutron decay via β^- , the proton decay can only happen inside a nucleus.

Another possible decay is the electron capture (EC). The nucleus captures an e^- from the shell instead of releasing a positron:

$$e^- + {}_{\text{Z}}^{\text{A}}\text{N} \rightarrow {}_{\text{Z}-1}^{\text{A}}\text{N}' + \nu_e \quad (1.14\text{a})$$

$$e^- + \text{p} \rightarrow \text{n} + \nu_e \quad (1.14\text{b})$$

$$e^- + \text{u} \rightarrow \text{d} + \nu_e \quad (1.14\text{c})$$

Depending on the binding energies of the parent and daughter nucleus the β^+ and EC decays may occur within the same nuclide.

The shape of the allowed beta decay spectrum is described by the following equation [Zub12]:

$$\frac{d^2N}{dt dE} = C \cdot F(E, Z + 1) \cdot pE \cdot \sqrt{(E_0 - E)^2 - m_{\nu_e}^2} \cdot (E_0 - E) \quad (1.15)$$

where E_0 is the energy difference between the initial and final state of the nucleus, p and E are the momentum and energy of the electron, C is a constant, $F(E, Z + 1)$ is the Fermi function [Fer34], m_{ν_e} is the neutrino mass and $E_0 > E + m_{\nu_e}$. In Figure 1.1 a beta decay spectrum is shown.

In order to measure the m_ν , a kinematic experiment can be performed. When measuring the beta decay spectrum, the mass of the neutrino is missing in the energy of every event. This gives the possibility to determine the neutrino mass by measuring the tiny gap of missing energy at the end of the spectrum if the Q value of the reaction is precisely known. An isotope with a reasonable small Q value, and therefore good potential to measure that gap, is tritium. The current upper limit for the neutrino mass determined with tritium decay is $m_{\nu_e} < 2$ eV (95 % C. L.) [Y⁰⁶] and was measured by the Mainz Neutrino Mass Experiment. An experiment improving this limit is the KATRIN experiment (acronym for “Karlsruhe Tritium Neutrino experiment”). In Figure 1.2 the shape of the high energy tail of the beta spectrum is shown for three different neutrino masses.

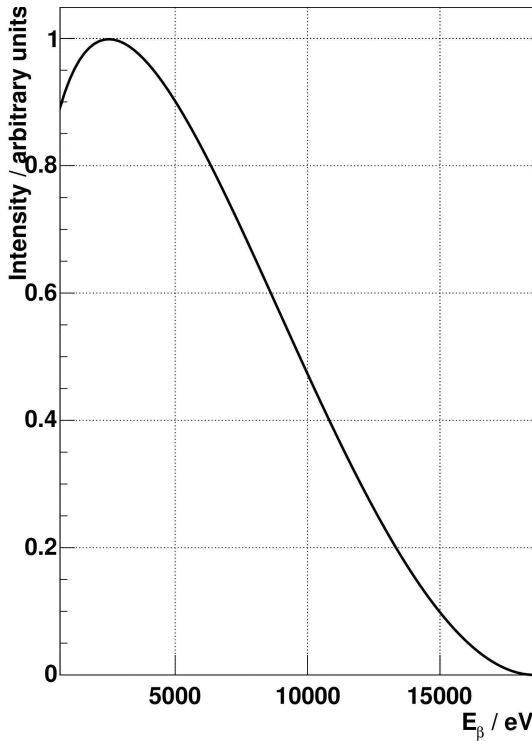


Figure 1.1: Beta spectrum of tritium. The Q value is 18589.8 ± 1.2 eV [N⁰⁶].

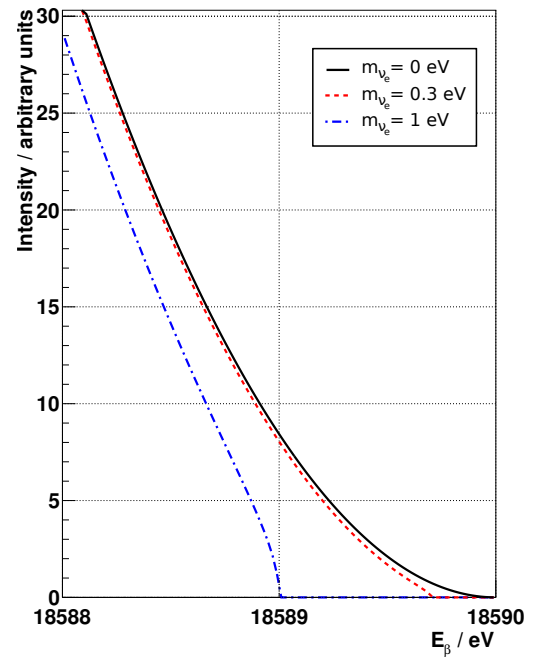
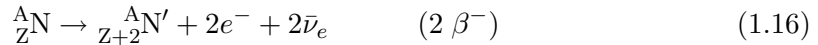


Figure 1.2: High energy tail of the tritium beta spectrum. The expected curves for three values of $m_{\nu_e} = (0, 0.3, 1)$ eV are shown.

1.5 Double beta decay

The double beta decay is the de-excitation of a nucleus through two beta decays at the same time which means that the number of protons Z changes by two units while the atomic mass A stays the same. It occurs only for isotopes with even numbers of protons and neutrons (even/even nuclei) and when the single beta decay is forbidden or strongly suppressed. For the double β^- decay this reads as:



Like in the single beta decay, the double β^+ decay is also competing with the process of orbital electron capture:



The binding energy B of a nucleus is described by the semiempirical Bethe-Weizsäcker formula [vW35]. For constant A , this formula is written as:

$$B \propto aZ^2 + bZ + c + \delta \quad (1.20)$$

The pairing term δ depends on the neutron and proton numbers as follows:

$$\delta = \begin{cases} -\frac{12 \text{ MeV}}{A^{1/2}} & \text{even-even nucleus} \\ 0 \text{ MeV} & \text{even-odd nucleus} \\ \frac{12 \text{ MeV}}{A^{1/2}} & \text{odd-odd nucleus} \end{cases} \quad (1.21)$$

For even A there are two parabolas separated by 2δ . This is shown in Figure 1.3, where the upper parabola is for odd/odd nuclei and the lower one for even/even nuclei.

For some nuclei (e.g. ${}^{130}\text{Te}$ to ${}^{130}\text{I}$ for β^-), the single beta decay is forbidden or strongly suppressed, because the daughter nucleus has a higher mass. The decay in this case can proceed via a double beta decay. This will allow a measurement of the double beta decay spectrum without the background of single beta decay.

To perform the measurements, isotopes with high Q values are chosen, because their half lives are shorter, which gives a stronger signal. Natural radioactive backgrounds are

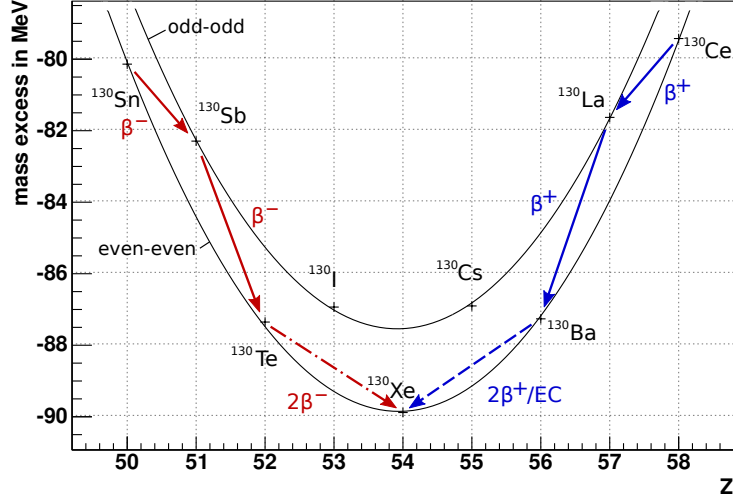


Figure 1.3: Mass excess as a function of Z for A=even nuclei. The single and double beta decay for some selected isotopes is shown (masses from [AWT03]).

also lower in higher energy regions. Out of 35 isotopes known to have the configuration for double beta decay, 11 are interesting for investigation because of their relatively high Q values (above 2 MeV):

Table 1.2: Candidates for double beta decay [Zub12].

Isotope	Q value/keV	Abundancy/%	$T_{1/2}/10^{24}$ yrs
⁴⁸ Ca	4274 ± 4	0.19	> 4.10
⁷⁶ Ge	2039.04 ± 0.16	7.8	> 40.9
⁸² Se	2995.5 ± 1.3	9.2	> 9.27
⁹⁶ Zr	3347.7 ± 2.2	2.8	> 4.46
¹⁰⁰ Mo	3034.40 ± 0.17	9.6	> 5.70
¹¹⁰ Pd	2004 ± 11	11.8	> 18.6
¹¹⁶ Cd	2809 ± 4	7.5	> 5.28
¹²⁴ Sn	2287.8 ± 1.5	5.6	> 9.48
¹³⁰ Te	2527.01 ± 0.32	34.5	> 5.89
¹³⁶ Xe	2457.83 ± 0.37	8.9	> 5.52
¹⁵⁰ Nd	3367.7 ± 2.2	5.6	> 1.25

1.6 Neutrinoless double beta decay

The neutrinoless double beta decay ($0\nu2\beta$) is a possible but not yet observed special case of the double beta decay. It can happen if the neutrino is a Majorana particle. This process violates the total lepton number by two units because no neutrino appears in the final state:

$${}^A_Z N \rightarrow {}^A_{Z+2} N' + 2e^- \quad (1.22)$$

The Feynman diagrams for the $2\nu2\beta$ and the $0\nu2\beta$ decay are shown in Figure 1.4.

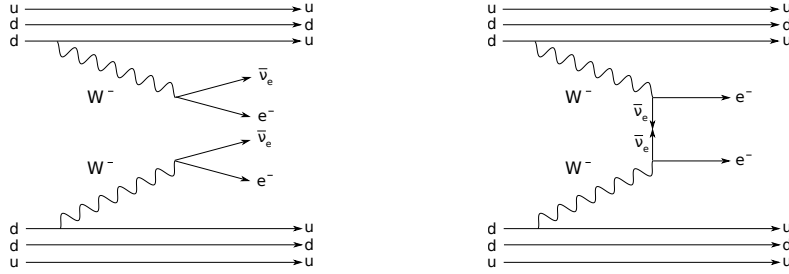


Figure 1.4: Feynman graphs for $2\nu2\beta$ (left) and $0\nu2\beta$ (right).

While the two-neutrino double beta decay ($2\nu2\beta$) is a 5 body decay (including the nucleus), $0\nu2\beta$ is a 3 body decay. The latter gives the possibility of experimentally testing for the absence of the neutrinos. Because of momentum conservation the nucleus gets a very small fraction of the total energy. The rest is distributed between the two electrons. If that decay exists, there will be a peak at the endpoint energy of the two electron spectrum that results from the $2\nu2\beta$ decay.

The shape of the $2\nu2\beta$ spectrum is shown in Figure 1.5. It can be approximated by the following parametrization [Zub12]:

$$\frac{dN}{dK} \approx K(Q - K)^5 \left(1 + 2K + \frac{4K^2}{3} + \frac{K^3}{3} + \frac{K^4}{30} \right) \quad (1.23)$$

with K being the sum energy of the two electrons and Q the endpoint energy of the reaction. The half life for $0\nu2\beta$ can be described by [Zub12]:

$$(T_{1/2}^{0\nu})^{-1} = G^{0\nu}(Q, Z) \cdot |M_{GT}^{0\nu} - M_F^{0\nu}|^2 \cdot \left(\frac{\langle m_{\nu_e} \rangle}{m_e} \right)^2 \quad (1.24)$$

with the phase space integral $G^{0\nu}$ and the two nuclear matrix elements $M_{GT}^{0\nu}$ and $M_F^{0\nu}$, for Gamov-Teller and Fermi transitions respectively. The effective Majorana mass of the

neutrino $\langle m_{\nu_e} \rangle$ consists of the mixed three mass eigenstates [Zub12]:

$$\langle m_{\nu_e} \rangle = |m_1 U_{e1}^2 \pm m_2 U_{e2}^2 \pm m_3 U_{e3}^2| \quad (1.25)$$

where the two Majorana CP-phases from (1.7) are ± 1 if CP-symmetry is conserved. As shown in Equation (1.24), neutrino mass limits can be derived from better limits on the half-life of $0\nu 2\beta$. Currently the best $0\nu 2\beta$ half-life limits are of the order of 10^{25} yr.

From a theoretical point of view, the larger challenge is the definition of the nuclear matrix elements $M_{\text{GT}}^{0\nu}$ and $M_{\text{F}}^{0\nu}$, as well as the phase-space factor $G^{0\nu}$. Using the nuclear matrix elements from A. Staudt et al. [SMKK90] an electron neutrino mass of 0.32 ± 0.03 eV was obtained by the Heidelberg-Moscow experiment [Zub12]. The neutrino mass was derived from the measurement of the $0\nu 2\beta$ decay of ^{76}Ge . Klapdor's claim for the observation of the $0\nu 2\beta$ decay seems to be excluded by the GERDA experiment [A⁺13a] and is controversially discussed.

The β^+ equivalent of the $0\nu 2\beta$ decay:

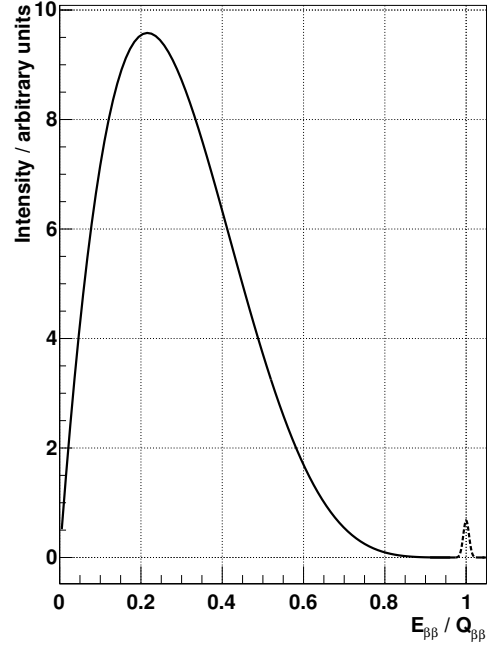
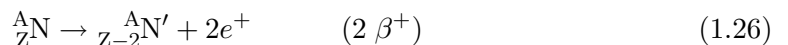


Figure 1.5: Schematic 2 electron energy spectrum for $2\nu 2\beta$ decay (solid line) and $0\nu 2\beta$ decay (dashed line). The $0\nu 2\beta$ peak is not to scale.



corresponds to the double beta decay on the right side of Figure 1.3.

These decays are more difficult to investigate experimentally because of even longer half lives. The ECHo experiment explores the single EC of ^{163}Ho through a calorimetric approach [Gas13]. This provides an alternative way for probing neutrino properties.

1.7 Solar Neutrinos

The Sun is producing its energy by fusion of hydrogen to helium. The main process is the proton-proton chain which describes the necessary reactions on the way from single protons to helium. Five of these processes release neutrinos with different energies (cf. Figure 1.6).

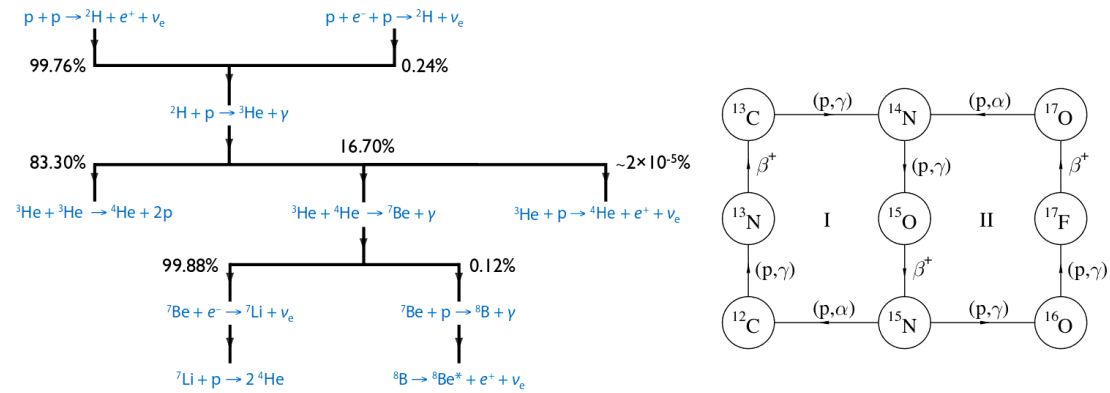


Figure 1.6: On the left frame the proton-proton chain with branching percentages is shown. The right frame shows the CNO cycle (adapted from [A⁺09]).

Due to the different kinematics of the reactions, neutrinos are produced monoenergetic or with broad energy spectra. In Figure 1.7 the expected ν flux, based on the SSM, as a function of ν energies is shown for the neutrinos of the proton-proton chain. The different ν spectra are labeled according to their respective production reactions (e.g. ^8B for neutrinos produced in the ^8B decay).

Because of the energy production in the proton-proton chain via the general reaction:

$$4p + 2e^- \rightarrow {}^4\text{He} + 2\nu_e + 26.7 \text{ MeV} \quad (1.29)$$

only electron neutrinos are produced. As anticipated in Section 1.1, the measurement of a smaller ν_e flux than expected by the SSM lead to the solar neutrino problem.

In the Sun, neutrinos are also produced by the CNO-cycle. This process is less probable than the proton-proton chain and produces only 1.6 % of the total energy in the Sun [Nau11]. Like the proton-proton chain, the CNO cycle produces helium from single protons as well, but it uses isotopes of the heavier elements carbon, nitrogen, oxygen and fluor as catalysts. ^{12}C converts via (p, γ) reactions and β^+ decays to ^{15}N in cycle I and ^{15}N builds up to ^{17}O in cycle II as shown in Figure 1.6. From ^{15}N and ^{17}O the

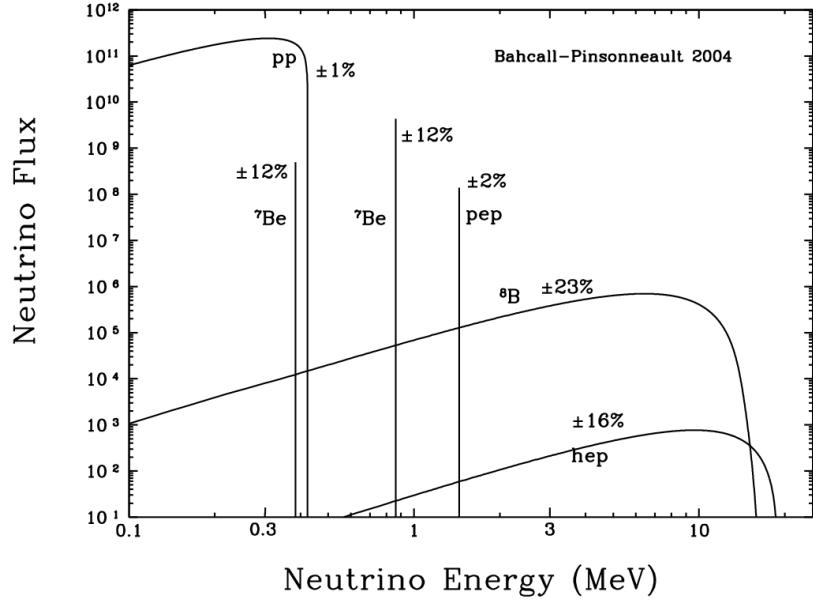


Figure 1.7: Solar neutrino fluxes from the proton-proton chain based on the SSM [BPG04].

alpha particles are emitted.

Neutrinos emitted in the β^+ decays of the solar CNO cycle could be used to probe the solar metallicity, which is the amount of heavy elements in the Sun. However, the weaker flux and the larger uncertainty on the production cross section make this measurement very challenging.

2 The SNO+ Experiment

2.1 The SNO+ detector

SNO+ is the follow up experiment of the Sudbury Neutrino Observatory (SNO) and is therefore reusing the location, detector, and some of the equipment of SNO. It is situated in a cavity that is part of a laboratory (SNOLAB) which lies about 2000 m beneath the surface inside the Creighton nickel mine in Sudbury, Ontario, Canada. The shielding is equivalent to about 6000 m water and ensures low backgrounds from atmospheric muons. The target volume of the detector is a sphere of 12 m diameter inside an acrylic vessel (AV) with a wall thickness of 5 cm. SNO+ will be a liquid scintillator detector, which will have a lower energy threshold compared to SNO because of the higher light yield. However, the information about the direction of the reacting particle will be lost. 780 tonnes of liquid scintillator will be filled in the AV. Around the AV about 9500 photomultiplier tubes (PMTs) are placed in the PMT support structure (PSUP). They cover about 54 % of the area and measure the scintillation light produced in the target volume (cf. Figure 2.1) [B⁺⁰⁰].

To reach high sensitivities in the proposed measurements a background reduction is crucial. The main sources of radioactivity are the natural U and Th chains as well as ^{40}K and neutrons. Isotopes in the U and Th chain emit α , β and γ radiation. A neutron background is produced via secondary nuclear reactions such as (α, n) or (γ, n) and from fission reactions. For shielding from radiation coming from the surrounding rock, the whole cavity will be filled with 7 kt of ultrapure water which has a high cross section for neutron capture. Additionally a radon tight layer is placed over the rock to suppress radon emanation into the water.

Facing outwards, some PMTs are searching for radiation that originates outside the detector and therefore causes Čerenkov light in the surrounding water. This provides a veto to identify backgrounds such as high energy muons.

Although the materials were carefully chosen with respect to their purity levels in U, Th and K, all parts of the detector are sources of background radiation. The water between the PSUP and the AV is shielding the active volume against radiation emitted by decays in the PSUP. The SNO+ experiment will use a U and Th purification system for the liquid scintillator based on distillation and with N_2 steam stripping Rn, Ar and Kr are removed [F⁺¹¹]. Background levels comparable to those of the initial Borexino experiment ($2 \cdot 10^{-17} \text{ g U/g}$ and $7 \cdot 10^{-18} \text{ g Th/g}$) are expected [A⁺⁰⁸].

The inside of the AV can be accessed via the neck, where also the calibration sources are

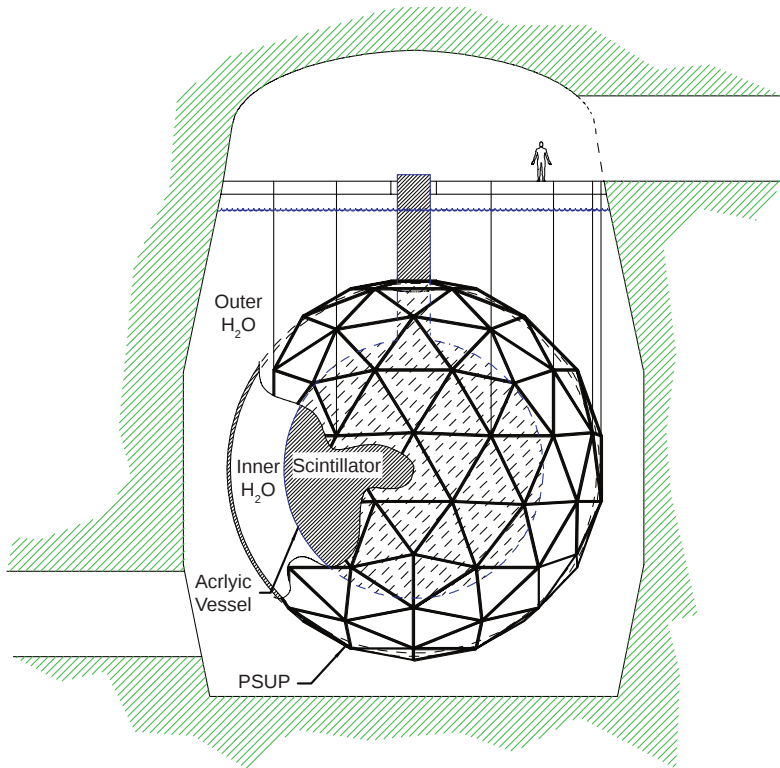


Figure 2.1: Sketch of the detector structure of SNO+. The inner and outer H_2O shieldings, the PSUP and the AV with the liquid scintillator (LAB) are shown [A⁺13b].

going through. The clean room on top of the neck ensures minimal radioactive contamination at the entrance. The calibration sources will be connected using an umbilical and a set of ropes to be moved inside the detector. When not in use, the calibration sources will be stored in a glove box on the top of the detector. The umbilical will provide all the necessary feeding lines (HV, output cables). The central rope carries the weight while the side ropes enable the movement of the sources in the AV via the connection to the anchor blocks. The ropes are operated by motors from the umbilical retrieval mechanism. A sketch of the source deployment hardware is shown in Figure 2.2.

One or more LEDs are additionally attached to the sources. The light from the LEDs is detected by 6 cameras that are distributed on the PSUP for position information. An error on the position as small as 1 cm can be achieved [Sin13b]. Using the umbilical system with the anchor blocks on the side of the vessel, the sources can reach a large fraction of the AV volume.

In SNO+ Linear Alkylbenzene (LAB) will be used as liquid scintillator charged with

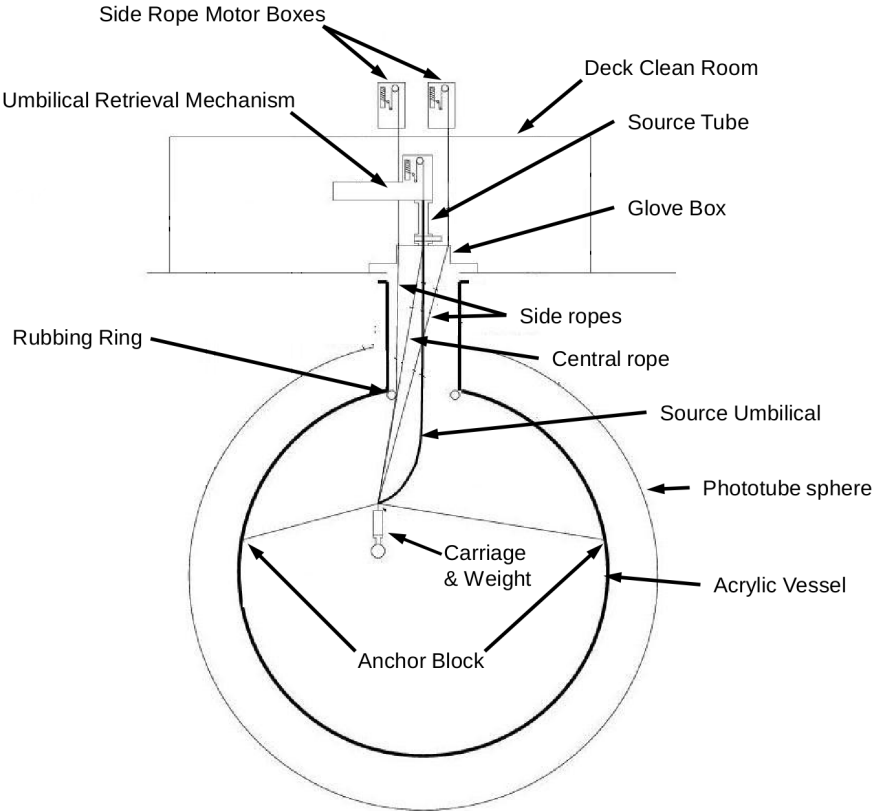


Figure 2.2: Schematic representation of the calibration source deployment hardware. The deck clean room with umbilical, source tube and glove box above the neck of the AV are shown. Inside the AV, the ropes and anchor blocks with an attached calibration source are indicated (based on [Hel11]).

2 g/l of 2.5-Diphenyloxazole (PPO) as wavelength shifter. LAB has chemical properties similar to mineral oil, such as good optical transparency and a high flash point. It is also compatible with the acrylic of the vessel and has a high light yield. Another important advantage is that it is commercially available, which makes it relatively cheap and easily accessible in the required amount [SNO14b]. With LAB as liquid scintillator, the light yield of SNO+ will be about 50 times higher than that of SNO with Čerenkov light. This will allow the detection of reactions with lower energies, such as solar pep or CNO neutrinos.

When the acrylic vessel was filled with D₂O for the SNO experiment, it was held up by a system of ropes because it was heavier than the surrounding light water. The LAB used in SNO+ has a density of (0.849 ± 0.005) g/cm³ at 24 °C [O'K09]. Since the AV

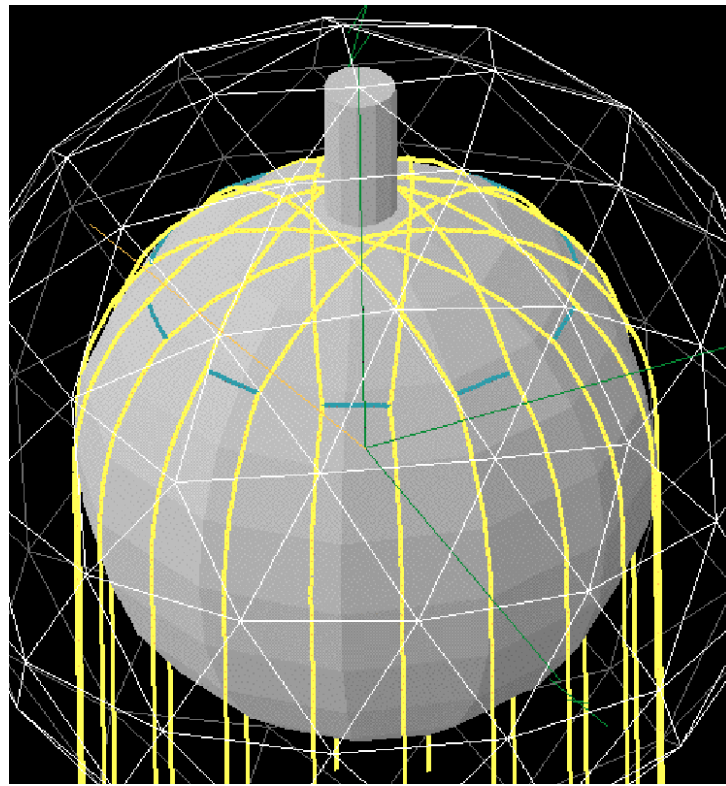


Figure 2.3: Drawing of the hold down rope system for the AV filled with LAB [Loz11].



Figure 2.4: Picture of the SNO+ vessel from May 2014. The neck, the vessel, the hold down rope system and the PMTs are visible [Sin14].

filled with LAB will be lighter than water, a hold down rope system was installed in 2012 which is shown as a sketch in Figure 2.3. A picture of the vessel and the installed rope system is shown in Figure 2.4.

2.2 SNO+ calibration system

The calibration of the SNO+ detector will be done with optical and radioactive sources and it is necessary to understand the detector response. As optical sources the Embedded LED/laser Light Injection Entity (ELLIE) as well as a laserball will be used. The ELLIE hardware is used by AMELLIE which measures the attenuation length of LAB at different wave lengths and by SMELLIE which measures the scattering properties of the detector. TELLIE is responsible for timing, gain and optics [Wat14]. Because ELLIE is installed on the PSUP, continuous calibrations can be done during the whole SNO+ operation. The laserball is a calibration source that needs to be deployed. It emits diffuse quasi-isotropic light with wavelengths between 337 nm and 620 nm and is used to test the overall PMT response [Sin13a].

Table 2.1: Radioactive calibration sources for the SNO+ experiment [Pee13].

Isotope	Energy/MeV	Decay used
^{57}Co	0.1	γ
^{90}Y	2.3	β^-
^{60}Co	2.5	γ
^{48}Sc	3.3	γ
^{24}Na	4.1	γ
AmBe	4.4	n/γ
^{16}N	6.1	γ

For the various physics goals SNO+ is aiming for, it is important to understand the behavior of the detector for different primary particles with different energies and positions. For this reason the radioactive sources listed in Table 2.1 are developed. The γ energies of ^{57}Co at 122 keV and 136 keV will be used to check the response at the trigger threshold. ^{60}Co , ^{24}Na and ^{16}N are designed to be tagged inside their containers which allows to investigate the shape of the detector response signal. Together with the ^{48}Sc they will be used for energy and position calibration. To test the detector response to electrons and neutrons, the β^- source ^{90}Y with endpoint energy of 2.3 MeV and the

AmBe as a neutron source will be used. Additionally a ${}^8\text{Li}$ beta source may be used for a high energy calibration point and studying of Čerenkov light in the presence of scintillation [Was11].

The sources are connected to the umbilical and inserted through the neck of the detector (see section 2.1). A source committee is dedicated to safety and cleanliness of the sources. It ensures that the sources are built safe, solid and tight and are clean when deployed, which minimizes the risk of contamination.

The first calibration was done in an air filled detector with the optical sources. Following calibrations will be done in water, pure LAB and tellurium loaded LAB fills where also the radioactive sources will be used.

2.3 Scientific Goals

2.3.1 Neutrinoless double beta decay

The main goal of the SNO+ experiment is the search for the neutrinoless double beta decay. For this purpose a double beta isotope will be loaded in the LAB. SNO+, as a liquid scintillator detector, will have a poor energy resolution compared to solid state experiments such as CUORE [CUO14] or GERDA [GER14] that are searching for the neutrinoless double beta decay as well. This will be compensated by the deployment of a large mass, which will give a high count rate of double beta decays.

The detector will be loaded with natural tellurium containing the double beta isotope ${}^{130}\text{Te}$ with a Q value of 2.53 MeV. Initially the detector will be loaded with 0.3% ${}^{\text{nat}}\text{Te}$. This corresponds to nearly 800 kg of ${}^{130}\text{Te}$ inside the detector and 160 kg inside a 20% fiducial volume which is a sphere with 3.5 m radius in the center of the detector [Mot14]. The fiducial volume cut reduces the external background sources which are mainly due to the AV radioactivity. For the future loadings up to 3% are under investigation.

Initially SNO+ targeted ${}^{150}\text{Nd}$ as double beta isotope, but after a full review of the collaboration in 2013 it was replaced by ${}^{130}\text{Te}$. The main advantages of ${}^{130}\text{Te}$ are:

- The longer $2\nu2\beta$ half life: the background from the $2\nu2\beta$ decay is 100 times lower than that of ${}^{150}\text{Nd}$.
- With 34.08% the natural abundance of ${}^{130}\text{Te}$ is the highest of all double beta elements.

- Tellurium loadings of 0.3% in LAB were successfully done and the cocktail has been proven to be stable and clear for more than one year.
- In contrast to neodymium, no inherent optical absorption line was measured and the intrinsic light yield is higher as well (cf. Figure 2.6) [Loz14b] [Mot14].

The main disadvantage of ^{130}Te is the lower Q value. This results in less phase space for the decay and a more complex background due to additional natural radiation in lower energy regions.

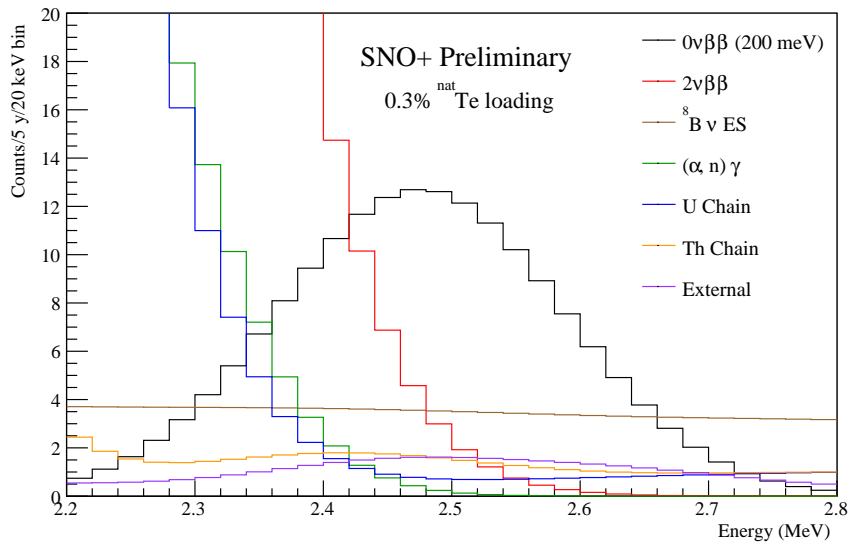


Figure 2.5: Expected energy spectrum in the $0\nu 2\beta$ peak region with backgrounds in SNO+. The counts are estimated for a 20% fiducial volume cut, measurement time of 5 years, background tag efficiency of $> 99.99\%$ for ^{214}Bi and 98% ^{208}Tl , factor 50 mitigation of ^{212}Bi and ^{212}Po , negligible cosmogenic activation and $m_{0\nu 2\beta} = 200\text{ meV}$ [Win14].

The main irreducible background for the $0\nu 2\beta$ peak is the high energy tail of the $2\nu 2\beta$ spectrum which increases with loading percentage. Due to the poor energy resolution of a liquid scintillator detector, this background will overlap with a big part of the 0ν peak. Another irreducible background comes from the ^8B neutrinos of the sun. The ^8B neutrinos create a continuous background from 0 to 15 MeV via elastic scattering in the LAB. In the region of interest (ROI), the ^8B spectrum is relatively flat (see Figure 2.5).

The backgrounds originating from ^{214}Bi (U chain) and ^{208}Tl (Th chain) decays can be strongly reduced by delayed coincidence β/α tagging because the half lives of the involved

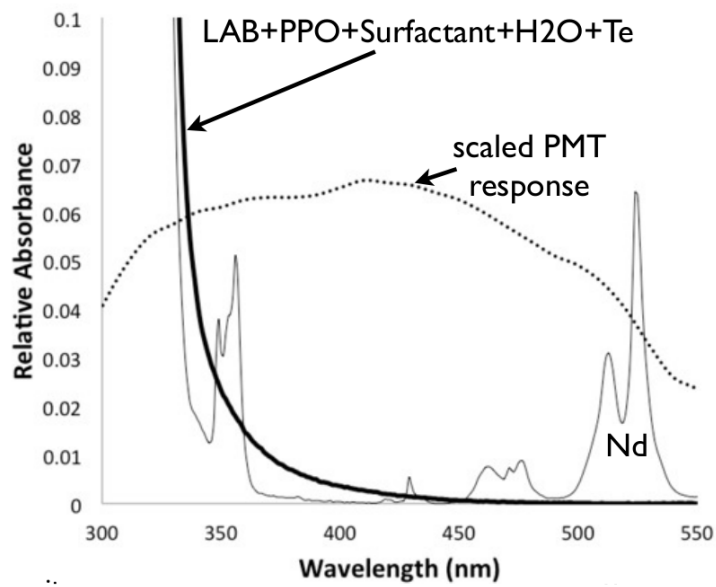


Figure 2.6: Relative absorbance of scintillation light by Nd and Te cocktail in LAB as a function of wavelength. The PMT response is added for comparison [FG14].

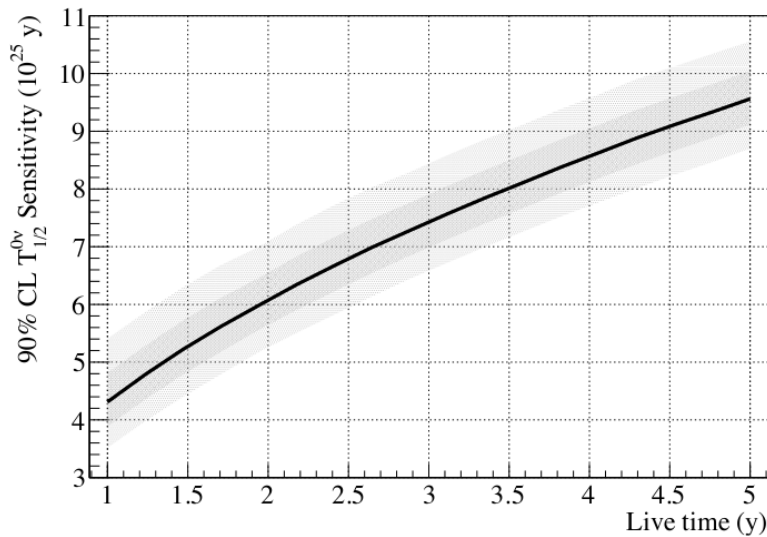


Figure 2.7: Expected half life sensitivities for a 0.3 % loading with ^{nat}Te at 90 % CL [FG14].

isotopes are relatively small. A rejection of >99.99 % for ^{214}Bi and 98 % for ^{208}Tl is expected [Mot14]. The efficiency for the ^{208}Tl tagging is lower because of its longer half life. Cosmogenic activation of the tellurium will be minimized by a purification strategy that has been developed specifically for SNO+ by the Brookhaven National Laboratory [BNL14] [Bil13] as well as minimal exposure time on the surface.

The expected spectrum for the case of an effective Majorana neutrino mass of 200 meV, 0.3 % loading of tellurium and a measurement time of 5 years is shown in Figure 2.5. Sensitivities for a Majorana neutrino mass of 100 meV are aimed for [Loz14a]. The corresponding half life limit expectations as a function of the data taking time (live time) are shown in Figure 2.7.

2.3.2 Solar neutrinos

Due to the energy threshold (3.5 MeV) of SNO only the high energy ^8B neutrinos from the Sun could be measured. Since SNO+ will be a liquid scintillator detector, its energy threshold will be around 0.2 MeV. This will allow the measurement of the monoenergetic flux of pep neutrinos at 1.44 MeV.

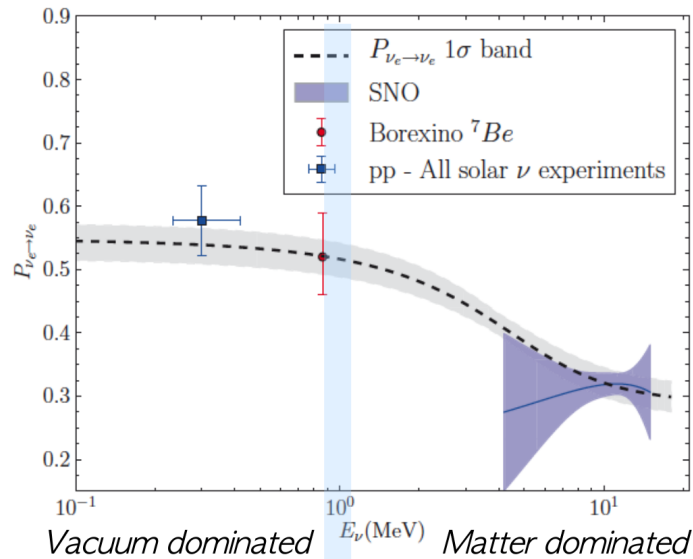


Figure 2.8: Survival probability of ν_e over energy. Vacuum and matter dominated energy regions of the solar neutrino spectrum are indicated. The region of the expected pep neutrino signal is shown as a vertical area [A⁺13b] [Loz14b].

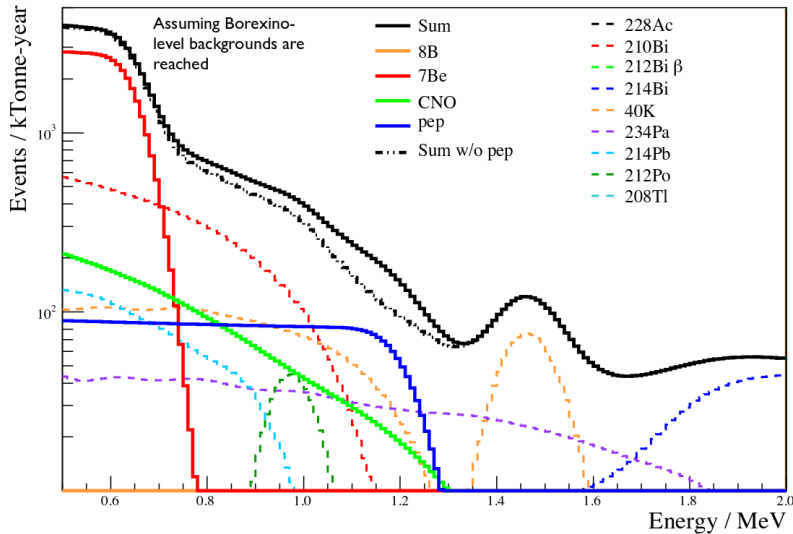


Figure 2.9: Expected number of events / kT-year from pep (blue), CNO (green), ^7Be (red) and ^8B (orange) solar neutrinos in SNO+ compared to expected backgrounds [Gan12].

The pep neutrinos will be detected via the observation of the energy spectrum of the recoiling electrons from neutrino-electron scattering. From solar models the flux is calculated with an uncertainty of $\pm 1.5\%$ which gives the opportunity to measure the survival probability with a high accuracy [Che11]. The measurement of the pep neutrinos will also contribute to the understanding of the neutrino oscillations between the vacuum dominated and the matter dominated energy region (see Figure 2.8) [Che08].

SNO+ has the sensitivities to measure also the fluxes of neutrinos produced in the CNO cycle of the Sun. Because CNO neutrino fluxes are directly proportional to the abundance of the heavier elements C, N, O and F, their measurement will help in understanding the metallicity of the Sun. Since the cross section for neutrinos is so small, they escape directly from the core of the Sun which gives direct information on the metallicity.

Although SNO+ has a natural shielding of 6000 m water equivalent, there are still about 70 atmospheric muons per day expected to traverse the detector [Che11]. These muons produce the beta plus emitter ^{11}C from ^{12}C which has a mass fraction of 86 % inside the LAB. ^{11}C has a half life of 20 minutes. The total energy released in the decay consists of two 511 keV gammas plus the β^+ energy and extends up to $\sim 2\text{ MeV}$. This poses a major background to the pep neutrino measurements.

Reaching low target levels in background reduction is especially crucial to the measure-

ment of the CNO neutrino flux because its spectral shape is close to that of ^{210}Bi . A high level of ^{210}Bi will make a discrimination very difficult. In Figure 2.9 the estimated signals of solar neutrinos are shown.

2.3.3 Geo and reactor antineutrinos

Another goal is the detection of antineutrinos from reactors and from inside the Earth. They are detected by the inverse beta decay reaction:



with an energy threshold of 1.8 MeV. The signature is a prompt signal from the positron annihilation and a delayed signal from the neutron capture on proton.

With a mean free path of several ten light years for 1 MeV antineutrinos in water, the measurement of geo antineutrinos provides a way of looking directly into the Earth's nuclear reactions. The $\bar{\nu}_e$ from the Earth originate in the β^- decay of the ^{238}U and ^{232}Th decay chains and from ^{40}K decay. Due to the energy threshold of reaction 2.1, the $\bar{\nu}_e$ from the ^{40}K cannot be detected.

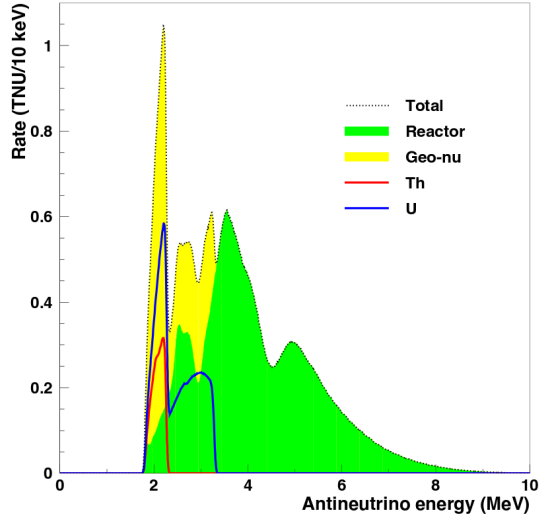


Figure 2.10: Expected rates from geo (yellow) and reactor (green) antineutrinos in SNO+. The geo antineutrinos originate from U (blue line) and Th (red line) decay chains [Dye12].

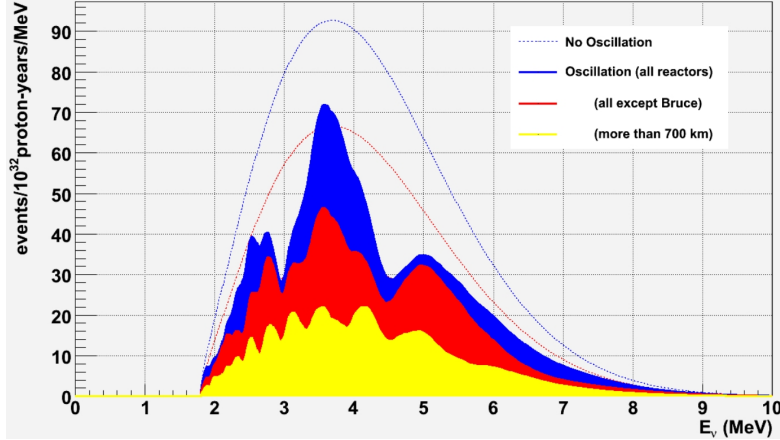


Figure 2.11: Simulated energy spectrum from reactor antineutrinos in SNO+. The spectrum is divided into that from all reactors (blue), all except Bruce Nuclear Generating Station (red) and reactors with distances larger than 700 km (yellow). Dotted lines show the spectra without oscillation [Gan12].

Because the location of the SNO+ detector is inside a nickel mine, the area is geologically well understood and predictions for the neutrino fluxes from theory can be tested. The measurement of geo antineutrinos will help understanding the relative contribution of radioactive decays to the heat production inside the Earth.

SNO+ will also be able to measure reactor antineutrinos from three reactors in the area. With 240 km distance the closest reactor (Bruce Nuclear Generating Station) is further away than for the KamLAND experiment. Despite the fact that the $\bar{\nu}_e$ flux is expected to be much smaller than that seen by KamLAND, the peak structure in the oscillation spectrum in Figure 2.11 is much sharper due to the good position with respect to the reactors. This will not only enable SNO+ to confirm the neutrino oscillation of the (1,2) sector at a higher energy but also allow SNO+ to be the first experiment that will see an oscillation induced dip in the $\bar{\nu}_e$ spectrum [Che11].

Since reactor and geo antineutrinos are a background to each other, the location of SNO+ is beneficial to the geo antineutrino measurement compared to other experiments. The relatively high distance to only a few reactors enhances the geo antineutrino to reactor antineutrino ratio by a factor of 4 compared to KamLAND [Lan07]. In Figure 2.10 the estimated energy spectrum from geo and reactor antineutrinos is shown.

2.3.4 Supernova neutrinos

With expected rates of 3 ± 1 core collaps supernovas per century in our cosmic neighborhood, the measurement of supernova neutrinos might happen once in the life time of the SNO+ experiment. Neutrinos of all kinds are released in a type II supernova explosion and carry about 99 % of the energy. A hypothetical supernova at a distance of 10 kpc from the Earth will result in an estimated 273 interactions via neutrino-proton scattering:



and 263 events from the inverse beta decay:



which are the main reaction channels. Such a neutrino shower will last for several 10 s [vK13].

Neutrinos arrive earlier than light from a supernova, because they escape the dense core before photons. A real time detection of these neutrinos can therefore be used to predict the arrival of the photons from the supernova. SNO+ as a real time detector for neutrinos will be part of the SuperNova Early Warning System (SNEWS) which is a combination of neutrino detectors designed to warn other astronomical telescopes that a supernova might become visible within a few hours.

2.4 SNO+ timetable

The electronics testing of the air filled detector was completed in 2013 and the water fill started at the end of 2013. Generally the water is filled at equal levels inside the AV and in the surrounding cavity to minimize tension. A phase where the water level is lower inside the AV will make it float which allows the testing of the rope system that holds the vessel down. This will ensure sufficient strength of the rope system for the scintillator phase.

While the water level is rising, it is possible to replace broken PMTs which will be reached by boat. When the cavity is about half way filled with water, a stop of a few days will allow the installation of the final fibres in the middle of the detector.

Calibrations during the water phase will be done mainly with optical calibration systems such as ELLIE. Because these are installed on the PSUP, the contaminations are

minimized. At the end of 2014 the water fill will be completed.

The first telluric acid is expected to arrive at site in 2014 and the processing and cleaning will start in 2015. The transition to the scintillator phase in 2015 will slowly replace the water inside the AV with LAB. In the scintillator phase the calibrations with radioactive sources will be done and the energy scale will be calibrated. Although the pure scintillator phase will be primarily used for calibrations, background measurement and as transition into the tellurium loaded phase, it may already yield first physics results e.g. for solar neutrinos or geo and reactor antineutrinos.

The main phase of the SNO+ experiment, namely measuring the neutrinoless double beta decay, will consist of operating the detector with a loading of 0.3 % natural tellurium in LAB. This phase is expected to start at the beginning of 2016 and it will run for some years until enough data is accumulated [Bil13]. For an increased sensitivity due to an increased number of ^{130}Te atoms, loadings of up to 3 % are under consideration and may follow after the first phase with 0.3 % loading.

During the double beta decay phase it is not possible to measure solar neutrinos. But when this phase is finished, the tellurium can be removed and another pure scintillator phase could follow for longer measurements of solar neutrinos.

3 Production of scandium isotopes via neutron activation of a titanium target

3.1 Motivation and experimental setup

The ^{48}Sc calibration source for SNO+ will be produced at the location of the Helmholtz-Zentrum Dresden-Rossendorf (HZDR) by neutron irradiation on a pure natural titanium target. For the calibration of the SNO+ detector an activity of 500 Bq for ^{48}Sc at the calibration campaign is desired. Because of the estimated shipping time of 6 days and the half life of 43.7 h [NND14], a production activity of 5000 Bq is aimed for. This ensures that the overall activity of the scandium source is low enough to be shipped without a declaration as radioactive source.

The neutrons are produced using a deuterium-tritium (DT) generator of the TU Dresden. The DT-generator accelerates deuterium ions inside a vacuum pipe that collide with a tritium target to produce the neutrons. The reaction is:



A flux of about 10^{11} neutrons per second can be achieved at full operation in a 4π sphere.

To test the capability of the neutron source to reach that activity, a first test activation was done in 2012. Due to technical problems and an unstable neutron flux, an activity

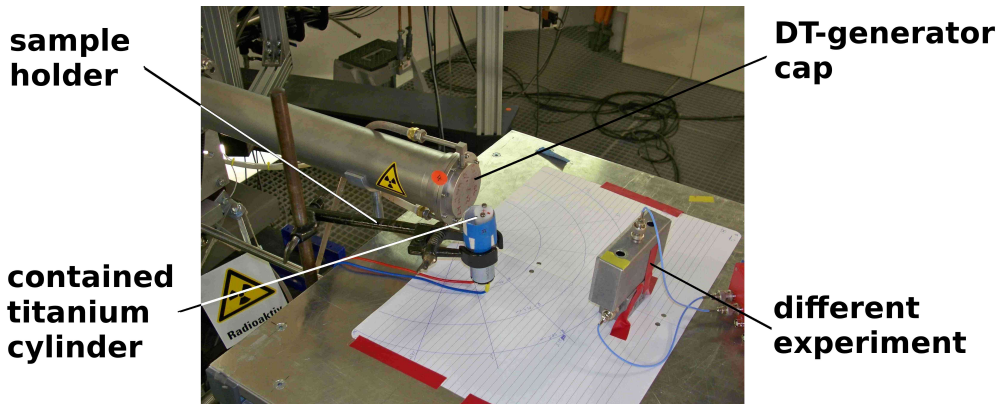


Figure 3.1: Titanium cylinder and probes in position for the irradiation. On the left side the end of the vacuum pipe with the tritium target inside is shown. On the right side another experiment for neutron irradiation was placed.

of only 1322 Bq was reached [Boe13]. After a long shutdown of the neutron source for maintenance, a second test activation was done to ensure that the neutron flux is still high enough for the activation.

Generally the titanium cylinder is positioned as close as possible to the tritium target to receive a neutron flux as high as possible. However, during the second activation in April 2014, a second experiment was performed at the same time which required a table in front of the target. The table slightly blocked the positioning of the holder for the titanium. For this reason the center of the titanium cylinder was placed at a distance of 10 cm to the target.

The distance was measured to the end of the metal cap of the vacuum pipe and the tritium target is located approximately 1 cm inside the pipe. The deuteron beam direction is altered during the irradiation to focus on fresh spots on the target. Since the exact position of the focal point is not known, an exact distance measurement to the source of the neutrons is not possible. The positioning and the second experiment are shown in Figure 3.1.

A small motor is attached below the holder to rotate the sample which ensures a uniform irradiation from all sides. Three aluminum probes are placed around the titanium cylinder and are used to measure the flux and check for inconsistencies in the uniform



Figure 3.2: Titanium cylinder placed in a plastic holder before the activation. The number I marks the first niobium probe and below the motor is visible.

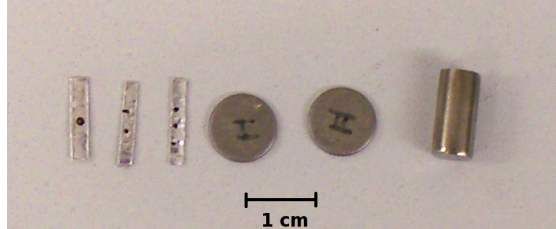


Figure 3.3: The three aluminum probes (stripes, left) and two niobium probes (disks, middle) for the neutron flux measurement. On the right side the titanium cylinder is shown.

irradiation. For the overall flux measurement one niobium probe is attached to the front of the plastic container and one to the back. The titanium cylinder is shown in Figure 3.3 together with the aluminum and niobium probes. A picture of the sample before the irradiation is shown in Figure 3.2.

After the irradiation when the dose rates in the neutron hall are low enough, the samples are retrieved and counted with a germanium detector.

3.2 Germanium-detector calibration

A germanium detector (DSG Detector Systems GmbH, NGC 3019, 30 % rel. eff. [DSG14]) was used to count the activated samples. The detector is located in an extra room close to the neutron hall. Prior to the counting of the irradiated titanium sample the detector was calibrated in energy to obtain its full energy peak efficiency.

The germanium detector is surrounded by lead bricks on all sides to reduce the background. A 1 mm copper plate in front of the detector lid absorbed a big part of the X-rays to reduce the count rate in the low energy region. A holder made of plastic was used to easily set different distances of the calibration sources and the samples with respect to the detector head. As calibration sources ^{137}Cs , ^{133}Ba ^{60}Co and ^{22}Na were used which allowed a calibration between 303 keV and 1333 keV. In Figure 3.4 a picture of the detector is shown.

The measurement distance for the activated titanium cylinder was chosen to be 30 mm which is a compromise solution between true coincidence summing (TCS) and counting statistics. Closer distances increase the TCS which is the simultaneous detection of more than one gamma from a cascade of one decay. This reduces the events in the single full energy peak and increases the events in the sum peak. The effect can be corrected

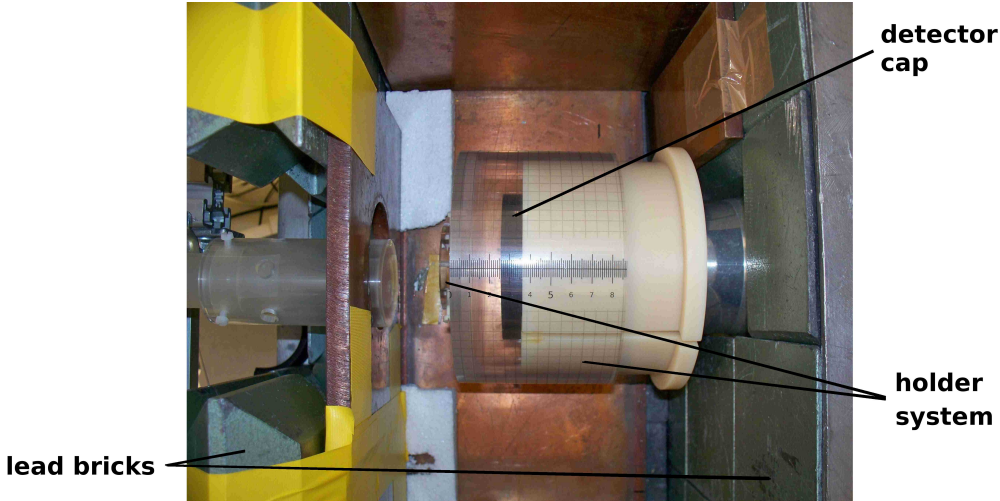


Figure 3.4: Germanium detector for calibration and measurement. The lead bricks, the black detector cap and the plastic holder for distance adjustments are visible.

for but the corresponding uncertainty increases with higher correction factors. Also the systematic error due to the shape of the titanium cylinder increases with closer distances because it cannot be treated as a point source.

Larger distances reduce the absolute detection efficiency which reduces the count rate. Because of the short half life of ^{48}Sc it is necessary to obtain high statistics in a relatively short amount of time to not significantly delay the shipping of the source after the final activation.

The TCS correction factors for ^{133}Ba and ^{60}Co were taken from simulations with the germanium detector in a modified version of RAT [Boe14]. For the β^+ calibration source ^{22}Na the TCS correction of the summing with an annihilation photon was applied manually. No TCS correction had to be done for the ^{137}Cs because it has only one gamma line.

The activities of the calibration sources are listed in Table 3.1. An uncertainty of 3% was assumed for the initial activities. Dead times of the detector were below 10% for all calibration sources and distances.

The absolute efficiency of the germanium detector was calculated for 7 energies by:

$$\eta = \frac{A_{net}}{t_{live} \cdot I_\gamma \cdot A_0} \cdot C_{TCS} \quad (3.2)$$

where η is the efficiency, A_{net} is the net area of the peak with subtracted background, t_{live} is the live time of the detector, I_γ is the probability for the gamma line, A_0 is

Table 3.1: Activities of the calibration sources.

Calibration source	$A(01.02.01) / 10^4 \text{ Bq}$	$A(11.04.14) / 10^4 \text{ Bq}$
^{137}Cs	3.83	2.83
^{133}Ba	4.20	1.76
^{60}Co	4.33	0.76
^{22}Na	3.84	0.11

the activity of the calibration source at the time of calibration and C_{TCS} is the TCS correction factor. The net counts in the peak area were obtained with the Genie 2000 software.

In Figure 3.5 the full energy peak efficiency of a germanium detector as a function of the energy of the gamma is shown. The efficiency function of every germanium detector should follow the trend of this curve. For higher energies the probability of the gammas to traverse the detector without energy deposition increases. In the region below 100 keV the gammas are absorbed by the detector cap and cannot reach the sensitive detector volume. Since all calibration points are well above the maximum of the expected efficiency curve, a function with the form:

$$\ln(\eta) = A \cdot \ln(E) + B \quad (3.3)$$

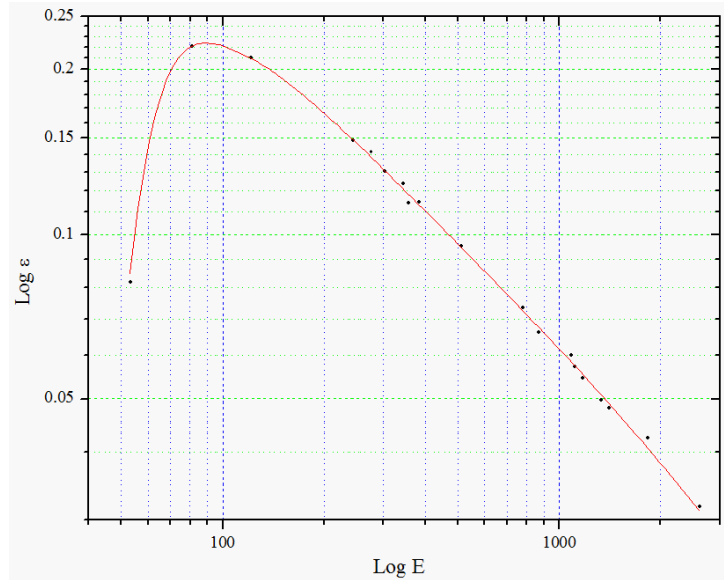


Figure 3.5: Full energy peak efficiency function for a general germanium detector in double logarithmic scale. The germanium detector used for the measurements should follow the trend of this efficiency curve [N⁺08].

was fitted for the efficiency calibration. With an energy of 159 keV, ^{47}Sc has the lowest gamma line among the analysed isotopes. The full energy peak efficiency of 159 keV gammas is 4.7 % and was obtained with Equation 3.3 because it is still above the maximum of the expected function in Figure 3.5.

In Figure 3.6 the measured full energy peak efficiency function in double logarithmic scale is shown. The improvement of the data points due to the TCS correction is visible. To account for the systematic uncertainty due to the thickness of the titanium cylinder (6 mm diameter) an efficiency calibration was also done at 27 mm and 33 mm distance. This corresponds to the closest and farthest part of the cylinder in an upright position (vertical axis of the cylinder). Additionally a calibration at 10 mm distance was done for the measurement of the niobium and the aluminum probes (see Section 3.4). They were measured at the closest possible distance to increase the statistics especially for the aluminum probes due to the short half life of ^{24}Na ($T_{1/2} = 14$ h).

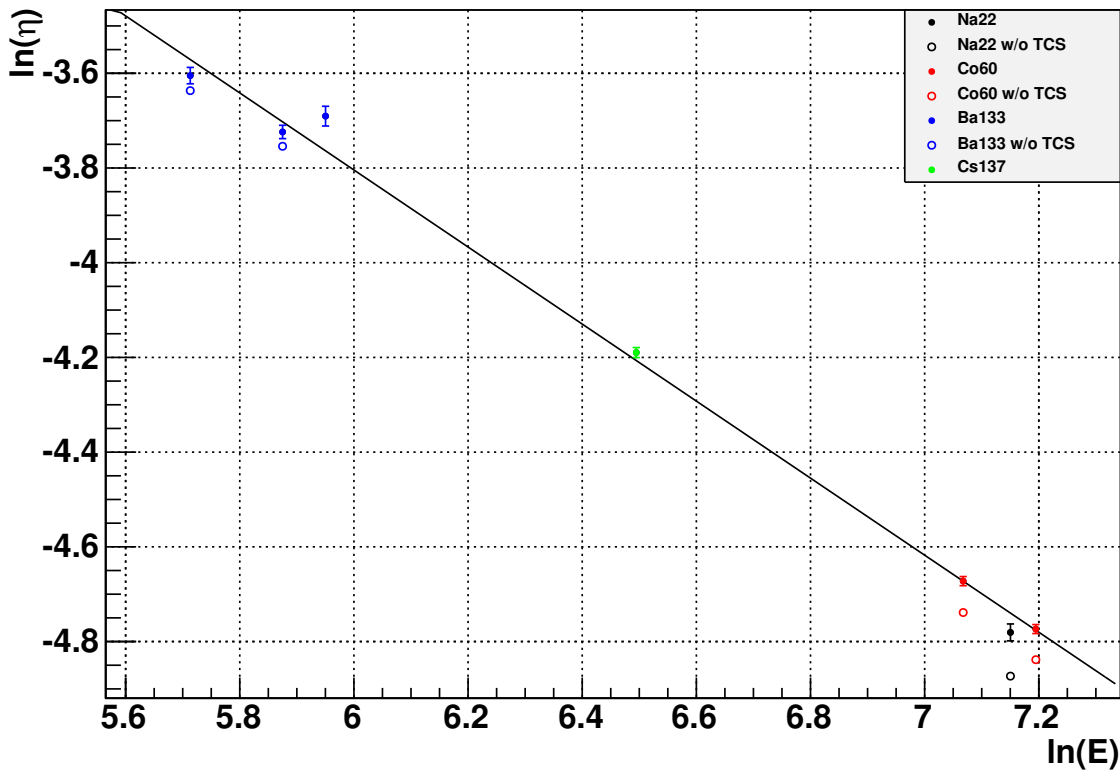


Figure 3.6: Full energy peak efficiency function for 30 mm distance from the detector cap in double logarithmic scale. Hollow data points are without TCS correction (^{137}Cs has a full point because it does not need TCS correction).

3.3 Scandium isotopes

The three most important isotopes that are activated by the irradiation of natural titanium with neutrons are ^{46}Sc , ^{47}Sc and ^{48}Sc . They decay via β^- decay with following γ cascades.

The calibration source was designed for the isotope ^{48}Sc which emits an electron followed by a cascade of three or four gammas. According to simulations, the container of the source is thick enough to absorb the emitted electron in $> 99\%$ of the cases leaving only the gamma energy for the calibration.

The Q-value of ^{48}Sc is $3992(5)$ keV and the half life is $43.67(9)$ h [NND14]. As shown in the decay scheme in Figure 3.7, in $89.98(18)\%$ of the cases the ^{48}Sc decays to the 3333.2 keV level of ^{48}Ti . The three gammas that are emitted from this level will be used for the calibration in SNO+. The 3508.6 keV level is reached with a probability of $10.02(18)\%$ [Fir99]. From there it decays either to the 3333.2 keV level with a probability of $7.48(9)\%$ or to the 2295.7 keV level with $2.38(4)\%$ releasing a gamma with the energy equal to the difference between the two levels.

Originally the ^{48}Sc was chosen as isotope for calibration, because the sum energy of the three gammas is close to the Q-value of the double beta decay of ^{150}Nd which was the double beta isotope considered for SNO+ before ^{130}Te . A calibration near the energy region of interest gives the opportunity to study the detector response where it is most important for the main physics goal of searching for the neutrinoless double beta decay. The Q-value of ^{130}Te at 2.5 MeV is still relatively close to the ^{48}Sc sum energy of 3333.2 keV but the ^{48}Sc source has lost its exceptional position among the calibration sources.

The decay schemes of ^{46}Sc and ^{47}Sc are shown in Figure 3.8 and 3.9. Again, the electrons from the β decay will be mostly absorbed by the source container. The Q-value of ^{46}Sc is $2366.7(7)$ keV and the γ cascade consists of two gammas with a sum energy of 2009.8 keV. In $1.3 \cdot 10^{-5}(10)\%$ of the cases it decays with only one gamma directly to the ground state of ^{46}Ti [NND14]. With a 40 times longer half life than ^{48}Sc and a sum gamma energy of about 2 MeV it is possible to reuse the calibration source with ^{46}Sc once the ^{48}Sc is decayed. The possibility of a usage of ^{46}Sc as second calibration isotope within the same source will be investigated in Section 6.2.

The Q-value of ^{47}Sc is $600.3(19)$ keV. It decays with a probability of $31.6(6)\%$ directly to the ground state of ^{47}Ti emitting only the electron. In $68.4(6)\%$ of the cases it decays to the $159.4(19)$ keV level releasing a gamma with that energy [NND14]. This gamma energy is close to the expected trigger threshold of the SNO+ detector. Depending on the actual threshold in the experiment, the ^{47}Sc peak might be only partly visible.

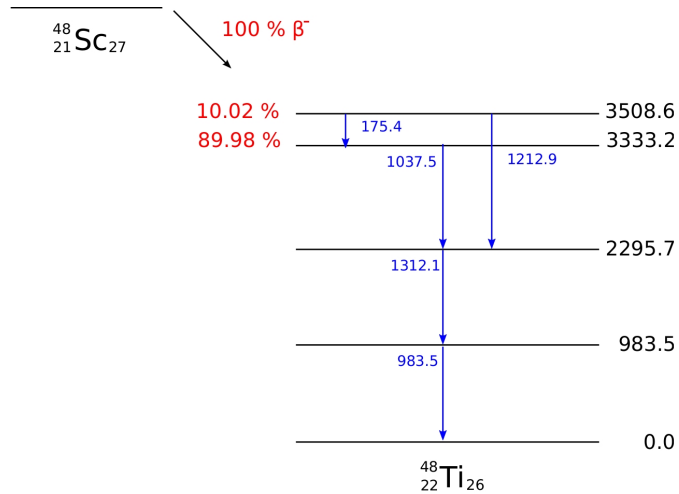


Figure 3.7: Decay scheme of ^{48}Sc to ^{48}Ti with a half life of 43.7 h [NND14].

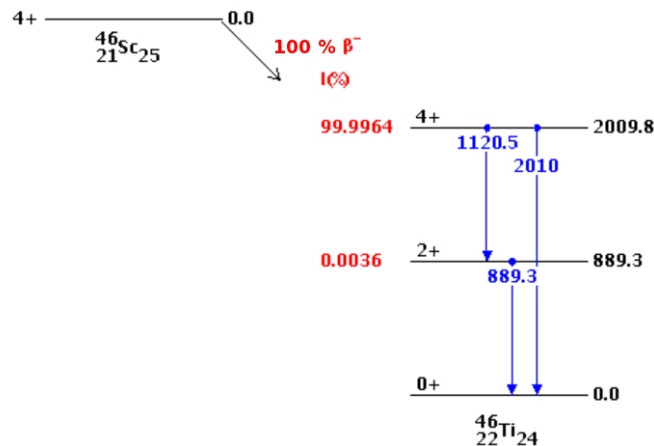


Figure 3.8: Decay scheme of ^{46}Sc to ^{46}Ti with a half life of 83.8 d [NND14].

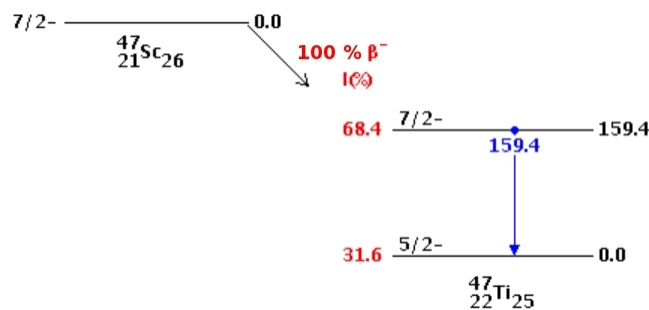


Figure 3.9: Decay scheme of ^{47}Sc to ^{47}Ti with a half life of 3.35 d [NND14].

3.4 Titanium target

The test activation of the titanium cylinder that will be used for the SNO+ calibration was done the 11.04.2014 and the DT-generator was active from 11:11 until 16:32.

Because it was the first measurement after a shutdown time of over one year it was carefully operated to check if everything was working properly. For a live measurement of the neutron flux a silicon detector is installed in the neutron hall. It detects secondary radiation caused by moderated neutrons and is used to monitor the neutron flux during an activation. The live dose rate in the hall is measured as well.

After a long operation it can take several hours until it is safe to reenter the hall. The data of the silicon detector for the irradiation on the titanium cylinder is shown in Figure 3.10. In contrast to the first activation [Boe13], the flux was stable at a high rate for about 4 h after which it was shut down.

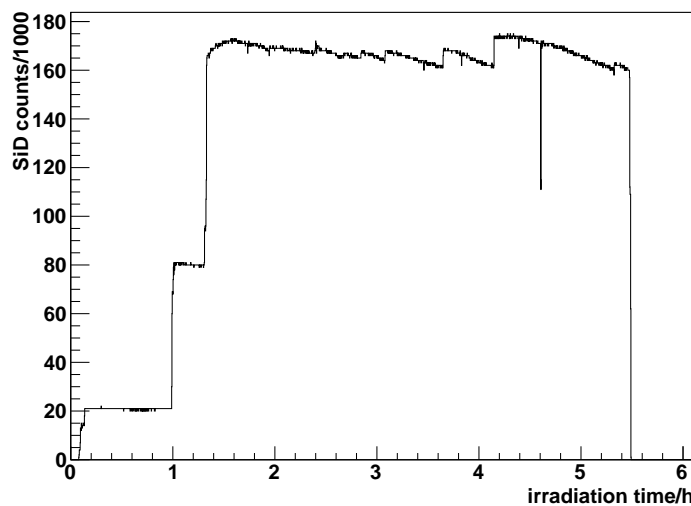


Figure 3.10: Neutron flux measured in counts of the silicon detector in the neutron hall during the irradiation of the titanium cylinder on 11.04.2014.

The energy spectrum of the neutron flux depends on the angle to the beam line. An energy spectrum of the neutron flux intensity at 0° based on measurements and simulations is shown in Figure 3.11. The maximum intensity is at around 15 MeV.

Table 3.2: Isotopes of natural titanium and their abundances [NND14].

Isotope	^{46}Ti	^{47}Ti	^{48}Ti	^{49}Ti	^{50}Ti
Abundance / %	8.25 (3)	7.44 (2)	73.72 (3)	5.41 (2)	5.18 (2)

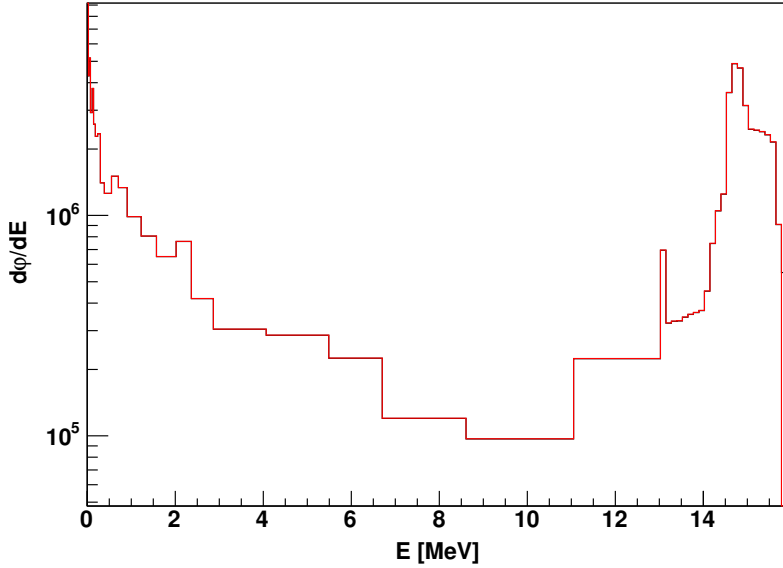


Figure 3.11: Energy dependent intensity of the neutron flux obtained from measurements and simulations. The maximum intensity is at around 15 MeV [Kan14].

The used titanium cylinders are from the Alfa Aesar company and have a certified purity of 99.998 %. Natural titanium consists of 5 stable isotopes which are listed in Table 3.2 with their abundances.

During the neutron irradiation the 5 scandium isotopes, from ^{46}Sc to ^{50}Sc , are produced. The (n,p) reactions on the titanium isotopes have the highest cross section. Additionally ^{45}Ca and ^{47}Ca are produced via (n,α) reactions on ^{48}Ti and ^{50}Ti as well as ^{45}Ti which is activated via a (n,2n) reaction on ^{46}Ti .

Table 3.3: Half lives and gamma energies, with intensities, for the activated isotopes visible to the SNO+ detector [NND14].

Isotope	$T_{1/2} / \text{d}$	γ energy / keV	$I_\gamma / \%$
^{46}Sc	83.79 (4)	889.277 (3)	99.9840 (10)
		1120.545 (4)	99.9870 (10)
^{47}Sc	3.3492 (6)	159.381 (15)	68.3 (4)
^{48}Sc	1.820 (4)	175.361 (5)	7.48 (10)
		983.526 (12)	100.1 (6)
		1037.522 (12)	97.6 (7)
		1212.880 (12)	2.38 (4)
		1312.120 (12)	100.1 (7)
^{47}Ca	4.536 (3)	1297.09 (10)	67

^{45}Ca undergoes β^- decay and emits a gamma with 12.4 keV which is far below the energy threshold of SNO+. The isotopes ^{45}Ti , ^{49}Sc and ^{50}Sc will be decayed before the source is deployed, because their half lives are at 185 min, 57 min and 1.7 min. These four isotopes are therefore irrelevant for the calibration of the SNO+ detector.

^{46}Sc , ^{47}Sc , ^{48}Sc and ^{47}Ca have relatively long half lives and high energetic gamma lines and will be visible to the SNO+ detector when the source is deployed. The half lives and main gamma lines, with the respective intensities of these activated isotopes, are listed in Table 3.3.

For an independent measurement of the neutron flux close to the titanium cylinder three aluminum and two niobium probes were used. Aluminum and niobium are standard elements for the monitoring of neutron fluxes because the cross sections are well known. An (n,α) reaction on the only stable aluminum nuclide ^{27}Al produces the radioactive sodium nuclide ^{24}Na with a cross section of 0.121 b [KR13]. Small amounts of ^{26}Al might be produced via $(n,2n)$ reaction but due to the half life in the order of 10^5 years it is not detectable.

The only stable nuclide of niobium is ^{93}Nb which produces $^{92\text{m}}\text{Nb}$ via $(n,2n)$ reaction with a cross section of 0.459 b and $^{90\text{m}}\text{Y}$ via (n,α) reaction during the neutron irradiation [KR13]. The activities from ^{24}Na , $^{92\text{m}}\text{Nb}$ and $^{90\text{m}}\text{Y}$ can be measured after irradiation to determine the neutron flux. The half lives, main gamma energies and intensities are listed in Table 3.4.

Table 3.4: Half lives and main gamma energies with intensities for the activated isotopes for the neutron flux measurement [NND14].

Isotope	$T_{1/2}$	γ energy / keV	$I_\gamma / \%$
^{24}Na	14.997 (12) h	1368.633	100
$^{92\text{m}}\text{Nb}$	10.15 (2) d	934.46 (5)	99
$^{90\text{m}}\text{Y}$	3.19 (6) h	202.51 (3) 479.17 (9)	97.3 (4) 90.74 (3)

3.5 Results of the neutron activation campaign

3.5.1 Titanium cylinder

The titanium cylinder was counted three times after the irradiation. Due to the availability of the detector, the first measurement was done three days after the activation. Two longer measurements of the titanium cylinder followed (6 and 27 days after activation) to collect more statistics and compare the peaks of ^{46}Sc and ^{48}Sc as they decay.

The long measurements also allowed the search for possibly activated impurities in the titanium. The spectrum of the first measurement on 14.04.14 can be found in Appendix A.1.

The activity at the end of irradiation A_{EoI} (on 11.4.) was calculated by:

$$A_{EoI} = \frac{A_{net} \cdot C_{TCS} \cdot C_{lapse}}{t_{live} \cdot I_{\gamma} \cdot \eta \cdot C_{decay}} \quad (3.4)$$

where A_{net} is the net peak area, t_{live} is the live time of the detector, I_{γ} is the probability for the gamma line and η is the full energy peak efficiency. The correction factors are for the true coincidence summing (C_{TCS}), the time lapse from the end of irradiation until beginning of measurement (C_{lapse}) and the decay of the nuclide during the measurement (C_{decay}).

The efficiency of each energy was extrapolated from the efficiency curves obtained with the calibration sources (see Section 3.2). Like during calibration the net count area A_{net} was obtained with the Genie 2000 software.

C_{lapse} and C_{decay} are calculated by:

$$C_{lapse} = e^{\lambda \cdot t_{lapse}} \quad C_{decay} = \frac{(1 - e^{-\lambda \cdot t_{real}})}{\lambda \cdot t_{real}} \quad (3.5)$$

where t_{lapse} is the time from the end of irradiation until the beginning of the measurement, t_{real} is the real measurement time and λ is the decay constant of the nuclide. The activities of each scandium and calcium line are listed in Tables 3.5, 3.6 and 3.7.

The error consists of three parts. The statistical error is the peak area uncertainty and

Table 3.5: Activities for each gamma line of the activated nuclides. The detector live time was 60.62 min. Measurement date: 14.04.14.

Nuclide	Energy / keV	Activity / Bq	Error / %			
			Stat.	Dist.	Eff.	Total
^{46}Sc	889	23.26	5.02	7.84	11.79	15.02
	1121	24.27	8.84	7.83	12.00	16.84
^{47}Sc	159	520.50	0.73	7.88	10.29	12.98
^{48}Sc	175	2874.90	1.72	7.87	10.37	13.14
	984	2009.38	0.77	7.84	11.88	14.25
	1038	2001.11	0.81	7.83	11.93	14.29
	1213	1940.54	9.53	7.83	12.07	17.26
	1312	1962.77	0.76	7.83	12.14	14.46
^{47}Ca	1297	8.64	13.48	7.83	12.12	19.75

Table 3.6: Activities for each gamma line of the activated nuclides. The detector live time was 121.17 h. Measurement started: 17.04.14.

Nuclide	Energy / keV	Activity / Bq	Error / %			
			Stat.	Dist.	Eff.	Total
^{46}Sc	889	22.75	0.58	7.84	11.79	14.17
	1121	23.27	0.60	7.83	12.00	14.34
^{47}Sc	159	519.73	0.11	7.88	10.29	12.96
^{48}Sc	175	2762.22	0.51	7.87	10.37	13.03
	984	1878.56	0.18	7.84	11.88	14.23
	1038	1951.55	0.22	7.83	11.93	14.27
	1213	2057.90	3.00	7.83	12.07	14.69
	1312	1748.43	0.21	7.83	12.14	14.44
^{47}Ca	1297	6.10	1.95	7.83	12.12	14.56

Table 3.7: Activities for each gamma line of ^{46}Sc . The nuclides ^{48}Sc , ^{47}Sc and ^{47}Ca were already decayed or the peak areas showed high statistical uncertainties 29 days after the activation. The detector live time was 167.02 h. Measurement started: 08.05.14.

Nuclide	Energy / keV	Activity / Bq	Error / %			
			Stat.	Dist.	Eff.	Total
^{46}Sc	889	22.84	0.43	7.84	11.79	14.17
	1121	23.59	0.45	7.83	12.00	14.16

follows a Poisson error on the total counts. It was obtained with the Genie 2000 software and generally the uncertainty for 1σ is given. The error on the efficiency from the calibration gives the first systematic error.

The cylinder was measured at a distance of 30 mm from its center to the detector cap in an upright position (vertical axis of the cylinder). Since the titanium cylinder is not a point source, the distance of the decaying nuclides to the detector ranges from 27 mm to 33 mm which corresponds to the diameter of the cylinder. To compute the changes in detector efficiency due to the distance uncertainty, additional efficiency functions at these two distances were obtained from the calibration. The difference between the efficiencies in these two positions with respect to that at 30 mm were calculated for each energy. Their weighted average gives the second systematic error. The total error was calculated by:

$$\delta A_{tot} = \sqrt{\delta A_{eff}^2 + \delta A_{dist}^2 + \delta A_{stat}^2} \quad (3.6)$$

The first measurement of the titanium cylinder was relatively short (cf. Table 3.5) because the aluminum and niobium probes had to be measured the same day. For this reason, the gamma lines with low intensities have a high statistical error but for the main lines of ^{48}Sc sufficient statistics was obtained. In Table 3.7 only ^{46}Sc is shown because at the time of measurement the ^{47}Sc , ^{48}Sc and ^{47}Ca was mostly decayed. In Figure 3.12 the decreasing activity of ^{46}Sc is compared to the theoretical expectation of an exponential function. The exponential function was calculated with an initial activity of 23.3 Bq which was obtained as average ^{46}Sc activity for the end of irradiation (cf. Table 3.8).

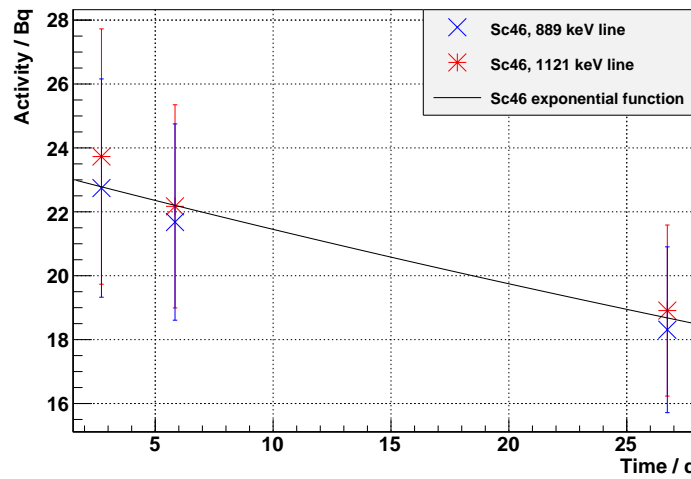


Figure 3.12: Obtained activities for the 889 keV (blue) and 1121 keV (red) gamma line of ^{46}Sc in the three measurements. The expected exponential function for an initial activity of 23.3 Bq (cf. Table 3.8) is shown for comparison.

The discrepancy between the activity obtained for the 175 keV line of ^{48}Sc and the other lines was already observed in [Boe13]. A possible explanation is an overestimate of the TCS correction factor that was obtained from simulations. This error could also affect the activity of ^{47}Sc which has a gamma line with similar energy. Since ^{47}Sc has only one gamma line the obtained activity cannot be cross checked like those from ^{48}Sc .

Average activities from the combined three measurements and from all available gamma energies, except the 175 keV line of ^{48}Sc , were calculated for the four nuclides. Using the total errors as weight, the weighted average was obtained for each measurement as:

$$\bar{A} = \frac{\sum_{i=1}^N \frac{A_i}{\Delta A_i^2}}{\sum_{j=1}^N \frac{1}{\Delta A_j^2}} \quad (3.7)$$

where N is the number of measured gamma lines. The average errors were obtained as:

$$\overline{\Delta A} = \left(\sum_{i=1}^N \frac{1}{\Delta A_i^2} \right)^{-\frac{1}{2}} \quad (3.8)$$

The final activities result from the weighted average of all available measurements and are listed in Table 3.8.

Table 3.8: Average activities combining all three measurements of the titanium cylinder and all available gamma energies for each nuclide. The 175 keV line of ^{48}Sc was not included.

Nuclide	^{46}Sc	^{47}Sc	^{48}Sc	^{47}Ca
Activity / Bq	23.3 (1.4)	520.1 (47.7)	1942.1 (100.6)	7.0 (0.8)

If the titanium cylinder would have been placed at 7 cm distance from the DT-generator cap instead of 10 cm, the neutron flux through the sample would have been about a factor 2 higher. In this case the activity of ^{48}Sc would have reached 4000 Bq. With one more hour of irradiation the desired amount of 5000 Bq could have been reached. In table 3.9 the calculated activities at 7 cm distance are shown together with the activity after an estimated travel time of 6 days. This time is a reasonable estimate of the time needed to ship the source to SNO+ including all necessary procedures.

Table 3.9: Average activities at a hypothetical 7 cm distance from the detector cap. Expected activities after 6 days are shown as well (see text).

Nuclide	^{46}Sc	^{47}Sc	^{48}Sc	^{47}Ca
Activity / Bq (7 cm distance)	47.5 (2.9)	1061.5 (97.3)	3963.5 (205.3)	14.3 (1.7)
Activity / Bq after 6 d	45.2 (2.7)	306.6 (28.1)	403.1 (20.9)	5.7 (0.7)

3.5.2 Aluminum and niobium probes

The aluminum and niobium probes were used to determine the neutron flux during the activation. ^{24}Na is produced in the aluminum and $^{90\text{m}}\text{Y}$ and $^{92\text{m}}\text{Nb}$ in the niobium probes as explained in Section 3.4. Because the measurement with the germanium detector was done three days after the irradiation, $^{90\text{m}}\text{Y}$ had been already decayed and could not be observed. The statistics for the ^{24}Na was also relatively low because it was measured

4.5 half lives after the activation. It was decided to count the monitors for a short time in order to allocate more data taking time for the titanium cylinder. In Table 3.10 the specific activities of the aluminum and niobium monitors are shown.

Table 3.10: Specific activities of the aluminum and niobium probes calculated for the end of irradiation (11.04.). Measurement date: 14.04.14.

Nuclide	Probe number	Live time in s	Specific activity in Bq / g	Error / %		
				Stat.	Eff.	Total
²⁴ Na	1	4238	14897	4.44	9.99	10.93
	2	5375	15631	4.82	9.99	11.09
	3	4588	14331	4.90	9.99	11.12
^{92m} Nb	1	899	1602	0.75	9.71	9.74
	2	1502	810	0.83	9.71	9.75

The probes were measured at 10 mm distance from the detector cap to increase the statistics. The specific activities A_{Spec} were calculated as:

$$A_{Spec} = \frac{A_{net} \cdot C_{TCS} \cdot C_{lapse}}{t_{live} \cdot I_{\gamma} \cdot \eta \cdot C_{decay} \cdot m_{probe}} \quad (3.9)$$

where the correction factors are the same as for the titanium cylinder (Eq. 3.4) and m_{probe} is the mass of the probe.

The statistical error was given by the Genie 2000 software and the efficiency error was obtained by the efficiency calibration at 10 mm distance. The total error was calculated as:

$$\delta A_{Spec,tot} = \sqrt{\delta A_{eff}^2 + \delta A_{stat}^2} \quad (3.10)$$

The niobium probes were placed at 8.5 cm and 11.9 cm distance from the DT-generator cap position. Applying a distance correction, $\frac{1}{r^2}$, to the second Nb probe the activity is in agreement within error with the one of the first Nb probe which is closer to the DT-generator cap. The new specific activity is 1588 Bq / g.

The neutron flux Φ through each probe was calculated as:

$$\Phi = \frac{A_{Spec} \cdot M}{\sigma \cdot N_A \cdot (1 - e^{-\lambda t_{irr}})} \quad (3.11)$$

where M is the molar mass, σ is the cross section, N_A is the Avogadro constant, λ is the decay constant and t_{irr} is the duration of the irradiation. The cross sections were taken from [KR13]. The irradiation time was 4.28 h since when the neutron source was operated at a high flux (cf. Fig. 3.10).

To get the neutron intensity I , the flux was multiplied by the total area that all neutrons pass at the distance of measurement:

$$I = \Phi \cdot 4\pi d^2 \quad (3.12)$$

where d is the distance from the DT-generator cap.

Table 3.11: Total neutron intensities obtained with the aluminum and niobium probes.

Nuclide	Probe number	Tot. neutron intensity / (10^{10} s^{-1})
^{24}Na	1	4.66 (0.51)
	2	4.89 (0.54)
	3	4.49 (0.49)
$^{92\text{m}}\text{Nb}$	1	5.04 (0.49)
	2	4.70 (0.45)
Weighted average		4.75 (0.22)

The intensities are listed in Table 3.11. All 5 probes agree well within the error and an average intensity of $4.75 (0.22) \cdot 10^{10} \text{ s}^{-1}$ was obtained (cf. Eq. 3.7 and 3.8).

It is worth noting that for this activation the acceleration voltage of the deuteron ions was set to 100 kV because it was the first run after a long technical maintenance period of over one year. When the DT-generator would be operated at the designed voltage of 280 kV, even larger intensities in the order of 10^{11} s^{-1} can be achieved.

Due to the large errors on the aluminum probes they could not be used to check a uniform irradiation of the titanium cylinder. The variation in distance is too small to give any indication. Since the motor was still running when the cylinder and the probes were retrieved after the irradiation, a uniform irradiation was safely assumed.

4 Test and production of the source container components

4.1 Scandium container design and production

Every time a calibration source is deployed into the SNO+ detector there is a risk of contamination with additional radioactive material. To minimize this risk an independent source committee ensures high safety standards for the source components before they can be used in the detector.

The concept of the scandium calibration source includes the possibility to open and close the enclosing containers. This is because the short half life of ^{48}Sc requires a fast procedure from the source production to the calibration. A glueing of the container would require a following mechanical polishing with an activated source that cannot be done due to radiation safety rules at the workshop. An advantage of the open design is that a source container that has proofed its viability can be reused with a newly activated titanium cylinder for every new calibration.

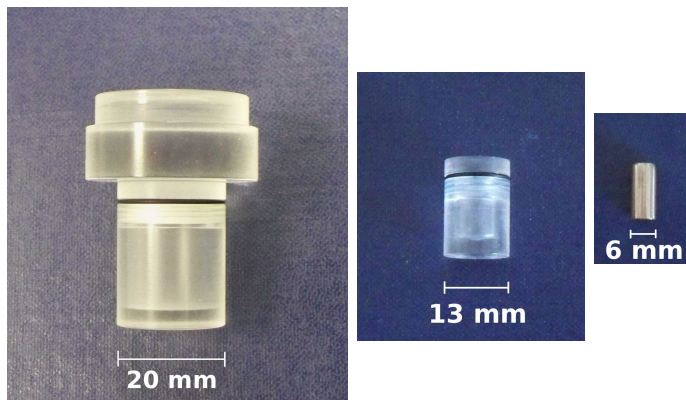


Figure 4.1: Prototypes of the outer container (left) and inner container (middle) for the titanium cylinder (right). The sealing O-rings are shown.

The source is encapsulated in two containers made out of acrylic (PMMA). Acrylic is used because it is compatible with LAB and it is transparent to the scintillation light. A double encapsulation ensures that the high safety standard required by the source committee is met. Both containers have to be stable and tight to safely shield the surrounding LAB from the source. Tightness for LAB is accomplished via perfluor elastomer (FFKM) O-rings which are proved to be compatible with LAB. In Figure 4.2 the absorption of UV and visible light in a pure LAB sample is compared to that of LAB with a cleaned O-ring inside. The measurement was taken after one month of exposure to LAB [Ans12].

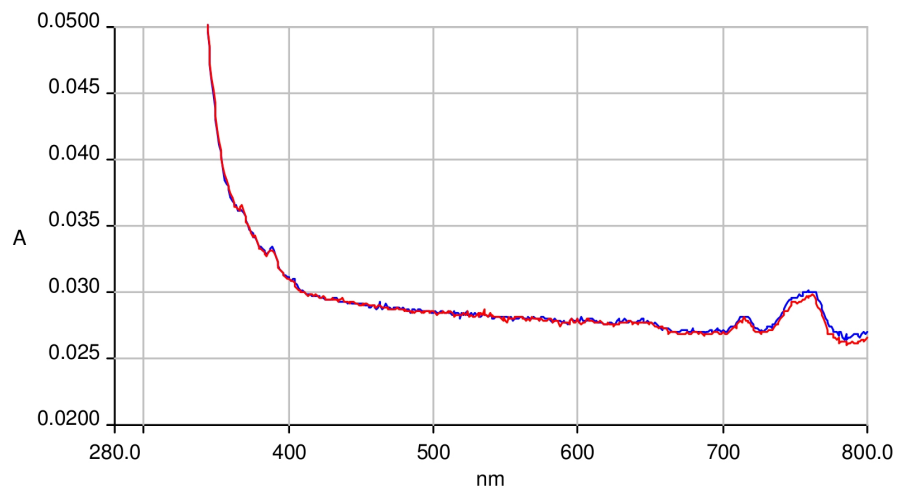


Figure 4.2: Absorbance spectra of pure LAB (blue) compared to O-ring inside LAB (red) after one month of exposure [Ans12].

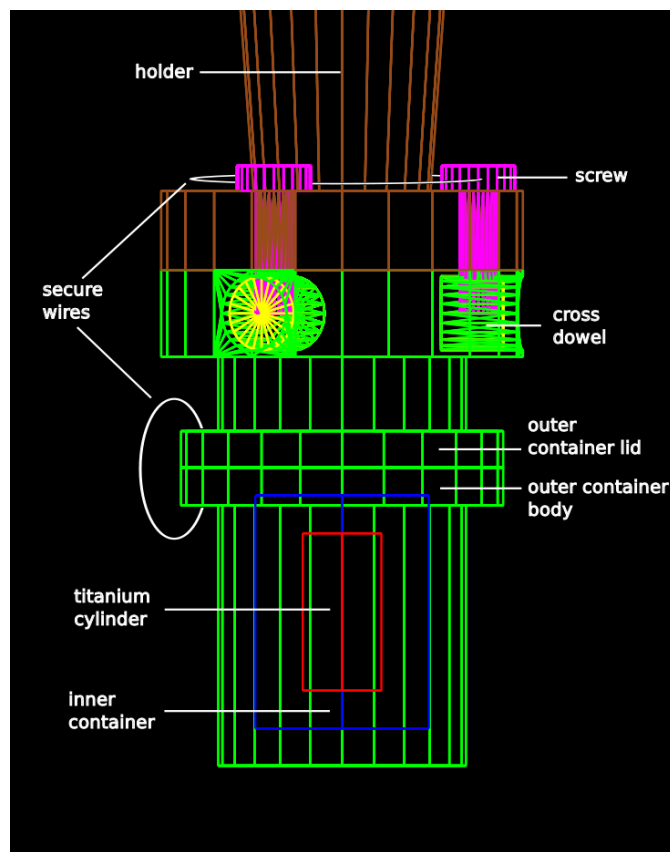


Figure 4.3: Drawing of the main components of the calibration source.

The O-rings are placed at the junction between the body and the lid of the inner and outer container. Pressure tests were done with prototypes of the two containers to ensure their tightness (see Section 4.3). The prototypes along with the titanium cylinder are shown in Figure 4.1. They give an idea of the shape and dimensions but they differ from the final design.

The calibration sources for the SNO+ detector are required to have a weight between 3 and 4 kg to ensure enough tension for the ropes of the calibration system. To reach that weight, the scandium calibration source is attached to a stainless steel weight cylinder (about 3 kg) via a holder. The holder increases the distance between source and weight cylinder to reduce energy loss inside the stainless steel. The material of the holder was originally designed to be PTFE and the length was 30 cm. These are the parameters that were used for the simulations in this thesis. However, due to simulations in Section 6.6 and in [Boe13] the final material will be acrylic and the height of the source box requires the length to be 20 cm.

The connection of the source to the holder is made via three stainless steel screws through the lid of the outer container as shown in Figure 4.3. During the movement of the source in the LAB it is possible that the screws become loose if they are not secured. Standard screws will be used but the screw heads will have small holes where a stainless steel wire will go through all three screws to keep them together if one unscrews. The ends of the wire will be tightly twisted so it cannot get lost.

Another solution was found for the nuts of the screws. It is not possible to cut holes for the nuts from the top into the lid of the outer container because they need to be larger than the holes for the screws. When the nut holes are cut from the side there is always the possibility that one of the nuts slightly unscrews and falls out. The solution is the usage of stainless steel cross dowels. They have a cylindrical shape which is easily cut into the lid and also keeps them from turning and consequently unscrewing.

The two parts of the outer container will be screwed together. Small edges with vertical holes are added on both parts. To prevent them from unscrewing, another wire goes through two holes and the ends are twisted. Six holes with slightly different relative positions will be drilled in the collar to account for possible misalignment during closure. This design ensures that the two parts of the outer container cannot be separated during measurement.



Figure 4.4: Photo of a cross dowel [PV14].

The source components are produced at the workshop of the TU Dresden. Since the collaboration is already familiar with the material, the acrylic for the two containers and the holder was bought from the same vendor who also supplied the acrylic vessel. Stainless steel for the screws, cross dowels and wires will be supplied by the workshop and the material was tested for compatibility with LAB.

During the production process for the two containers and the holder it is possible that tensions are created inside the material. Because these tensions could lead to cracks or crazings, they are removed by an annealing process. When the acrylic parts are brought into a rough shape by the workshop, they are annealed for the first time after receiving the material. In an oven they are slowly heated up to about 80 °C, remain there for some hours and are then cooled down again to room temperature. The annealing time for the ramp up, soak and ramp down depends on the thickness of the material. For example, the outer container goes through 12 h heating, 13 h soaking time and 12 h cooling.

After the first annealing, the components go back to the workshop for the final machining. A second annealing follows to remove possible additional stresses.

4.2 Cleaning procedure

4.2.1 Material tests

When the production of the source components is finished, they need to be cleaned very carefully before they can be used in the SNO+ detector. Alconox [Alc14] is a detergent that removes general impurities and was used on the AV. Cleaning steps with a 1% Alconox solution are included on all parts of the source. Nitric acid is used in a solution of 1 mol/l on acrylic to remove metallic contaminations. For steel and titanium a 1% Citranox solution [Cit14] is used instead. Deionized water (DIW) and ultrapure water (UPW) remove remnants from the cleaning detergents.

Ethanol is a solvent that was considered for cleaning on all source parts as well. However, according to the data sheets of three different vendors only ethanol in lower concentrations is compatible with acrylic. A test series with different types of acrylic was done to determine if it can be used to clean the acrylic source parts. An alternative to ethanol is 2-propanol which was tested as well. All cleaning steps will be done in an ultrasonic bath to enhance the efficiency.

The smallest part of the acrylic source components is the lid with a thickness of 3 mm. In the first test series 6 acrylic samples with a thickness of 3 mm and 3.5 mm were tested

for material strength. The diameter of the samples was 8 mm. They were tested in an ultrasonic bath which was equipped with a heater to test the response at higher temperatures as well.

Additionally to a visual inspection of the surfaces, the stress in the samples was checked before and after each test. This was done by using polarized light and polarizing glasses. The samples were also weighted before and after the tests. The test parameters and results are summarized in Table 4.1.

Table 4.1: Results of the first test samples for different possible cleaning steps.

#	Test type	t / min	T / °C	Weight / mg before	Weight / mg after	Results
1	acetone	10	25	185	157	bubbles, obvious damage
2	pure eth.	60	30-55	214	226	bubbles on surface, soft material
3	water	68	45-54	183	188	no change
4	pure eth.	8	25	215	219	fine crack lines
5	30 % eth.	14	25	212	215	one crack
6	pure 2-prop.	8	25	180	181	fine crack lines

Acetone is known to be incompatible with acrylic, the first test was only done for comparison of the damage. When the second sample in pure ethanol at around 40 °C failed, the three following samples were tested to find the reason. The third and fourth were done to check if the high temperature in the ultrasonic bath lead to the breaking of the sample. With samples 5 and 6 a lower concentration and the alternative of 2-propanol were tested.

All samples except for the one in water were already damaged after a short period of time. The weight also changed slightly, probably due to absorption of water or ethanol. In samples 4 and 6 slightly less stress was observed after the test, apart from that the stress did not change noticeably. The 6 samples after the test are shown in Figure 4.5.



Figure 4.5: Broken samples after the first ethanol test.

The two possible reasons for acrylic breaking are either the small size of the samples which means there is few material to absorb stress or a low quality of the acrylic. To check for both possibilities a new test series was done with larger samples from three different vendors.

The second test series consisted of 11 acrylic samples from three different vendors with a diameter of 14 mm and a thickness of 3 mm each. These are close to the dimensions of the inner container lid. 4 samples are from the stock of TU Dresden, 4 are from the company Röhm and the last 3 are from a vendor of the former GDR. The test environment is the same as for the first test. The test parameters and results are shown in Table 4.2.

Table 4.2: Results of the second test samples (14 mm diameter and 3 mm thickness) with different cleaning conditions.

#	Test type	t / min	T / °C	Weight / mg before	Weight / mg after	Results
Stock TUD						
1	pure ethanol	60	23-38	544	544	surface opaque
2	pure ethanol	60	41-44	546	546	surface opaque
3	pure 2-propanol	60	23-38	548	548	surface opaque
4	pure 2-propanol	60	41-42	549	549	surface opaque
Röhm						
1	pure ethanol	60	23-38	565	565	surface opaque
2	pure ethanol	60	35-42	560	560	surface opaque
3	pure 2-propanol	60	23-47	577	575	fine cracks
4	pure 2-propanol	55	41-43	551	551	fine cracks
GDR						
1	pure ethanol	60	37-38	548	548	surface opaque
2	pure ethanol	60	39-44	547	547	surface opaque
3	pure 2-propanol	60	41-43	550	550	surface opaque

The first sample of each vendor was tested at room temperature and the second one at about 40 °C in pure ethanol. When using the ultrasonic bath a temperature increase of up to 38 °C was possible without additional heating during 60 min of cleaning. The third and fourth sample were tested at both temperatures with 2-propanol instead of ethanol.

In all cases except for the 2-propanol with Röhm samples, no real damage or weight difference like in the first test was observed. The only difference was a slightly more opaque surface after the test (cf. Figure 4.6). None of the samples showed a difference in the stress after the test.



Figure 4.6: Acrylic sample 3 of Stock TUD before (left) and after the test (right). An increase of opacity is visible.

It seems that the larger size and the different source of the acrylic have improved the test results. However, a change of the surface cannot be accepted for the calibration source because it is a sign for damage of the material. It was therefore decided to leave out the steps with ethanol cleaning for the acrylic parts.

4.2.2 Detailed cleaning steps

Before the titanium cylinder gets finally activated, all parts that will make the final container will be thoroughly cleaned. For this purpose a class 100 clean room is available in the same building where the activation is done. A detailed procedure was written for the cleaning of the calibration source components. The full cleaning procedure is attached in Appendix A.2.

The general procedure is to put the component with tweezers into a beaker, fill the beaker with a cleaning detergent and put the beaker into the ultrasonic bath. All needed tools such as beakers and the tweezers are always cleaned with alconox and deionized water (DIW) before they are used. Powderfree gloves are used and they are changed after every step. The solutions are generally prepared with DIW and very pure ethanol is used for the cleaning of the metal parts. Whenever the components are wiped or dried, cleaning tissues from Kimtech are used because of reduced lint.

All metal parts such as the titanium cylinder, the screws, the cross dowels and the wires are cleaned according to the following steps:

- 10 min bathing in Alconox (10 g/l DIW)
- 60 min bathing in pure ethanol
- 15 min bathing in DIW

- wipe with Alconox
- wipe with ethanol
- 15 min bathing in DIW
- 15 min bathing in Citranox solution (10 g/l DIW)
- 15 min bathing in ultra pure water (UPW)

The cleaning procedure of the acrylic parts is similar but without ethanol and with nitric acid instead of Citranox:

- 10 min bathing in Alconox
- 15 min bathing in DIW
- wipe with Alconox
- 15 min bathing in DIW
- 5 min bathing in nitric acid solution (1 mol/l DIW) at 40 °C
- rinse with UPW
- 5 min bathing in nitric acid solution (1 mol/l DIW) at 40 °C
- 15 min bathing in UPW

The three steps of the cleaning procedure for the FFKM O-rings are:

- rinse and wipe with Alconox
- 10 min bathing in Alconox
- 10 min bathing in UPW

After the cleaning each part is packed in a cleaned Polypropylen plastic bag. Then the bags are flushed with nitrogen and heat sealed.

For the irradiation the titanium cylinder is bagged four times. The first bag is removed after the activation in the pre-hall that leads to the neutron generator room, the second one in the room of the Ge-detector before the counting, the third after the counting and the fourth inside the clean room before the assembly. When the source and the containers are assembled they are bagged under nitrogen atmosphere. An additional radon tight bag will reduce the radon contamination during the shipping to the SNO+ detector. The outer container is shipped to SNO+ site seperately to avoid cross contamination during the cleaning procedure.

4.3 Pressure tests

If LAB enters the containers during the calibration of the SNO+ detector it is possible that parts of Ti and Sc are washed off and dissolve in the LAB. A double encapsulation system as described in Section 4.1 is designed to avoid this scenario. Each of the two containers has to be tight for LAB under the expected pressure and for the period that it will stay in the detector.

The highest expected pressure at the bottom of the LAB filled AV is 1.54 bar. If the containers are tightly closed on surface, the 2000 m difference in height adds 0.23 bar. Together that is a maximum overpressure of 1.77 bar that the containers have to withstand. The expected calibration time with the scandium source is less than 24 hours even with a calibration in multiple positions in the detector.

The tests were done with pressures between 3.8 bar and 7.0 bar and the duration times vary between two and five days which is in both cases more than twice the expected amount.

4.3.1 Chamber design

The pressure chamber was originally designed as a metal cylinder with an attached barometer and an adjustable spring. An access screw on the top (1) allows the LAB filling, while the pressure is adjusted using the spring (2). The spring also acts as a buffer to compensate for lost pressure inside the chamber. A schematic view of the chamber design is shown in Figure 4.7.

However, when the setup was tested it was not possible to set the pressure with the spring and a replacement with a stronger spring brought no improvement as well. According to the workshop, a reason might be the friction inside the guide bar that blocks the spring from applying pressure. In a next attempt the spring was replaced by a steel bar. High pressures could be applied properly but lacking a buffer atmospheric pressure was reached within 1 to 2 hours. It seems that the oily LAB can get lost in parts of the chamber such as the guidebar which causes the

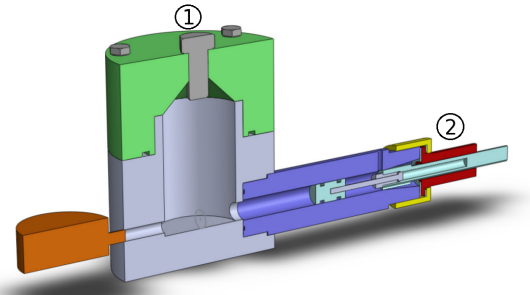


Figure 4.7: Sketch of the first design of the pressure chamber [Dom13].

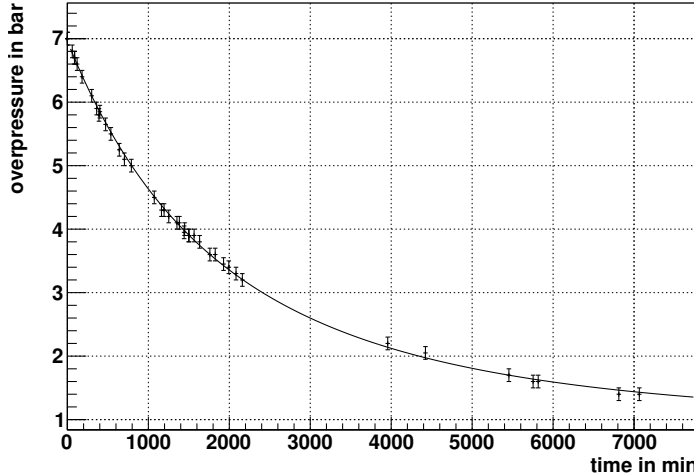


Figure 4.8: Decrease of the pressure in the chamber over time.

pressure to decrease too fast. With necessary adjustments every hour a testing period of more than one day was not possible.

The problem was solved by changing the screw at the inlet (1) into an access for pressurized air. With the new design the chamber can be connected to pressurized air from the laboratory supply and about 7 bar overpressure are reached. For safety reasons the air supply is stopped after filling the chamber. As a consequence the pressure decreases slowly. With air in about half the chamber acting as a buffer the chamber has to be refilled only twice a day to sustain pressures above 3.8 bar. The decrease of the pressure over time was measured and is shown in Figure 4.8. After 24 hours the pressure is reduced by a factor of 0.57.

The errors shown in the Figure are the reading errors on the barometer and are estimated to be 0.1 bar. The used fit function is a double exponential function with three free parameters:

$$f(x) = ae^{bx}e^{cx} \quad (4.1)$$

and the fit parameters are shown in Table 4.3.

Table 4.3: Fit parameters for the double exponential fit function of the measured pressure decrease.

a	b	c
0.9789	1.9614	-0.00023248

For the analysis the fluorescent properties of LAB mixed with 2,5-Diphenyloxazole (PPO) under ultraviolet (UV) light were used. The LAB that was used in the tests was

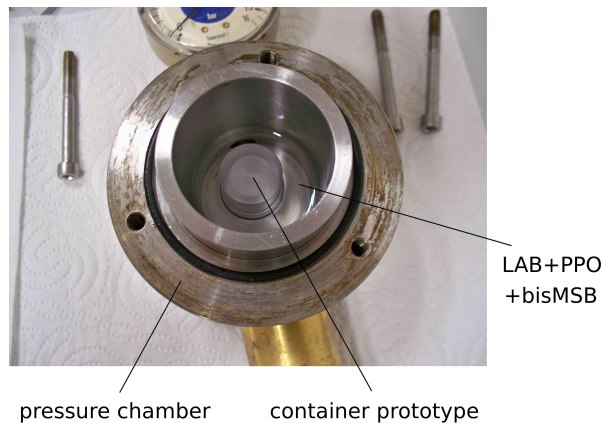


Figure 4.9: Open pressure chamber with LAB mixture containing PPO and bisMSB. At the center the acrylic outer container is shown.

mixed with 3 g/l of PPO and additionally with 15 mg/l of 1,4-Bis(2-methylstyryl)benzene (bisMSB) to enhance the fluorescence. A picture of the open chamber with the LAB mixture and the outer container inside is shown in Figure 4.9. The container was placed with the lid facing down into the chamber to ensure a liquid level well above the sealing O-ring.

4.3.2 Analysis

A UV lamp was used to check for LAB leaking into the container. An image of the fluorescent liquid on the acrylic of the outer container is shown in Figure 4.10.

Since only a small amount of LAB (if any) is expected to leak inside the container, the fluorescence light directly on the acrylic is too weak to be detected by eye. The fluorescence of LAB on paper towel is stronger and smaller amounts can be detected. To use the fluorescence effect for the analysis a piece of paper towel was placed inside the container directly below the thread. In Figure 4.11 the fluorescence light of the LAB mixture on a paper towel is shown.

Additionally an inspection was done by eye with normal light. It is possible to identify parts that are wet with LAB on the acrylic due to the changing reflectivity of the surface. In Figure 4.12 a close look on the body of the outer container is shown. The O-ring edge was checked for leaked LAB by eye. On the inner edge the paper towel piece was placed and used to check with UV light for LAB leakage after each test. In Figure 4.13 the piece of paper is shown under UV light. No fluorescence light is visible which means no LAB reached the paper in that test.

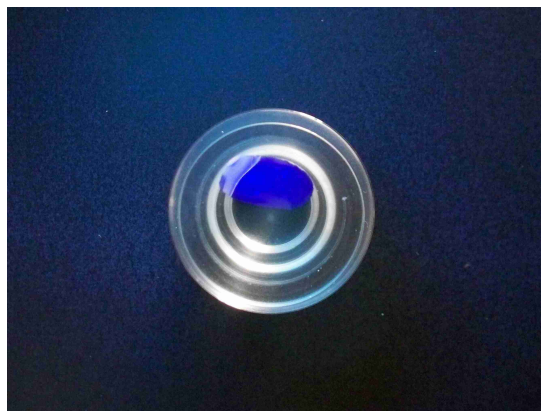


Figure 4.10: LAB+PPO+bisMSB on top of the outer container under UV light.

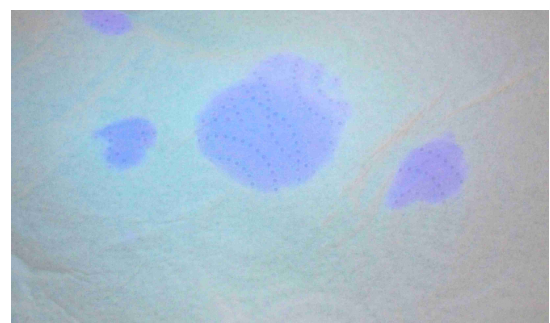


Figure 4.11: Spots that are seen show the fluorescence light of LAB+PPO+bisMSB on a paper towel under UV light.

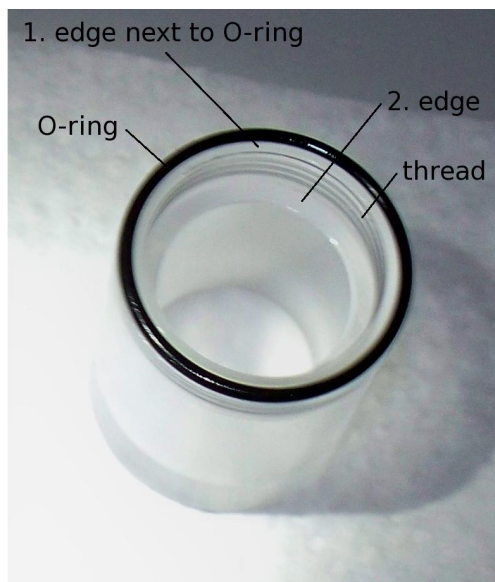


Figure 4.12: Outer container body part with O-ring. Highlights are the O-ring edge, the thread for the lid and the inner edge.



Figure 4.13: Outer container body part with O-ring and piece of paper towel. No fluorescence is visible on the paper.

4.3.3 Results

Each pressure test period was about 4 days long with the exclusion of the first two tests. Three days before each pressure test the container was immersed in LAB without pressure.

Table 4.4: Results of the pressure tests.

#	t / d	p / bar	Results
1	2.0	4.3 - 7.1	1/4 of the 1. edge wet
2	3.0	3.9 - 7.1	1/2 of the 1. edge wet
3	4.2	3.8 - 6.9	1. edge dry
4	4.2	4.2 - 7.0	1. edge dry
5	4.2	3.8 - 7.0	parts of the thread wet
6	4.2	4.1 - 7.0	1/4 of the 1. edge wet
7	4.2	3.8 - 6.9	1. edge dry

In 3 of 7 tests no LAB was detected behind the O-ring at the level of the first edge. The results from test 3 are shown in Figure 4.14. It can be seen that the outer edge is shining which is a sign of wet. The O-ring is also shining where it was in contact with LAB. For comparison the lid of the outer container is shown in Figure 4.15. In none of the tests a leakage of LAB below the paper towel piece was detected with the UV lamp.



Figure 4.14: Outer container body after the pressure test. The O-ring edge is wet with LAB but all other parts are dry.



Figure 4.15: Outer container lid after the pressure test. The O-ring edge is wet with LAB but all other parts are dry.

Under the high pressure test conditions it was possible that a small fraction of LAB entered the outer container just behind the O-ring. In only one case it reached the thread. There are a few possible reasons that could have caused this problem. When the container was carefully reopened after the test, LAB could have leaked inside during the unscrewing operation. Even though the container and O-ring were always cleaned before the test, small impurities could have been trapped below the O-ring, creating a minimal gap through which LAB could have leaked. Another reason might be the differences in the closing tightness of the container at the beginning of each test.

Concluding, the design of the outer container was found to be good enough to prevent any significant leakage. Once the final containers are produced the tests will be redone.

4.4 Ink tests

After the pressure checks for the outer container, the tightness of the inner container was tested as well. This test is important to ensure that the inner container can withstand the cleaning procedure (in particular an ultrasonic cleaning) once it is equipped with the activated titanium sample. It was done by filling the inner container with ink and checking for leakage in an ultrasonic bath with DI water. Due to the shape of the container it was only possible to fill about half of the inner volume. The container was tested upside down to ensure contact of the ink with the inside of the O-ring. The test setup is shown in Figure 4.16.

Even if no additional heat is turned on, the temperature of the container increases due to the ultrasonic bath. This adds pressure inside the container which it has to withstand as well.

At first the tightness of the container was tested in water for 48 hours without ultrasonic. No visible ink leakage was observed.

A first series of 6 tests in ultrasonic bath of water followed. Each test was done for 60 min and leakage checks were done by eye at least every 5 min but more frequently at the beginning. Before each test the container was opened and the O-ring was turned around to ensure a new setup.

The first two tests showed leakages in the form of small threads of ink that were released at a certain spot of the O-ring. This was due to small misplacements of the O-ring or a weak closing of the container. In tests 3 to 6 no leakage occurred which shows that the design of the container is in principle strong enough but needs some adjustments.

In a first attempt thicker O-rings were tested to increase the surface area between O-ring



Figure 4.16: Inner container filled with ink in water.

and acrylic. 6 out of 7 tests showed no leakage in that second test series but the problem with the closing remained and one test failed.

For an easier and tighter closing of the container a slit was added into the lid following the design of an earlier prototype. Using a plastic rod for screwing it is easier to tighten the lid and properly adjust the O-ring (cf. Figure 4.17). 7 final tests with the thin O-ring were performed and no leakage was observed.



Figure 4.17: Inner container lid with slit (left) and plastic rod used for screwing it (right).

The tests showed that the inner container has to be closed properly to ensure its tightness. This can be achieved with a slit machined in the lid of the inner container. If closed correctly, the container is tight for ink in an ultrasonic bath of DI water and the final design can be used for the calibration source.

5 Calibration source implementation in RAT

5.1 SNO+ software: RAT

The simulation software used by the SNO+ collaboration is the Reactor Analysis Tool (RAT). It combines the Monte Carlo (MC) simulation for the Braidwood detector with event-based analysis tasks. This includes position and energy reconstruction. It is based on “GEANT4” (GEometry ANd Tracking) and “GLG4sim” (Generic LAND Geant4 simulation), which is a software developed for Monte Carlo simulations of particles going through matter [A⁺03]. RAT is written in C++ and the data is stored and analysed with ROOT, a program for efficient analysis of large amounts of data. GEANT4, GLG4sim and ROOT are developed by CERN and RAT is under constant development by the SNO+ collaboration [SNO14a]. For the simulations in this thesis versions 4.2 to 4.5 of RAT and version 5.34 of ROOT were used.

In RAT the specific information for the simulations are stored in a database. The geometry of the sources is hard coded but the sizes and materials of the different components can be changed in geometry files (.geo). This allows easy adjustments, because no recompiling is required in this case. Information about materials, optics and surfaces are stored in separate database files (.ratdb). Changing or adding new materials or properties can be easily done through access to these files. Simulating the detector response to the calibration sources, for instance, is extremely important to tune the source dimensions and material in order to find a geometry that will give the best results during the calibration. The goal is to have a geometry with minimal energy loss inside the source and maximum energy deposition in the scintillator.

In RAT the full detector response is simulated which includes the scintillation light physics process and the electronics response from the PMTs. Several analysis tools have been developed to fit the deposited charge and obtain information on energy and position. The amount of photons triggering the PMTs (Nhits) and the energy and position reconstruction is simulated as well. The data is stored in a .root file.

The data in the .root file is divided into two main branches. The data that will be accessible in the actual measurements after analysis by the electronics goes into the event (EV) branch. The Monte Carlo (MC) branch holds the detailed information on the simulated particle like tracks and exact energy depositions in each volume. Combining the MC and EV information it is possible to do a detailed study of the calibration source, for instance, analyzing the advantages or disadvantages of different geometries.

ROOT provides an interactive mode to analyze the data but it is more convenient to

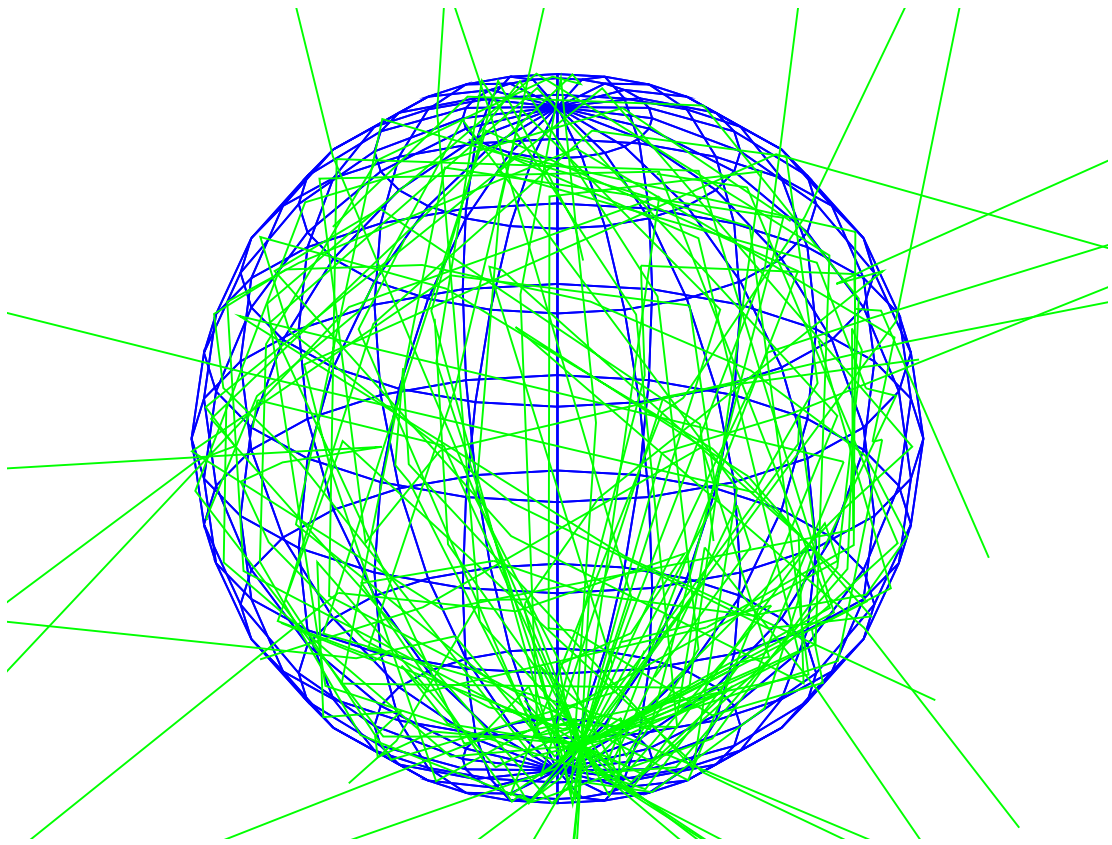


Figure 5.1: Simulated tracks of scintillation photons (green lines) for a 10 keV gamma event inside the LAB filled AV (blue lines).

use macro files which are written in C++. With the macros the particularly interesting data can be extracted from the .root files to decrease the file size and increase processing speed. The data can be processed to create plots and fitting functions for the analysis.

Like ROOT, RAT can be run interactively but usually macro files are used where all commands are listed. At the beginning of the macro the detector geometry is loaded. Any additional geometry, like calibration sources, are also specified at the beginning. Once the geometries are defined, the processors are specified in the event loop. The event loop includes the electronics chain (data aquisition) and the fitter structure. The output directory and file are also defined inside the event loop.

In the last part of the macro the event generators are specified. Several generators are available for different sources and primary particles. To indicate decay chains like U and

Th where secondary isotopes are emitting radiation as well, and isotopes with several decay modes such as IT, EC, β^+ and β^- , a decay chain generator was written. Using its functionality a generator specifically for the ^{48}Sc source was developed. The usage is described in Section 5.3.

The tracks of the simulated particles and the used geometries can be written into an XML format using HepRep. They are then visualized with the associated java browser application HepRApp. In Figure 5.1 the tracks of the scintillation photons caused by a 10 keV gamma event inside the AV filled with LAB are shown.

5.2 Development of a geometry tool for the scandium source

Geometries in RAT are defined using the GEANT4 objects such as cubes, cylinders or polycones (objects made of many cylinders with different diameters). In logical volumes the shape and the material are combined to one object. A vector object holds the information of the position for the logical volume and can be set relative to other logical volumes.

The geometry of the ^{48}Sc source simulated in RAT is shown in Figure 5.2. It consists of a titanium cylinder in which the scandium isotopes are evenly distributed. The titanium cylinder (red) is surrounded by an inner (blue) and an outer container (green). A holder (brown) is connected to the outer container by 3 screws and 3 cross dowels. The holder is then connected to a weight cylinder. The further connection of the source to the umbilical is not simulated yet.

The source is coded in two files named:

```
GeoSc48SourceFactory.cc  
GeoSc48SourceFactory.hh
```

These files contain all the geometry objects that constitute the source. The geometry parameters such as size and material of the different volumes can be changed by settings in the file:

```
Sc48Source.geo
```

In this way it is possible to test different geometries without recompiling the code.

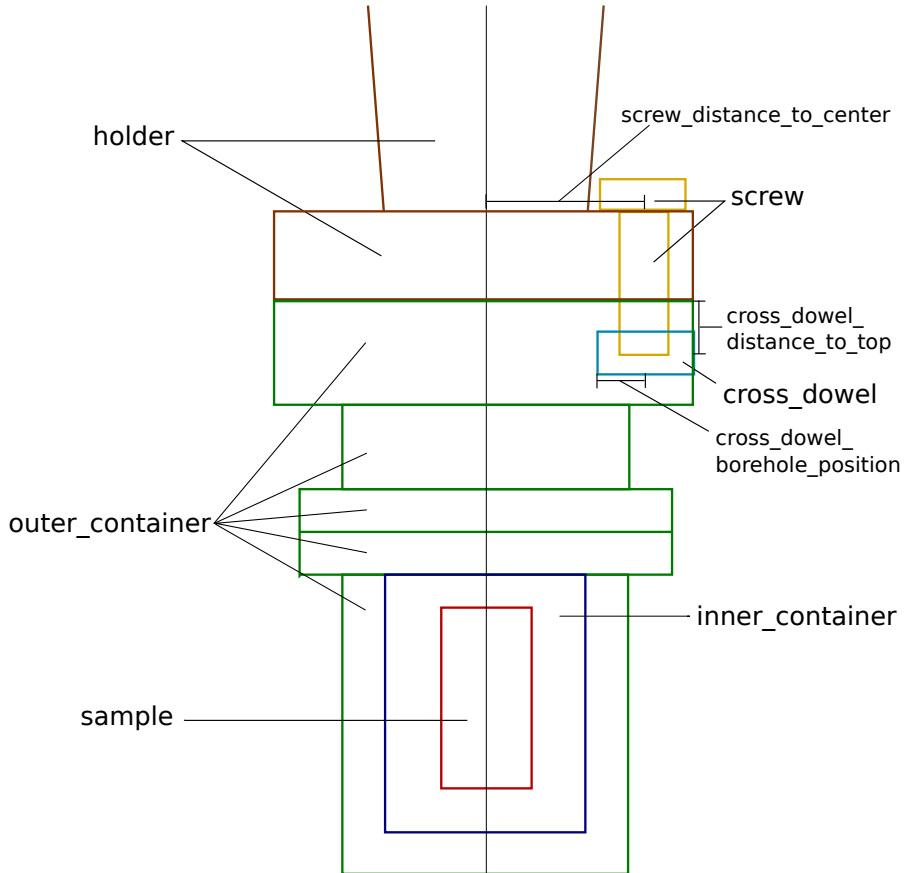


Figure 5.2: Scheme of source, containers and holder for illustration. Adjustable position parameters are shown as well. The labels are according to the names in the source code.

The containers have been included in RAT based on the technical drawings of M. Siegel. The active source is a titanium cylinder of 12.7 mm height and 6.35 mm diameter enclosed in an acrylic inner container. Both the sample and the inner container are shaped as a cylinder.

The outer container is made of acrylic as well and has a more complicated shape. The base and the lid have a flat collar with holes at the point where they connect. A stainless steel wire passes through the holes to fasten the closure. The lid is shaped in order to host three cross dowels. The cross dowels are used to avoid the release of the screws during movement in the vessel. In RAT the outer container and the holder are shaped as a polycone.

Where it is reasonable, some dimensions cannot be set manually but are calculated au-

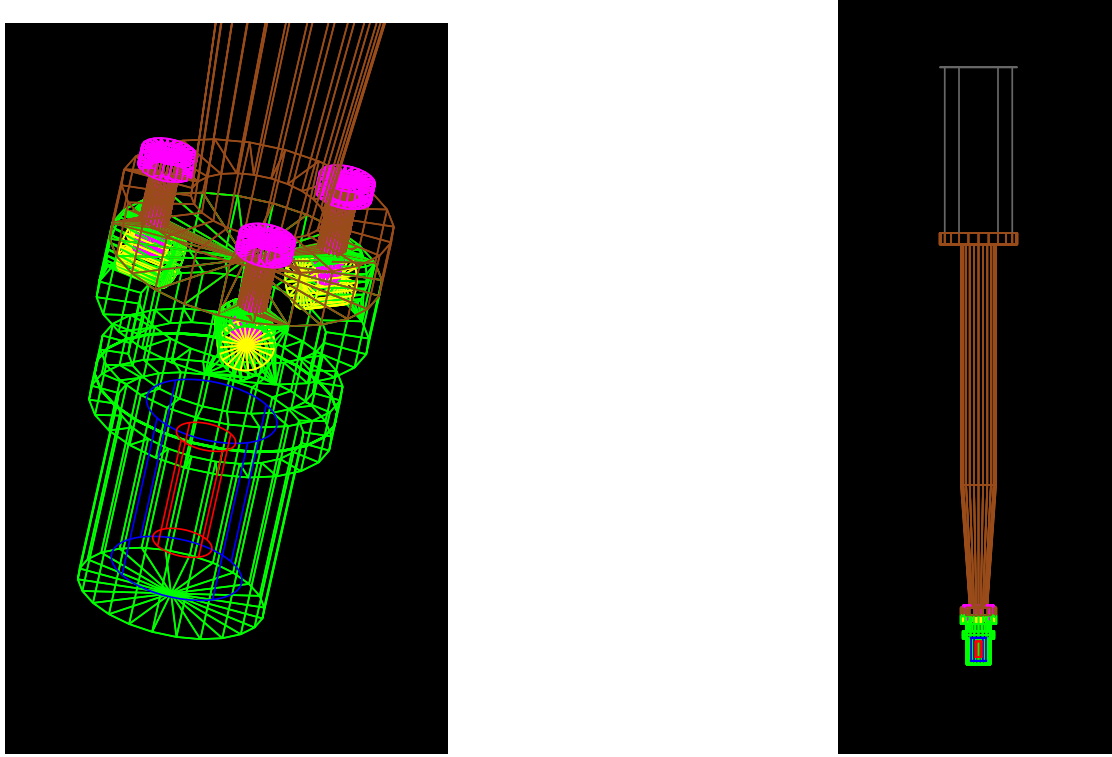


Figure 5.3: Source geometry in 3D projection (left) and view from distance with weight cylinder (right).

tomatically relative to others which reduces the amount of free parameters. The screw length for example is calculated so the screws start right above the holder and end in the middle of the cross dowels. Also the positions are set by only a few parameters, e. g. the screw position is set by the variable `screw_distance_to_center` and all three screws positions are calculated from that. A sketch of the source and its containers is shown in Figure 5.2. The variable names of the objects in the .geo file are as shown, which are the following:

sample: This is the titanium cylinder with the scandium isotopes. It is defined as a cylinder. The radius and height can be changed. At default its center corresponds to the center of the AV.

Standard dimensions: 12.7 mm height; 3.2 mm radius.

inner_container: This is defined as a cylinder whose radius and height can be changed. The material is acrylic.

Standard dimensions: 18.8 mm height; 7.0 mm radius.

outer_container: This is defined as a polycone where the height and diameter of each part can be changed. A small gap is added at 24 mm for a visible border between the base and the lid. The material is acrylic.

Standard dimensions:

heights: 0.0 mm, 21.0 mm, 21.0 mm, 24.0 mm, 24.0 mm, 24.1 mm, 24.1 mm, 27.0 mm, 27.0 mm, 33.0 mm, 33.0 mm, 43.0 mm;
radii: 10.0 mm, 10.0 mm, 13.0 mm, 13.0 mm, 13.0 mm, 13.0 mm, 13.0 mm, 13.0 mm, 10.0 mm, 10.0 mm, 14.6 mm, 14.6 mm.

holder: The holder connects the weight cylinder to the outer container. It is defined as a polycone where each height and diameter can be changed. The standard material is PTFE but simulations with acrylic showed better results.

Standard dimensions:

heights: 0.0 mm, 6.4 mm, 6.4 mm, 106.1 mm, 302.1 mm, 302.1 mm, 311.5 mm;
radii: 14.6 mm, 14.6 mm, 7.2 mm, 14.3 mm, 14.3 mm, 31.8 mm, 31.8 mm.

weight_cylinder: The weight cylinder is needed for the movement of the source in the LAB as it provides additional weight. It is defined as a cylinder whose height and radius can be changed. The material is stainless steel. It is visible at the top of the right picture of Figure 5.3.

Standard dimensions: 134.9 mm height; 31.8 mm radius.

Some of these volumes can be enabled or left out to allow simulations with only parts of the calibration source setup. This is done by setting the arguments with the word “enable” to 0 or 1. The holder, the weight cylinder, the screws and their holes can be enabled, but some combinations (e.g. weight cylinder on but holder off) are not possible due to the relative position setting.

All units used in the .geo file are given in mm. In the source file the volume names have the prefix “Sc48Source_” so they are not confused with other calibration source names. The position of the sample can be set all around the AV. At default the center of the titanium cylinder coincides with the center of the vessel. The other volumes positions are then calculated relatively to this position.

The simulated geometry was visualized using HepRApp. In Figure 5.3 a 3D projection of the sample, its containers and part of the holder is shown on the left side. The right side shows the distant view of the whole calibration source setup. In Figure 5.4 the projections from the top (left picture) and from the side (right picture) are shown.

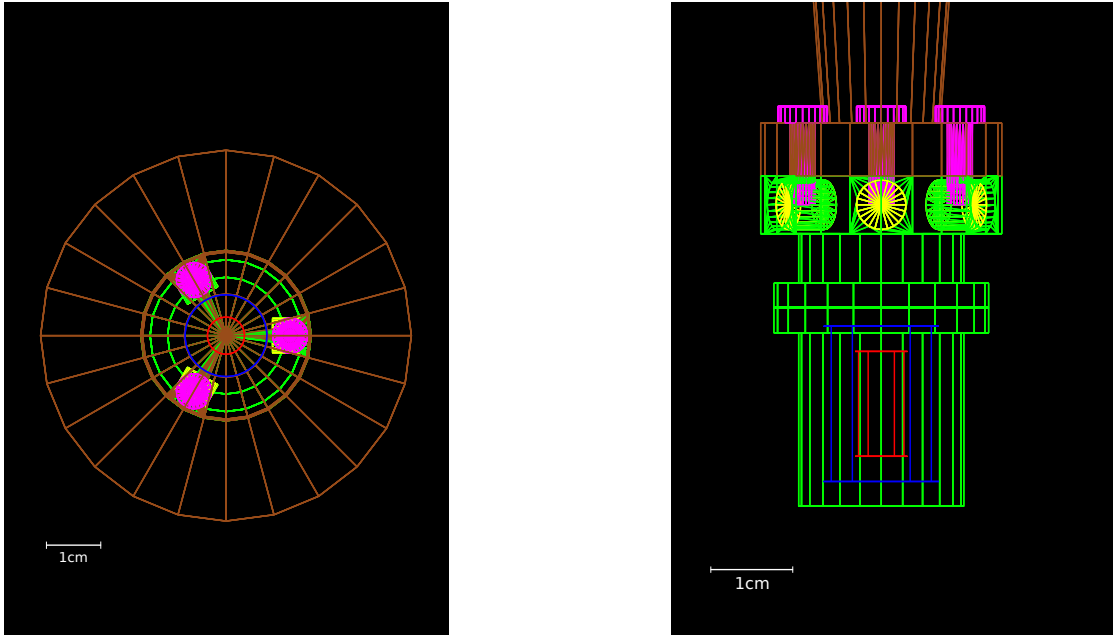


Figure 5.4: Top view (left) and side view (right) of the source container and holder.

5.3 Development of a generator tool for the scandium source

In RAT events are created by particle generators that are called in the macro file. With the generator the position in the detector, the time and the kind of primary particle as well as its energy are determined. It is allowed to use more than one generator at a time. It is possible to set the rate of each generator to simulate different activities.

The general line for adding generators in the macro file is:

```
/generator/add gen_name generator_options
```

As seen in Chapter 3 the production of scandium by neutron irradiation on ^{nat}Ti results in the three main isotopes ^{46}Sc , ^{47}Sc and ^{48}Sc . The relative activities depend on the distance to the DT generator head and the irradiation time. To reduce the sources of mistakes, a generator was specifically written for the scandium source. The generator assigns the production of the isotopes in the sample geometry. An additional time parameter, which represents the time since activation, determines their relative activities

that change according to their half lives.

The source is coded in the files:

`Sc48SourceGen.cc`

`Sc48SourceGen.hh`

A typical generator command for the ^{48}Sc is defined as:

```
/generator/add gen_name 48Sc:A1 47Sc:A2 46Sc:A3 DecayTime:T
```

where `gen_name` is `sc48source`, A_i are the activities (in Bq) of the 3 nuclides directly after the irradiation. The decay time T (in Geant4 units) is the time between the end of irradiation and deployment of the calibration source in the SNO+ detector as specified in Chapter 3. One, two or three isotope arguments can be set to start the simulation. When only one or two isotopes are simulated the corresponding activity for the rest is set to 0 or left out. If no time argument is given, the initial activities will be used, i. e. no lapse of time.

The position of the generator inside the AV is defined relative to the scandium source geometry and it is fixed to be always inside the titanium cylinder. It is further assumed that the simulated events are uniformly distributed. The position can be modified only by changing the position of the scandium source through the command line:

```
/rat/db/set GEO[Sc48Source] sample_position [0.0, 0.0, 0.0]
```

6 Analysis of simulation data

6.1 Simulation of scandium isotopes

In the SNO+ detector gamma rays are detected via scintillation light in the LAB. Because the mean free path of a 1 MeV photon in LAB is about 50 cm which is small against the 6 m radius, all gammas from a decay cascade at center position are fully converted into optical photons. The energy of an event is then proportional to the number of PMTs that triggered at least once (Nhits). This means that most decays are detected with their sum energy which is contrary to standard germanium detectors where usually only one gamma is detected from a decay cascade and the TCS peaks are small. The 1σ energy resolution of the detector is at around 4.5 % in 0.3 % tellurium loaded scintillator at 2.5 MeV [Mai14]. This is a preliminary value which can be improved by increasing the light yield.

The full energy peak of ^{48}Sc consists of two overlapping Gaussians in the Nhits spectrum. The decay of ^{48}Sc releases three gammas with a sum energy of 3.333 MeV in 90 % of the cases and three or four gammas with 3.509 MeV in 10 % of the cases (cf. Figure 3.7). Due to the proximity of the two energies and the higher probability for the 3.333 MeV sum energy, the Gaussian at 3.509 MeV cannot be distinguished. In Figure 6.1 the Nhits

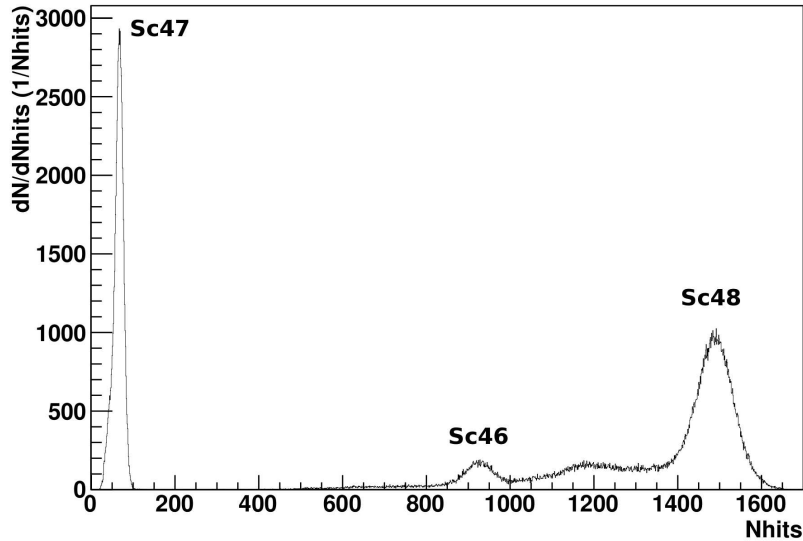


Figure 6.1: Simulated Nhits (PMT hits) spectrum for ^{46}Sc (2.01 MeV), ^{47}Sc (0.16 MeV) and ^{48}Sc (3.33 MeV). 300,000 events were simulated in LAB 6 days after activation.

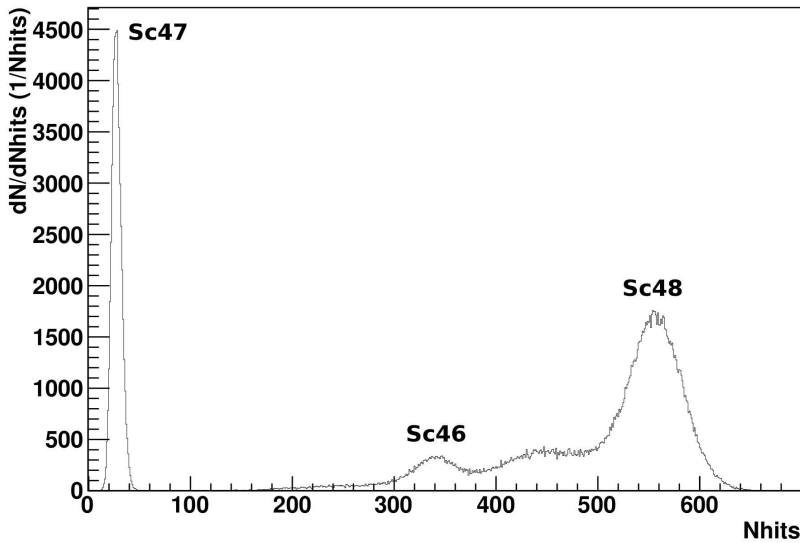


Figure 6.2: Simulated Nhits (PMT hits) spectrum for ^{46}Sc (2.01 MeV), ^{47}Sc (0.16 MeV) and ^{48}Sc (3.33 MeV). 300,000 events were simulated in LAB loaded with 0.3 % of natural tellurium 6 days after activation.

spectrum from a simulation with all three scandium isotopes in a contained source in LAB is shown. The isotopes corresponding to each peak area are indicated. The light yield in pure LAB is about 500 Nhits / MeV. The relative activity of the isotopes corresponds to an estimated shipping time of 6 days after the activation. The events are distributed equally inside the titanium cylinder. Electrons from the beta decay are absorbed by the source container in > 99 % of the cases.

In Figure 6.2 the spectrum for the case of a 0.3 % natural tellurium loaded scintillator is shown. Due to increased scattering and absorption in the new cocktail the signal strength decreases to about 200 Nhits / MeV.

The events between the peaks of ^{46}Sc and ^{48}Sc are decays of ^{48}Sc which lost energy inside parts of the source container and do not contribute to the full energy peak. About 50 % of the ^{48}Sc events deposit the full energy.

For the analysis the peaks were fitted. The main interest lies in the ^{48}Sc and ^{46}Sc . For the ^{48}Sc four different fitting functions were tested and the most reasonable is a double Gaussian:

$$f(x) = a_1 e^{-\frac{1}{2} \left(\frac{x-b_1}{c_1} \right)^2} + a_2 e^{-\frac{1}{2} \left(\frac{x-b_2}{c_2} \right)^2} \quad (6.1)$$

where one Gaussian is fitting the full energy peak at the maximum of the spectrum and the other one is fitting the events that did not deposit the full energy in the scintillator. With the Monte Carlo (MC) information it is possible to plot only the events outside the full energy peak with less than 3.1 MeV energy deposition. As shown in Figure 6.4 the shape of the histogram justifies the fit with the right tail of a Gaussian.

A third Gaussian for the second peak energy at 3.509 MeV was considered as well but due to the small peak and the large energy resolution it was not possible to fit an additional Gaussian there. This results in a slight deviation of the fitting function from the data points at the maximum and at the high energy tail (around 1600 Nhits) where the 3.509 MeV peak is barely visible. In Figure 6.3 the ^{48}Sc peak fit function is shown. The

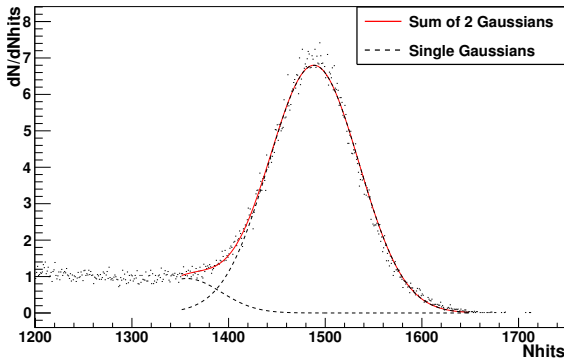


Figure 6.3: ^{48}Sc peak with the double Gaussian fit (red) and the two single Gaussians (dashed black) in pure LAB.

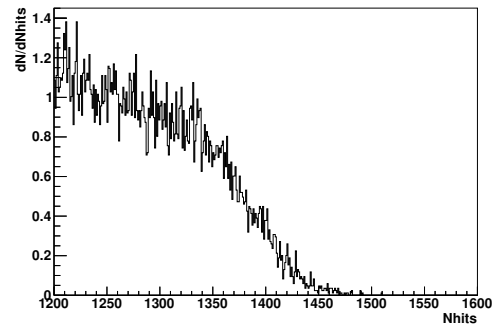


Figure 6.4: Nhits outside the full energy peak with total scintillation energy deposition of less than 3.1 MeV.

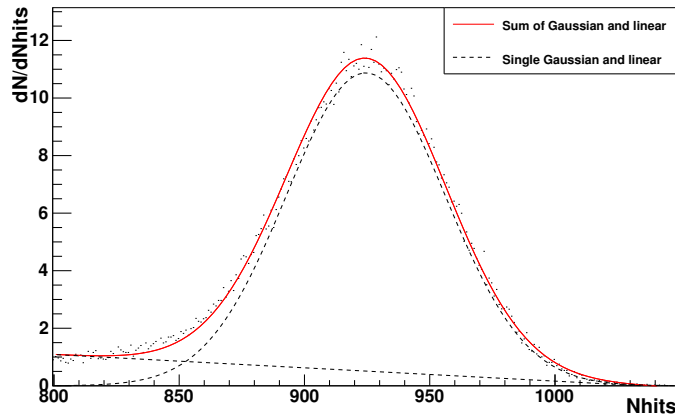


Figure 6.5: ^{46}Sc peak with the fit of a linear function and Gaussian (dashed black) as well as their sum (red) in pure LAB.

two Gaussians and their sum are visible.

The peak area of ^{46}Sc was fitted by:

$$f(x) = ae^{-\frac{1}{2}\left(\frac{x-b}{c}\right)^2} + dx + e \quad (6.2)$$

In Figure 6.5 the fit of the ^{46}Sc peak with the sum of the linear function and the Gaussian is shown. This fit was done for a simulation with ^{46}Sc alone without background from ^{48}Sc decays in the peak area.

Parameter limits were set to constrain the functions to reasonable areas. The peak position is the maximum of the single Gaussian. In Table 6.2 the fit parameters for the ^{46}Sc and ^{48}Sc peak fits are summarized.

**Table 6.1: Fit parameters with errors for the function in Equation 6.2 and χ^2 / ndf .
The function fits the ^{46}Sc peak in Figure 6.5.**

Isotope	a	b	c	d	e	χ^2 / ndf
^{46}Sc	10.88 (5)	924.5 (1)	31.78 (13)	4.786 (88)	-0.004623 (85)	1.808

**Table 6.2: Fit parameters with errors for the function in Equation 6.1 and χ^2 / ndf .
The function fits the ^{48}Sc peak in Figure 6.3.**

^{48}Sc	a ₁	b ₁	c ₁	a ₂	b ₂	c ₂	χ^2 / ndf
	6.801 (35)	1488 (0)	46.58 (25)	0.9457 (285)	1357 (4)	35.66 (348)	1.475

6.2 ^{46}Sc as additional calibration source

With a half life of 1.8 d the ^{48}Sc decays fast compared to the ^{46}Sc that has a half life of 83.8 d. This circumstance gives the possibility for an additional calibration of the SNO+ detector using ^{46}Sc when most of the ^{48}Sc has decayed. The advantage is that the same source could be used for a calibration at 3.333 MeV from ^{48}Sc and at 2.010 MeV from ^{46}Sc without the risk of additional contamination. To check the possibility to use the ^{46}Sc , shadowing and quenching studies were done (see Sections 6.3 and 6.4). As a possible hypothesis, it was considered that the scandium source is reused after one additional week. About 7 half lives passed for the ^{48}Sc which means a reduction of the activity of about 99.2 % since activation. The two spectra of simulations in LAB and 0.3 % tellurium loaded LAB 13 days after activation are shown in Figures 6.6 and 6.7.

In Figure 6.8 a blown up version of the simulation of the Nhits spectrum 13 days after

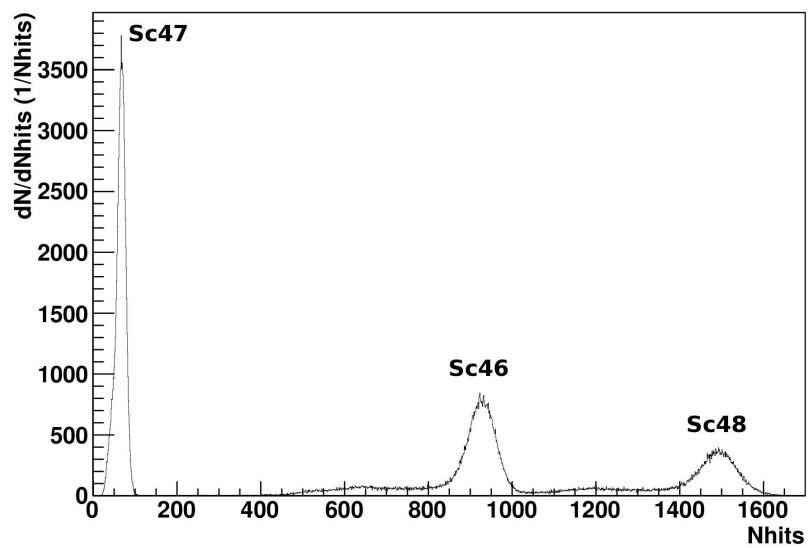


Figure 6.6: Simulation of 300,000 events with all scandium isotopes 13 days after activation in LAB. The peak of ^{48}Sc is small compared to ^{46}Sc .

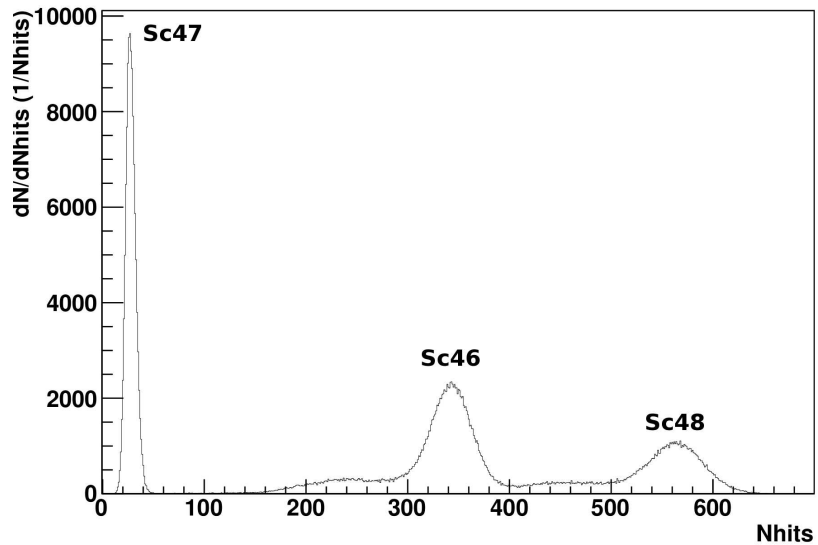


Figure 6.7: Simulation of 300,000 events with all scandium isotopes 13 days after activation in 0.3 % tellurium loaded LAB. The peak of ^{48}Sc is small compared to ^{46}Sc .

activation is shown. The fit of the ^{46}Sc peak with and without the background of ^{48}Sc is compared. Because of the low background of ^{48}Sc in the peak area of ^{46}Sc the peak position of ^{46}Sc changes by only 0.14 %.

If it is decided that the ^{46}Sc will be used as additional calibration source there is a possibility to increase the activity for ^{46}Sc . The titanium cylinder could be activated to higher activities than the 5000 Bq for ^{48}Sc which is an activity that stays safely below the exemption limit of 10^4 Bq for ^{48}Sc and allows shipping of the scandium source without a declaration as source¹. When the activity of ^{48}Sc is decayed below 5000 Bq the cylinder can be safely shipped but the activity of ^{46}Sc is higher. A possible scenario is an activation to an activity of 10^4 Bq for ^{48}Sc . After two days the activities would be at 4668 Bq (^{48}Sc), 118 Bq (^{46}Sc), 1770 Bq (^{47}Sc) and 27 Bq (^{47}Ca) based on the achieved activities listed in Table 3.8. In this case twice as much ^{46}Sc activity would be available for the calibration of the SNO+ detector.

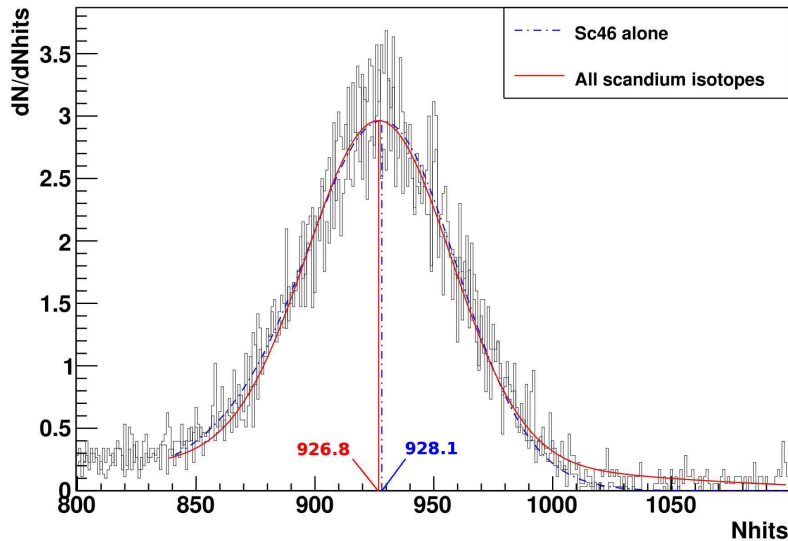


Figure 6.8: Comparison of the ^{46}Sc peak position with and without ^{48}Sc background in pure LAB 13 days after the activation.

¹Exemption limits for ^{46}Sc , ^{47}Sc and ^{47}Ca are at 10^6 Bq. Their impact on the cumulative activity of the source is negligible.

6.3 Shadowing of ^{46}Sc

The primary high energy gammas emitted in the decay have a high probability to escape the source container without energy loss. However, the scintillation light that is created afterwards, scatters in all directions and is possibly absorbed by components of the calibration source. This shadowing effect due to loss of scintillation photons reduces the Nhits.

The amount of lost Nhits due to shadowing in the container parts was studied for the ^{46}Sc and the effect on the newly designed container with screws and cross dowels was of special interest. The following three scenarios were simulated in LAB+PPO:

- ^{46}Sc as a point source
- ^{46}Sc inside the titanium cylinder with full containers
- ^{46}Sc inside the titanium cylinder with both containers, but without screws and cross dowels

Table 6.3: Peak positions and FWHMs obtained from the simulations of a point source and a contained source with and without screws and cross dowels.

	Full container	Container w/o screws & cross dowels	Point source
Peak position	928.6 (2)	929.9 (2)	946.0 (1)
FWHM	77.85 (35)	77.95 (35)	70.08 (23)

The comparison of the three peak positions and their full width half maximum (FWHM) is shown in Table 6.3. Only statistical uncertainties are given. The peak position in the simulation with the containers shifts by about 0.1 % due to the screws and cross dowels. The shadowing of the whole source in comparison to the point source is 1.8 %. The fitting functions are shown in Figure 6.9 and 6.10.

The shadowing affects the position of the peak. The peak position decreases because of small amounts of absorbed scintillation photons due to the size of the source container in every event. At the time of simulation, all scintillation photons hitting a stainless steel surface were absorbed because reflection was not implemented in RAT. Although the screws and cross dowels are made of stainless steel their effect on the shadowing is small because of their small dimensions. In contrast to the contained source where some gamma events lose energy inside the container parts, all events from the point source are detected inside the full energy peak. This explains the difference of the peak height in Figure 6.9. About 32.3 % of the gamma events from ^{46}Sc lose energy inside the container.

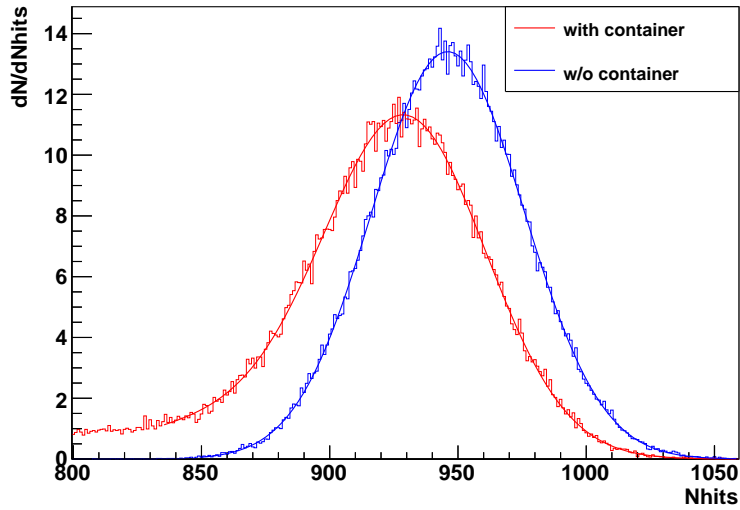


Figure 6.9: Simulated ^{46}Sc as point source and with full container. All events from the point source are inside the full energy peak and no shadowing occurred there.

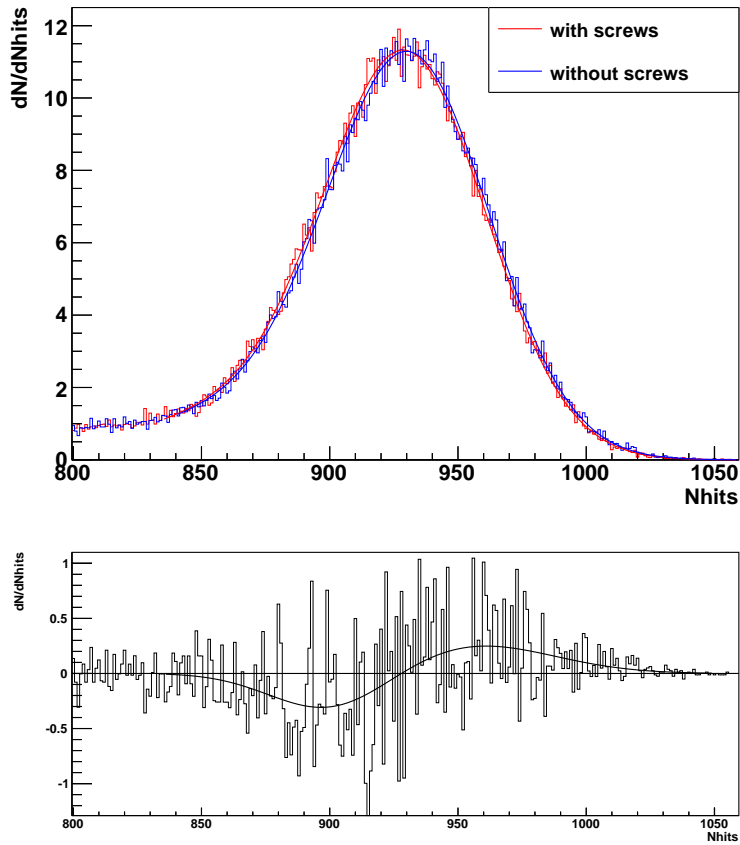


Figure 6.10: The upper figure shows the simulated ^{46}Sc inside the container with (red) and without screws and cross dowels (blue). In the lower figure the difference of the two spectra is shown for better comparison (the spectrum with screws/cross dowels is subtracted from the one without).

6.4 Quenching

The amount of scintillation photons produced by primary particles in liquid scintillator depends on their type and energy. Particles with a high stopping power create less scintillation light than those with less stopping power if they have the same initial energy. The effect of losing scintillation light due to a higher stopping power is called ionisation quenching. The ionisation quenching effect for photons is caused by the secondary electrons because their stopping power depends on the initial energy of the photon. The effect is much weaker than for ions but in a simulation it can be investigated. Since SNO+ will search for the double beta decay of ^{130}Te which is detected by two electrons, it is important to know the quenching parameters of the calibration sources.

The visible energy deposition of particles in liquid scintillator can be calculated by Birks' law [Bir51]:

$$dE_{vis.} = dE \cdot \frac{1}{1 + kB \cdot \frac{dE}{dx}} \quad (6.3)$$

where $dE_{(vis.)}$ is the (visible) energy deposition, $\frac{dE}{dx}$ is the stopping power and kB is the Birks constant. Because Birks' law is an empirical formula, kB has to be determined experimentally for every liquid scintillator.

Birks' law is implemented in RAT and quenching studies were done for ^{48}Sc and ^{46}Sc . The difference in the Nhits spectrum of the normal three or two gammas with about 1 MeV each was compared to that of one hypothetical gamma that carries the sum energy. Since one gamma with the sum energy has a lower stopping power, the light yield is expected to be higher.

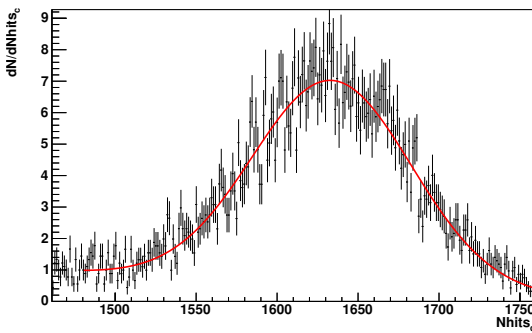


Figure 6.11: Fitted peak position of the 3 gammas of Sc48 with a sum energy of 3.333 MeV.

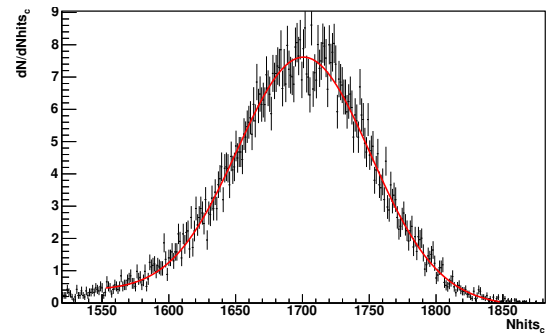


Figure 6.12: Fitted peak position of a single 3.333 MeV gamma.

To compare the Nhits spectra from one and three gammas in the case of ^{48}Sc , the two simulations were done with containers in LAB and with 20,000 events each. The fits for the peak positions are shown in Figure 6.11 and 6.12. The resulting peak positions and FWHMs with statistical errors are shown in Table 6.4.

Table 6.4: Fit results of Sc48 compared to a hypothetical 3.333 MeV gamma.

	Peak position	FWHM	$\frac{\sigma}{\sqrt{\text{Peakposition}}}$
Sc48	1630.7 (7)	124.4 (17)	1.31 (2)
3.3331 MeV	1700.7 (5)	119.1 (10)	1.23 (1)

The peak position of the normal ^{48}Sc is 4.1 % lower than that of the single gamma case. The FWHM and the resolution relative to the peak position are also different by 4.3 % and 6.3 % respectively. The two simulations show that the calibration with ^{48}Sc cannot be treated as a source with one single 3.333 MeV gamma because the gammas with lower energy are more affected by quenching.

For the study of the quenching of ^{46}Sc the Nhits spectrum was compared to that of one gamma with an energy of 2.010 MeV. Four different scenarios were investigated:

- ^{46}Sc as a point source in LAB
- ^{46}Sc inside the contained source in LAB
- ^{46}Sc as a point source in 0.3 % tellurium loaded LAB
- ^{46}Sc inside the contained source in 0.3 % tellurium loaded LAB

A total of 8 simulations was done with RAT version 4.4.0 and 100,000 events each. The fit functions of each case are compared in Figures 6.13 to 6.16 and the fit results are summarized in Table 6.5.

As expected the quenching of ^{46}Sc is less than for ^{48}Sc because of the higher stopping

Table 6.5: Peak positions and FWHMs of the Nhits spectra of ^{46}Sc as point and contained source in LAB and 0.3 % tellurium loaded LAB for quenching study.

		peak position			FWHM	
		Sc46	2 MeV γ	diff. in %	Sc46	2 MeV γ
LAB	cont.	928.6	957.7	3.04	77.8	77.9
	point	946.4	969.3	2.36	70.4	72.0
tellurium	cont.	342.8	353.9	3.14	47.5	47.2
	point	350.1	358.7	2.40	43.9	44.6

power of the 2.010 MeV gamma compared to that of the 3.333 MeV gamma. The contained source is more affected by quenching because the initial gamma can lose energy in the container which increases the stopping power in the LAB. Even though the absolute peak position is almost a factor 3 lower in the tellurium case, the percentage of lost Nhits due to quenching is comparable.

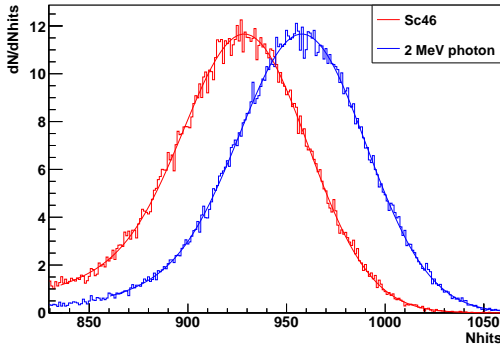


Figure 6.13: Fitted peak positions of the 2 gammas of ^{46}Sc compared to that of one hypothetical 2.010 MeV gamma in a contained source in LAB.

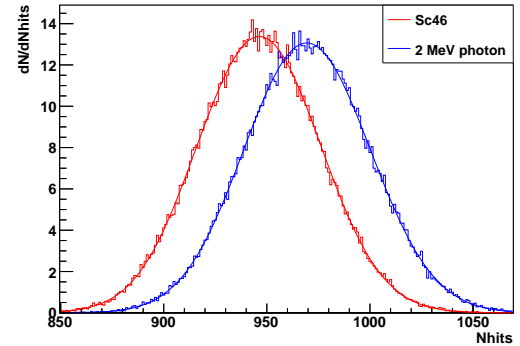


Figure 6.14: Fitted peak positions of the 2 gammas of ^{46}Sc compared to that of one hypothetical 2.010 MeV gamma as a point source in LAB.

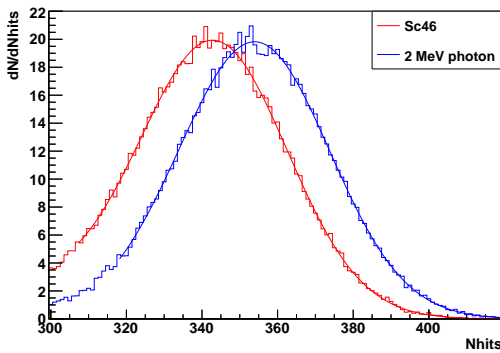


Figure 6.15: Fitted peak positions of the 2 gammas of ^{46}Sc compared to that of one hypothetical 2.010 MeV gamma in a contained source in 0.3% tellurium loaded LAB.

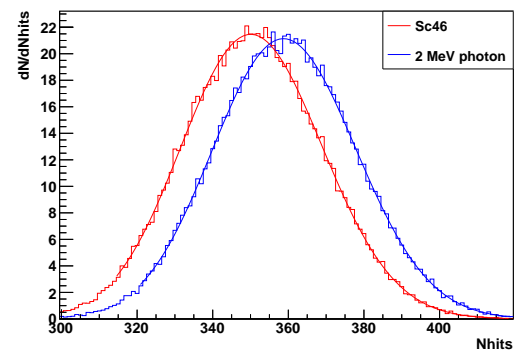


Figure 6.16: Fitted peak positions of the 2 gammas of ^{46}Sc compared to that of one hypothetical 2.010 MeV gamma as a point source in 0.3% tellurium loaded LAB.

6.5 Birks constant and light yield

Two parameters that are essential for the understanding of the detector response of SNO+ are the Birks constant and the light yield of the scintillator. The light yield is a constant that defines how many scintillation photons are created for each MeV initial energy. Both constants are determined experimentally. In LAB the measured values are (0.0798 ± 0.0039) mm/MeV [Tse11] for the Birks constant and (10800 ± 574) Photons/MeV [Gru14] for the light yield. Because the two parameters have different effects on the creation of scintillation light, the possibility of extracting these parameters directly from the shape of the Nhits spectrum was investigated.

The ^{48}Sc calibration source was simulated in LAB varying the parameters of the Birks constant and light yield. The standard scandium geometry and the sc48source generator were used (cf. Chapter 5). Twice the errors from the experimental values were chosen as a reasonable range for the variation. The range was divided into 9 parts and all pairs of values were simulated together which gives a total of 81 simulations. The first simulations were done with RAT version 4.2.1 and 20,000 events each. The used parameters are shown in Table 6.6.

Table 6.6: Birks constant and light yield values for the simulations.

BC/(mm/MeV)	0.0720	0.0740	0.0759	0.0779	0.0798	0.0818	0.0837	0.0857	0.0876
LY/MeV $^{-1}$	9652	9939	10226	10513	10800	11087	11374	11661	11948

If the desired activity of 5000 Bq for ^{48}Sc is reached in Dresden, the activities after 6 days of travel time to the detector are estimated to be 509 Bq for ^{48}Sc , 377 Bq for ^{47}Sc and 54 Bq for ^{46}Sc . These activities were chosen for the simulations.

The peak position for ^{48}Sc with standard parameters is around 1640 Nhits with 9080 PMTs online in the used RAT version. It is possible that two or more photons hit one PMT but only one signal is triggered. Therefore the number of photons hitting the PMTs is always higher than the amount of Nhits. To be able to test the linearity of the peak positions over the light yield change, this has to be taken into account. The Nhits were adjusted by the following formula:

$$\text{Nhits}_c = N_{\text{online}} \cdot \left(-\ln \left(1 - \frac{\text{Nhits}}{N_{\text{online}}} \right) \right) \quad (6.4)$$

where the Nhits_c are the corrected Nhits and N_{online} are the 9080 online PMTs. This formula is used under the assumption of a Poisson distribution for the probability of photons hitting the PMT. The assumption is justified with the low probability for a hit

on a random PMT.

To leave the same amount of events inside each bin the change is actually done by increasing the bin size. With a bigger bin size, the integral over the histogram is increased. Therefore the number of entries in each bin is reduced by the same factor that the bin was increased. The bin size of the graph in Figure 6.17 is 2 Nhits_c .

All the data and the fits are shown in Figure 6.17 in the range of the peaks. The fit functions are 2 Gaussians with 6 free parameters for each peak. The groups of peaks correspond to identical light yields and within them the Birks constant varies. This shows that the error range of the LY has a greater effect on the peak position than that of the Birks constant.

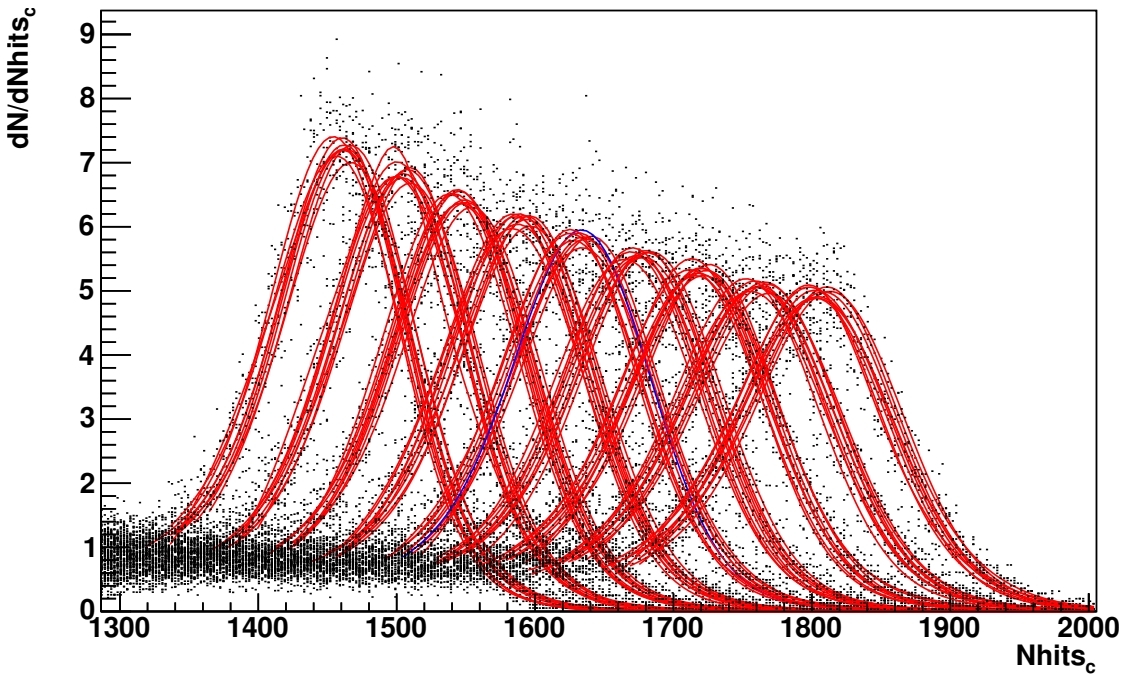


Figure 6.17: Data and fits of the peak of ^{48}Sc with the corrected Nhits . The blue function in the middle is the fit with standard values for the Birks constant and light yield.

In Figure 6.18 and 6.19 the peak positions over the Birks constant and the peak positions over the light yield are shown respectively. Both graphs show the same data points but in different order. The lines are linear fits of the points with the same light yields (Figure 6.18) or the same Birks constants (Figure 6.19). The statistical errors of the peak positions are also shown but since they are smaller than 1 bin which is smaller than 0.1 %, they are hardly visible.

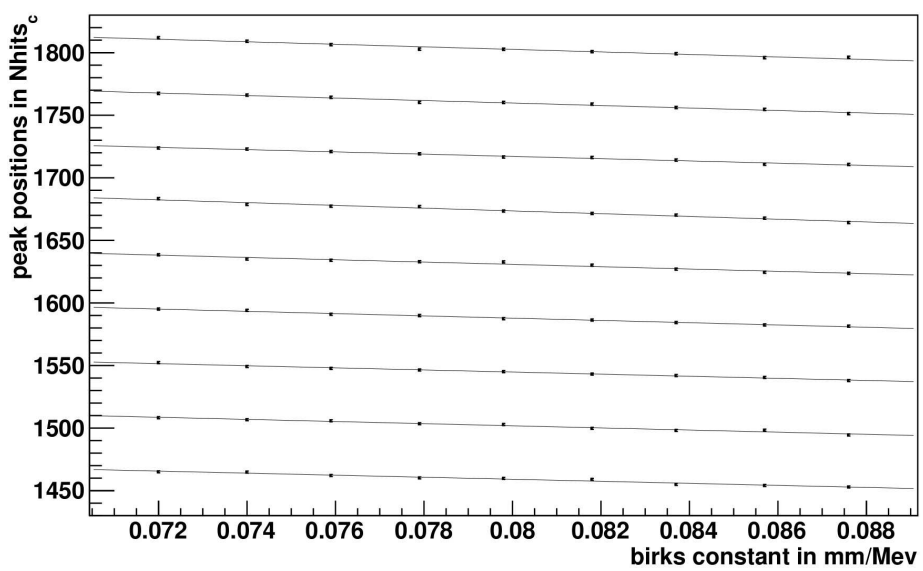


Figure 6.18: Birks constant dependent peak positions with light yield increasing from bottom to top.

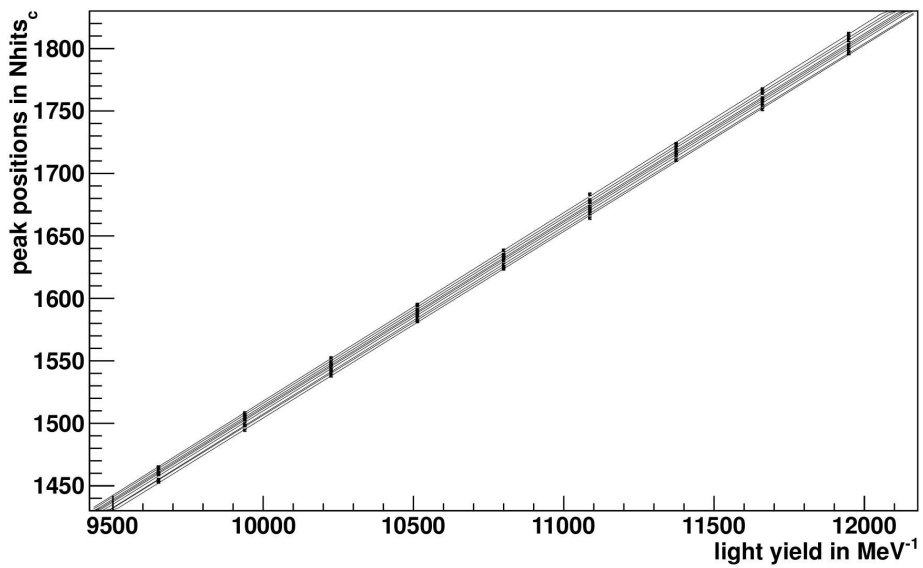


Figure 6.19: Light yield dependent peak positions with the Birks constant increasing from top to bottom.

The average of the 9 slopes in Figure 6.18 is $-929 \text{ Nhits}_c \frac{\text{MeV}}{\text{mm}}$ but the slope increases from bottom to top with increasing light yield. This can be explained by Birks' law because the visible energy deposition is reduced relatively with respect to the total light output. This means that the absolute change in Nhits due to quenching is larger for higher light yields.

The average of the slope in Figure 6.19 is $(0.1497 \pm 0.0004) \text{ Nhits}_c \cdot \text{MeV}$. The offsets are between 8 and 19 Nhits_c with an error of 4.2 Nhits_c. The Birks constants are increasing from top to bottom.

The comparison of the two graphs shows again that the range of the light yield has a bigger impact on the peak position than the range of the Birks constant.

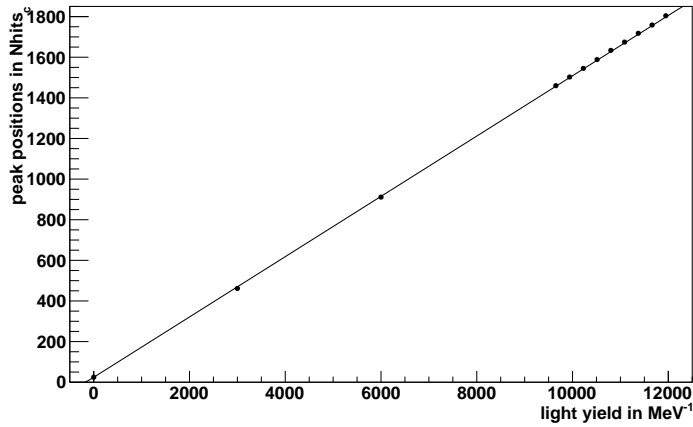


Figure 6.20: Linear fit of peak positions over light yield from 0 MeV^{-1} to 11948 MeV^{-1} with a Birks constant of 0.0798 mm / MeV .

With another set of simulations it was tested if the assumption of a linear dependency of the peak position on the light yield parameter can be extended to a light yield of 0 MeV^{-1} . Three extra simulations were done with the standard Birks constant and a light yield of 0 MeV^{-1} , 3000 MeV^{-1} and 6000 MeV^{-1} . The linear fit for that case is shown in Figure 6.20.

The fit parameters for the linear functions in the ranges $(0 - 11948) \text{ MeV}^{-1}$ and $(9652 -$

Table 6.7: Parameters from linear fits of peak positions over light yield in the ranges $(0 - 11948) / \text{MeV}^{-1}$ and $(9652 - 11948) / \text{MeV}^{-1}$.

Fit range / MeV ⁻¹	Slope / (Nhits _c · MeV)	Offset / Nhits _c
0 - 11948	0.1484 (0)	24.3 (1)
9652 - 11948	0.1494 (4)	17.7 (42)

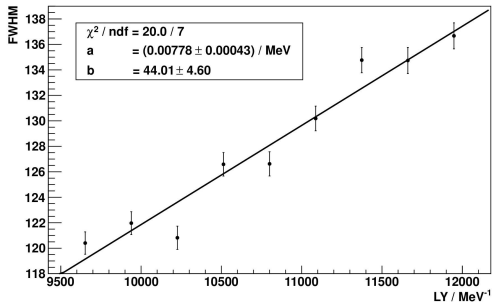


Figure 6.21: Linear fit of FWHM over LY with a Birks constant of 0.0798 mm/MeV and 100,000 events per point.

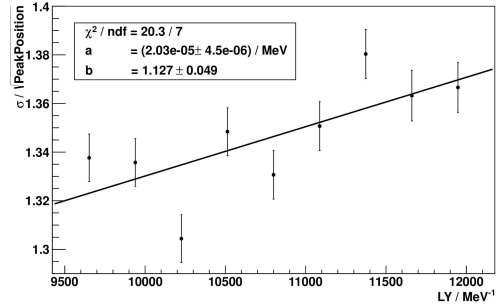


Figure 6.22: Linear fit of resolution over LY with a Birks constant of 0.0798 mm/MeV and 100,000 events per point.

$11948) \text{ MeV}^{-1}$ are compared in Table 6.7. Because the slope changes only by 0.7% a linear dependency of the peak position on the light yield is a good approximation. The small positive offset can be explained by hits that were triggered by direct Čerenkov light that passes through the scintillator even without any simulated light yield. This was confirmed by a simulation without Čerenkov light where no Nhits were obtained at 0 light yield value.

For the evaluation of the FWHM and the resolution a new simulation with 9 different light yields and 100,000 events each was done to increase the statistics. In Figure 6.21 and 6.22 the dependency of the FWHM and relative resolution on the light yield is shown. Both are rising with higher light yields but due to the large errors no direct prediction on the light yield is possible.

When the scandium calibration source is deployed in the detector only the Nhits spectrum will be available to extract information. From the peak position it is possible to extract the value for the light yield when the Birks constant is fixed or vice versa.

The aim of further analysis was to find out if it was possible to distinguish a set of Birks constant and light yield parameters from the shape of the Nhits spectrum. A possible hint could result from the relative distance of the scandium peaks. Such a parameter would allow an additional measurement from the calibration alone which would be independent from optical measurements of Birks constant and light yield. A new set of 81 simulations with 100,000 events each was done.

Because the peak position in Nhits is shifted towards higher values for larger light yields and lower values for larger Birks constants, it was possible to obtain the same peak position with two different sets of Birks constant and light yield. To get an idea of the

effect in the change of the shapes of the spectra, the largest and lowest possible Birks constants were chosen. Largest and lowest light yield values exceed the range for the Birks constant that would be required to match the same peak position. The parameters used for the shape analysis are shown in Table 6.8 together with the corresponding fitted peak positions for all three scandium isotopes. Using the slopes from the largest and smallest Birks constants in Figure 6.19, the corresponding peak positions were calculated for comparison.

Table 6.8: Birks constant and light yield values with calculated and fitted peak positions for the three scandium isotopes. The peaks are calculated from the linear functions in Figure 6.19 (peak_c).

	BC/(mm/MeV)	LY/MeV $^{-1}$	peak_c ^{48}Sc	^{48}Sc peak	^{46}Sc peak	^{47}Sc peak
min BC	0.0720	10752	1631.2	1631.7 (4)	979.9 (9)	68.31 (9)
max BC	0.0876	10848	1630.8	1630.8 (4)	977.5 (9)	67.21 (9)

The relative change of the peak positions is 0.06 % for ^{48}Sc , 0.2 % for ^{46}Sc and 1.6 % for ^{47}Sc . The fits of the peaks are shown in Figure 6.23 for ^{48}Sc , Figure 6.24 for ^{46}Sc and Figure 6.25 for ^{47}Sc . ^{48}Sc and ^{46}Sc were both fitted with a Gaussian plus a linear background and ^{47}Sc was fitted with one Gaussian².

The spectrum of ^{48}Sc shows a slight difference for what concerns the height of the two fitted peaks. However, this is considered not relevant because it is still within the statistical error range. The peak position shift of ^{47}Sc might be large enough to give a hint to distinguish between the Birks constant and the light yield pairs. However, due to its proximity to the trigger threshold there is the risk that the peak will either not be measured at all or it could be distorted during data taking. The small difference in the relative peak positions of ^{46}Sc and ^{48}Sc is also not significant.

The high energy part of the two spectra with the peaks of ^{46}Sc and ^{48}Sc is compared in Figure 6.26. The idea was to check not only for differences in the peak positions but also for possible changes of the shapes in the region between the peaks. This area is populated by events originating in ^{48}Sc decays that lost energy in the source container. It is possible that differences in the shape due to quenching are visible there. Unfortunately the spectra are very similar and it is not possible to extract any hint about a preferred pair of Birks constant and light yield.

With only small changes in the Nhits spectra that differ by twice the measured errors of the Birks constant, it is unlikely that a significant distinction between different values

²The analysis for the double Gaussian fitting function of the ^{48}Sc peak in Section 6.1 was done after the simulation for Birks constant and light yield. At this time the standard fit was still a Gaussian with linear background.

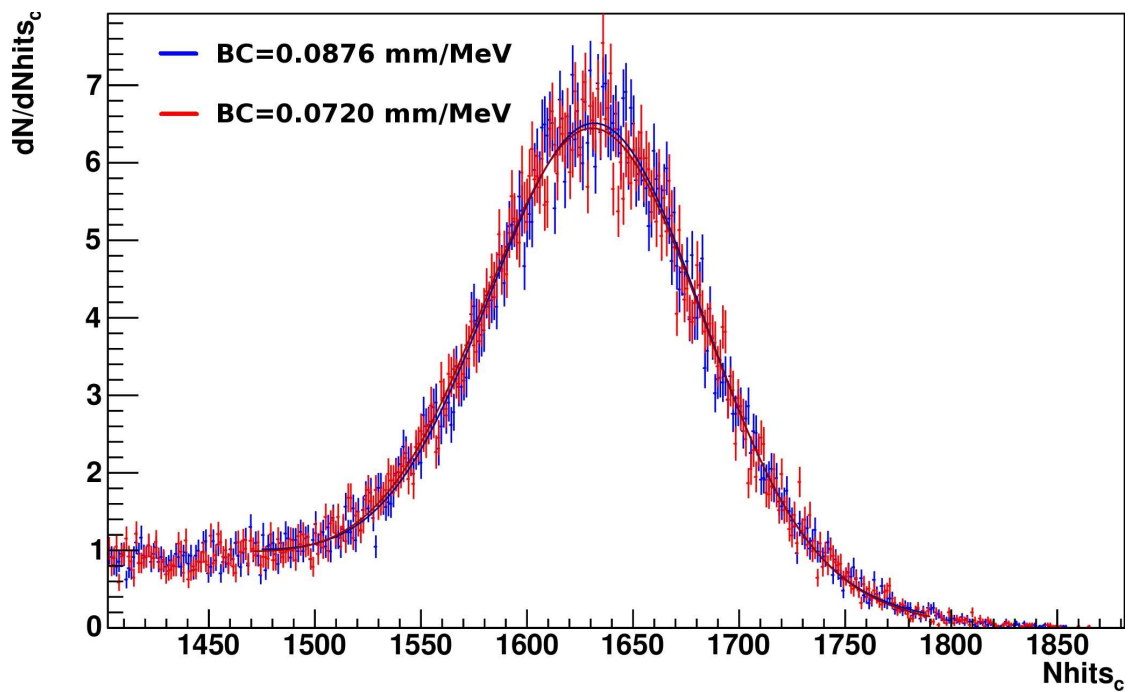


Figure 6.23: ^{48}Sc peak area of the simulations with minimum (red) and maximum (blue) Birks constant and fit function.

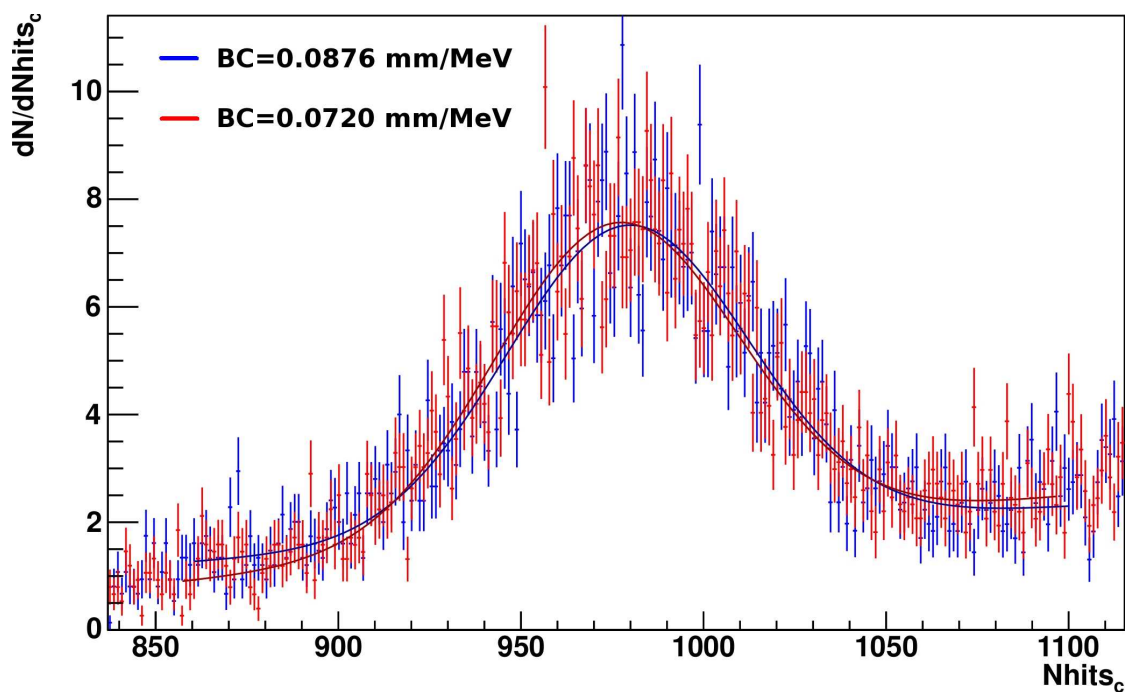


Figure 6.24: ^{46}Sc peak area of the simulations with minimum (red) and maximum (blue) Birks constant and fit function.

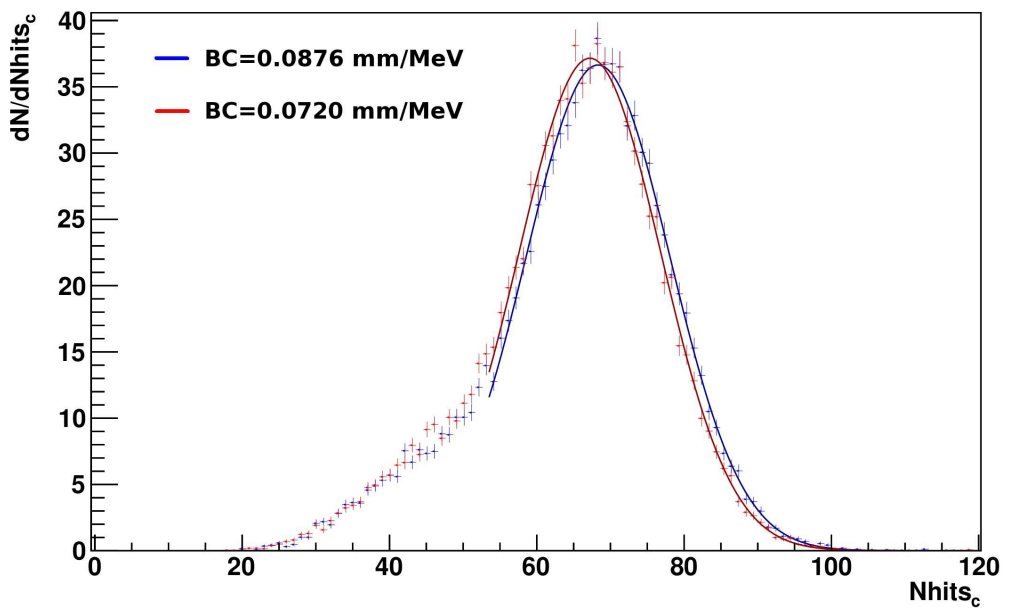


Figure 6.25: ^{47}Sc peak area of the simulations with minimum (red) and maximum (blue) Birks constant and fit function.

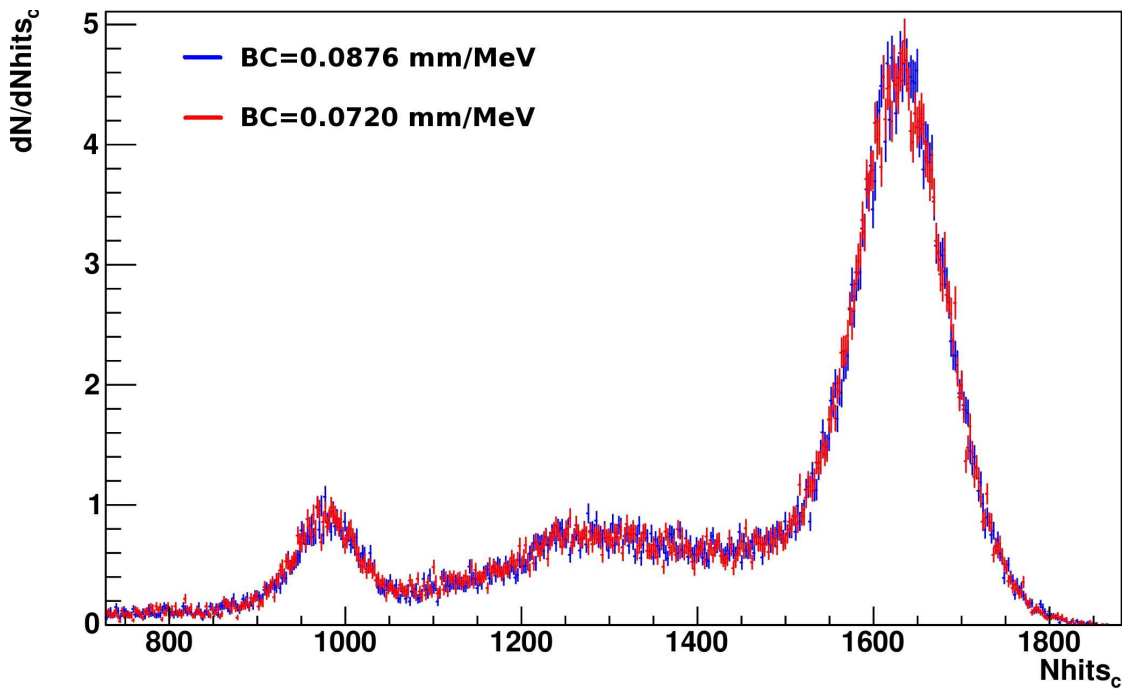


Figure 6.26: Nhits spectra of the simulations with minimum (red) and maximum (blue) Birks constant.

of Birks constant and light yield can be made with the data from the scandium calibration source. However, the peak position of ^{48}Sc determines the light yield if a Birks constant is fixed and the Birks constant is determined for a fixed light yield. Using this correlation, independent optical measurements of Birks constant and light yield can be checked for agreement.

6.6 Source holder tests

The calibration system in the SNO+ detector requires the sources to have a weight between 3 and 4 kg to apply enough tension to the ropes. To reach that weight, the source is connected via a holder made of acrylic to a stainless steel weight cylinder of about 3 kg that is possibly encapsulated in acrylic to reduce impurities. A sketch of the source geometry is shown in Figure 6.27.

The purpose of the holder is to increase the distance to the steel cylinder which will reduce the absorption of scintillation photons and energy loss due to primary gamma scattering. Additionally, the total length of all source parts (containers, holder, weight cylinder and connector to umbilical) has been fixed to about 50 cm to match the source box height. For these reasons the dependence of the ^{48}Sc peak position in the Nhits spectrum on the holder length has been investigated.

Three simulations with all scandium isotopes were done in LAB using a modified version of RAT 4.5 and 30,000 events each. The modifications were done to be able to extract the energy deposited in the different parts of the source encapsulations from the MC branch. Lengths of 10 cm, 20 cm and the standard value of 30 cm were simulated for an acrylic and a teflon (PTFE) holder. The standard stainless steel weight cylinder had a height of 13.5 cm and a radius of 3.2 cm. An additional simulation was done for the case of a steel holder which would be heavy enough to replace half of the weight cylinder.

In RAT 4.5 material surface reflections of scintillation photons were implemented. All

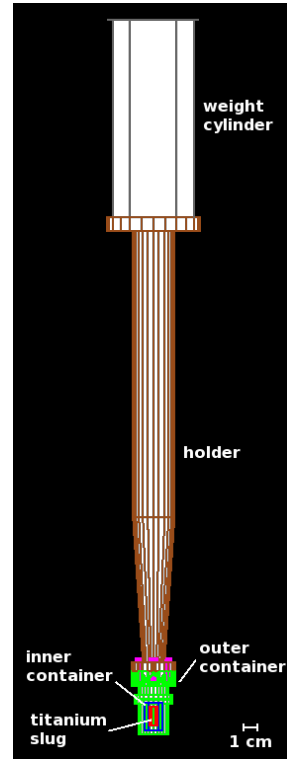


Figure 6.27: Source geometry with holder and weight cylinder.

Table 6.9: Energy deposition, peak positions and FWHMs for different holder lengths.

Holder material	Holder length	Energy deposition Weight cyl./%	Holder/%	Peak position	FWHM
PTFE	10 cm	0.47	0.34	1491.1 (5)	109.0 (11)
	20 cm	0.15	0.36	1493.3 (4)	108.9 (11)
	30 cm	0.06	0.36	1494.5 (4)	105.8 (11)
Acrylic	10 cm	0.54	0.25	1499.6 (4)	102.3 (10)
	20 cm	0.20	0.22	1506.8 (4)	100.0 (10)
	30 cm	0.07	0.24	1511.1 (4)	96.7 (10)
Steel	30 cm	0.03	0.99	1495.6 (4)	107.2 (11)

simulations for the different holder lengths were done with a 40 % reflectivity on the stainless steel surfaces which reduces the shadowing on the ^{48}Sc peak position from 2.00 % to 1.89 %.

In Table 6.9 the energy deposition inside the weight cylinder and holder together with the resulting peak positions and FWHMs is shown. In Table 6.10 the fraction of events with full energy deposition in the scintillator is shown.

The comparison of the energy deposition in a teflon and acrylic holder favors the acrylic. The fraction of full energy events is higher for the acrylic holder. It also shows a higher peak position and a better resolution. In both cases the 30 cm holder length is obviously the best option while for shorter lengths peak position and resolution decreases. Decreasing the length by 20 cm increases the energy deposition in the weight cylinder by a factor of 8. The peak position (FWHM) changes by 0.23 % (2.9 %) for the teflon holder and 0.76 % (5.5 %) for the acrylic holder.

A steel holder would have the least amount of energy deposition in the weight cylinder because the holder acts as a shield and the cylinder has only half the volume. In this

Table 6.10: Fraction of Nhits inside the two full energy peaks of ^{48}Sc .

Holder material	Holder length	Events with full energy deposition/%	
		3.3 MeV peak	3.5 MeV peak
PTFE	10 cm	49.1	4.2
	20 cm	50.3	4.1
	30 cm	50.8	4.3
Acrylic	10 cm	49.3	4.1
	20 cm	50.6	4.1
	30 cm	51.7	4.4
Steel	30 cm	48.4	4.0

case 1% of the energy is already lost in the holder which leads to the lowest fraction of events inside the full energy peak. The peak position and FWHM are comparable to the teflon holder simulations but worse than those with acrylic.

It is therefore recommended to use an acrylic holder with the maximum possible length.

6.7 Position dependence

When the scandium calibration source is deployed, it will be placed in different positions in the detector. A calibration at varying positions will improve the understanding of the position dependent detector response. With simulations in RAT the effects of different positions can be investigated before the deployment.

The full scandium source was simulated along X, Y and Z axis with the distance parameters shown in Table 6.11. At each position 100 k events were simulated for ^{48}Sc and ^{46}Sc in LAB and 0.3 % tellurium loaded LAB. The simulation data was analyzed for the Nhits spectrum as well as the energy and position reconstruction. A standard fitter that was developed by the SNO+ collaboration was used in this case. The Nhits and energy

Table 6.11: Distances from the center of the detector along X, Y and Z axis for the position simulations. The center position at (0.0, 0.0, 0.0) was simulated as well.

X Position / m				
(± 1.0 , 0.0, 0.0)	(± 2.0 , 0.0, 0.0)	(± 3.0 , 0.0, 0.0)	(± 3.5 , 0.0, 0.0)	(± 4.0 , 0.0, 0.0)
(± 4.5 , 0.0, 0.0)	(± 5.0 , 0.0, 0.0)	(± 5.5 , 0.0, 0.0)	(± 5.7 , 0.0, 0.0)	(± 5.9 , 0.0, 0.0)
Y Position / m				
(0.0, ± 1.0 , 0.0)	(0.0, ± 2.0 , 0.0)	(0.0, ± 3.0 , 0.0)	(0.0, ± 3.5 , 0.0)	(0.0, ± 4.0 , 0.0)
(0.0, ± 4.5 , 0.0)	(0.0, ± 5.0 , 0.0)	(0.0, ± 5.5 , 0.0)	(0.0, ± 5.7 , 0.0)	(0.0, ± 5.9 , 0.0)
Z Position / m				
(0.0, 0.0, ± 1.0)	(0.0, 0.0, ± 2.0)	(0.0, 0.0, ± 3.0)	(0.0, 0.0, ± 3.5)	(0.0, 0.0, ± 4.0)
(0.0, 0.0, ± 4.5)	(0.0, 0.0, ± 5.0)	(0.0, 0.0, ± 5.5)	(0.0, 0.0, ± 5.7)	(0.0, 0.0, ± 5.9)

reconstruction spectra were fitted with a double Gaussian in case of ^{48}Sc and Gaussian plus linear function (cf. Section 6.1) in case of ^{46}Sc to determine the peak values. The absolute peak values³ at the center of the detector are summarized in Table 6.12. In Figure 6.28 the peak values of the Nhits spectra are shown relative to the central peak values.

³This refers to the peak position that is fitted from the respective spectrum. To prevent confusion with the position of the source in the detector, it is called peak value in this Section.

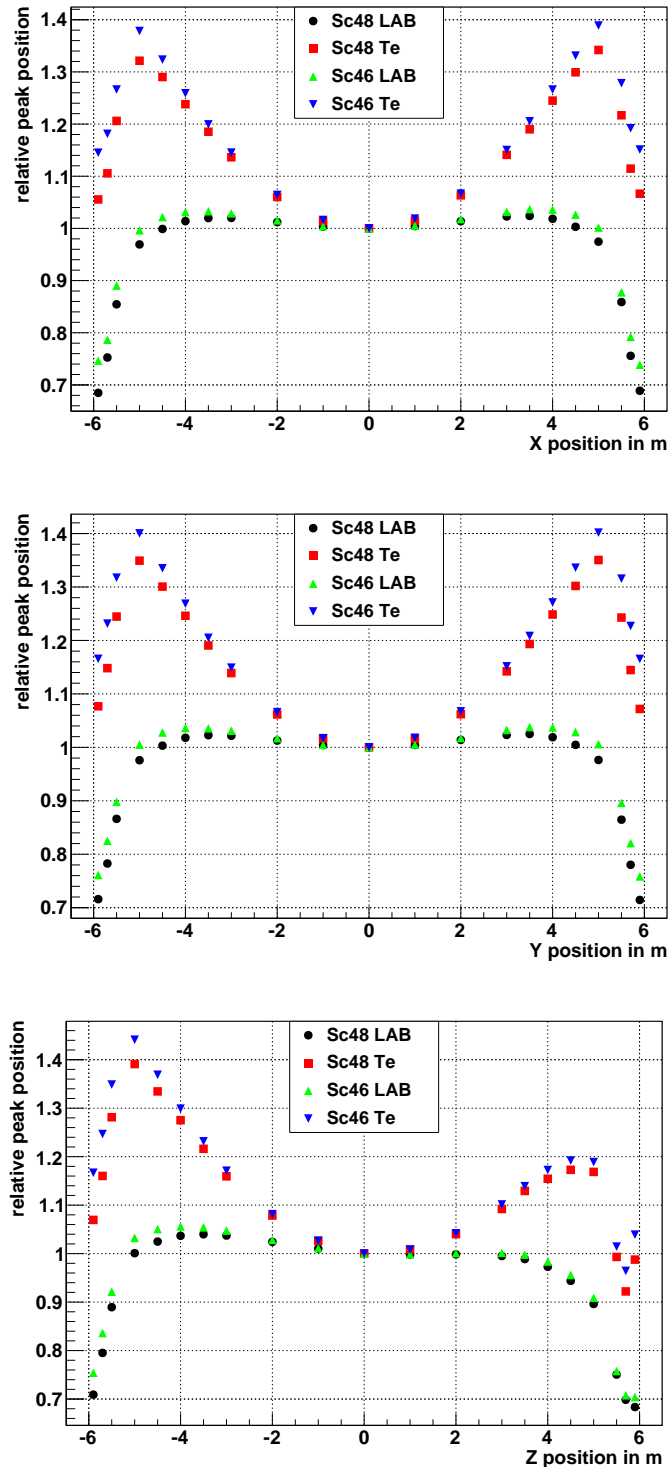


Figure 6.28: Peak values relative to the one obtained for a source at (0,0,0) in the Nhits spectra. Results are obtained for different source positions in the detector. Changes along X (top), Y (middle) and Z axis (bottom) for ^{48}Sc and ^{46}Sc in LAB and 0.3 % tellurium loaded LAB are shown.

Table 6.12: Absolute peak value in the Nhits and energy reconstruction spectra for central source position in the detector.

Peak value	$^{48}\text{Sc LAB}$	$^{48}\text{Sc Te}$	$^{46}\text{Sc LAB}$	$^{46}\text{Sc Te}$
Nhits	1488.3	558.1	925.0	337.5
Energy reconstruction	3.136	3.064	1.882	1.851

The peak value increases with larger distance from the detector's center. The PMTs with short distances to the event have a larger probability to trigger because of less absorption in the LAB. This overcompensates the lost Nhits on the PMTs with larger distance to the event. However, when the source position is close to the detector edge, there is a high probability that the primary gammas leave the detector without depositing the full energy. As a consequence the peak value decreases.

Position shifts in X and Y directions are symmetric with respect to the detector center. However, the Z direction shows an asymmetry. Simulations of the source at positive Z positions yield smaller peak values because of a lack of PMTs at the neck of the AV. Generally the Nhits spectra show a stronger dependence on the position in the 0.3 % tellurium loaded LAB case because of the stronger absorption of scintillation light. However, close to the edge of the detector ($r > 5\text{ m}$), the simulations in LAB show deviations of up to 30 % from the central peak value. The relative peak values of ^{46}Sc are larger than those of ^{48}Sc but the difference is below 10 % for the 0.3 % tellurium loaded LAB case and below 5 % for pure LAB.

In Figure 6.29 the peak values of the reconstructed energy spectra are shown relative to the central peak values. The energy reconstruction algorithm takes into account that the peak values shift at different positions in the detector. As a result, the energy reconstruction is less dependent on the source position in the detector than the Nhits spectra. However, deviations of the peak values up to about 5 % were obtained for positions close to the edge when the source is moved along the X and Y axis. The fluctuation of the Z position showed a large asymmetry. Energies from positions close to the neck are underestimated by up to 25 % and those at the bottom are overestimated by up to 10 %. For the analysis of the position reconstruction the spectra were fitted with a single Gaussian. The deviations of the peak values from the central detector position are shown in Table 6.13. On the positive distance scale, the deviation of the position reconstruction is obtained by subtracting the distance of simulation from the fitted peak values. For symmetry reasons the results on the negative scale were inverted. The results are shown in Figure 6.30.

With increasing distance from the center of the detector, the position reconstruction in

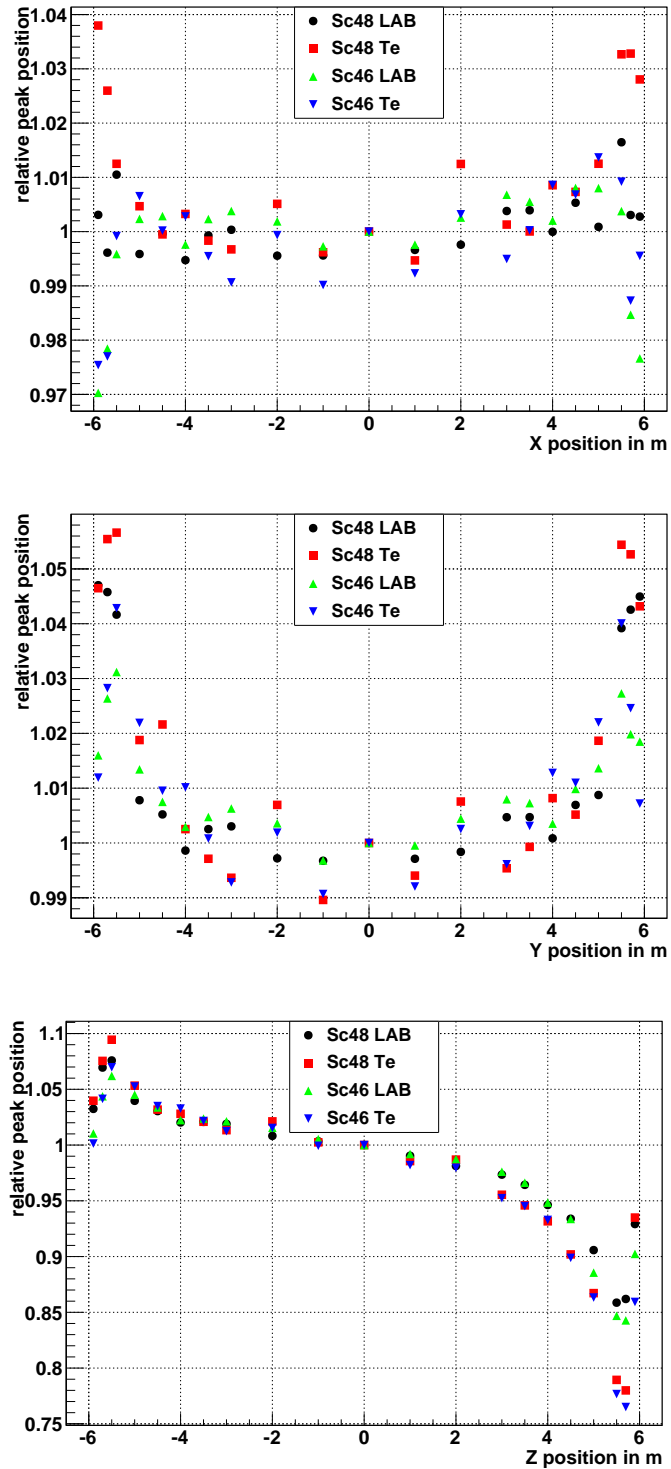


Figure 6.29: Peak values relative to the one obtained for a source at (0,0,0) in the reconstructed energy spectra. Results are obtained for different source positions in the detector. Changes along X (top), Y (middle) and Z axis (bottom) for ^{48}Sc and ^{46}Sc in LAB and 0.3 % tellurium loaded LAB are shown.

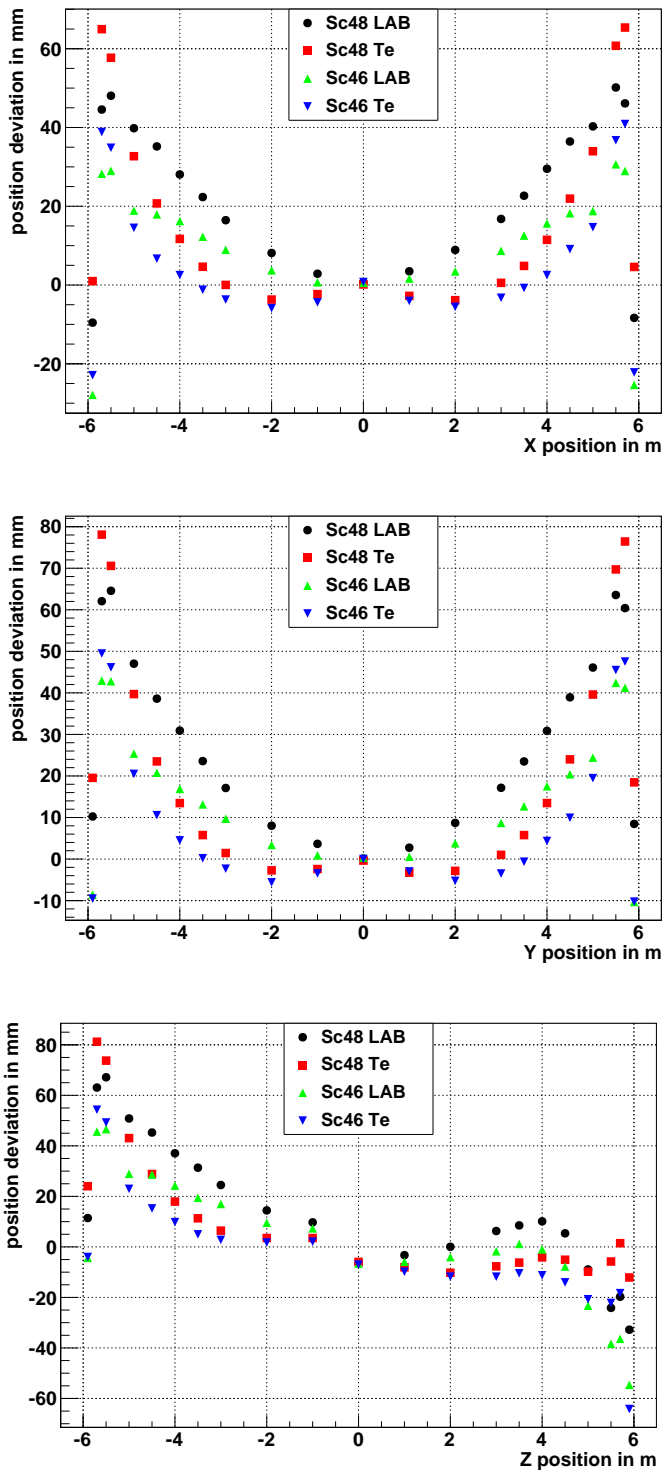


Figure 6.30: Deviations of reconstructed peak values from simulated source positions in the detector. Changes along X (top), Y (middle) and Z axis (bottom) for ^{48}Sc and ^{46}Sc in LAB and 0.3 % tellurium loaded LAB are shown.

Table 6.13: Deviations of reconstructed peak values from simulated source positions in the center of the detector at (0,0,0).

	^{48}Sc LAB	^{48}Sc Te	^{46}Sc LAB	^{46}Sc Te
X/mm	0.707	0.140	0.561	0.755
Y/mm	0.142	-0.363	0.337	0.010
Z/mm	-6.706	-5.933	-6.620	-7.022

LAB overestimates the position with respect to the center. Close to the edge the reconstruction is off by up to 8 cm. In 0.3 % tellurium loaded LAB the deviation is generally smaller by roughly 1.5 cm but shows the same behavior. The simulations along the X and Y axis are similar and symmetric. Negative Z distances have deviations similar to the simulations along X and Y. Peak values from simulations at the neck of the detector are underestimated by up to 6 cm.

7 Conclusion and Outlook

The scandium calibration source for the SNO+ experiment was developed for about three years. In this thesis the source container design was completed. The scandium source is produced via neutron irradiation on natural titanium. A titanium cylinder was successfully irradiated using the DT-generator of TU Dresden. It was demonstrated that an activity of 5 kBq of ^{48}Sc can be achieved. After a shipping time of 6 days this will result in an activity of 500 Bq available for the calibration at the SNO+ detector.

The final shape of the source containers was designed and prototypes were tested for tightness. All problems concerning the safety and tightness of the source containers are solved and they are now ready for production. Two annealing cycles during the machining process ensure good material quality and prevent cracks or crazings in the containers. Compatibility of acrylic with cleaning agents was tested and a detailed cleaning procedure for all source parts is available.

^{48}Sc will be used to calibrate the SNO+ detector at the sum energy of 3.3 MeV and possibly study the ionisation quenching. The possibility for the usage of ^{46}Sc as a second calibration source at 2.0 MeV was examined. After the calibration with ^{48}Sc it is possible to calibrate with ^{46}Sc one week later when most of the ^{48}Sc has decayed. This will reduce the contamination in the ^{46}Sc energy region due to the gammas of ^{48}Sc and give a much clearer peak. Quenching studies and calibration at two energies can be done without introducing additional contamination risk.

Simulation studies for the usage of the source in the detector were presented. A linear dependence of the peak position on the light yield was found. The Birks constant and the light yield were varied to test if each of them leaves a unique signature on the Nhits spectrum that makes it possible to separate them. The goal was to derive parameters from hints in the spectrum that would favor a distinct set of Birks constant and light yield that lead to the specific spectrum. No such parameters were found but the peak position of ^{48}Sc allows to cross check the optically measured values for Birks constant and light yield.

The holder of the source geometry was simulated with different materials and sizes and the effects on the peak position and FWHM were examined. Best results were found with an acrylic source holder as long as possible to increase the distance to the weight cylinder.

When the containers are produced, they will be tested for tightness, cleaned thoroughly and measured for radioactive background. The outer container and the activated source will be sent to SNO+ site separately to avoid cross contamination during the cleaning

procedure.

The scandium calibration source can be deployed in the SNO+ detector during the pure scintillator phase and the tellurium loaded phase. If deployed, the source will contribute to the energy calibration and to the understanding of the detector.

A Appendix

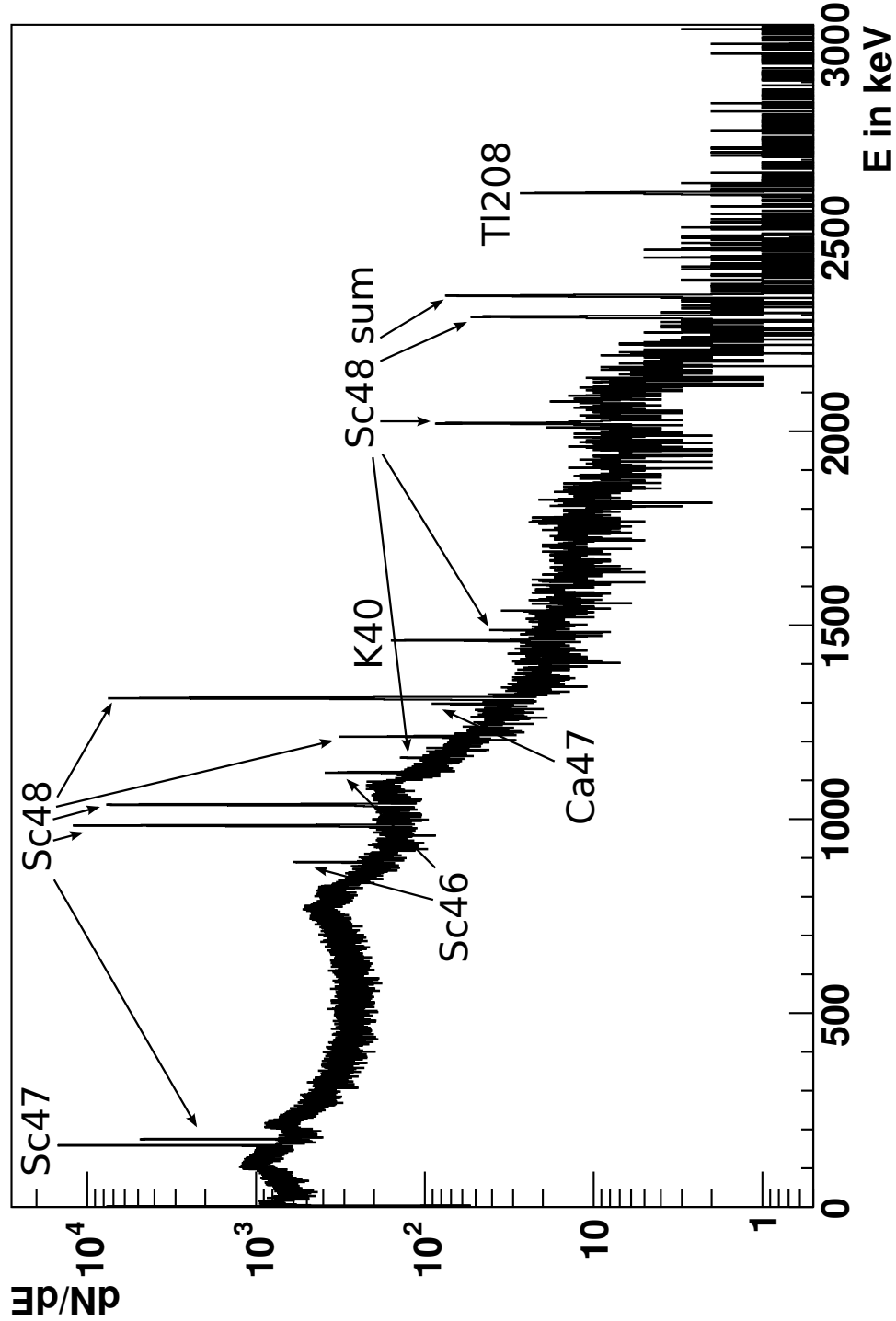


Figure A.1: Spectrum of the activated titanium sample measured on 14.04.14. The peaks of the main isotopes are indicated.

Figure A.2: Detailed cleaning procedure for the scandium calibration source parts.

Cleaning procedure for the Sc48 calibration source

March 3, 2014

1 Materials

- Ultrasonic bath (UB)
- Scale (mg accuracy)
- Beakers (at least 2 of 250 ml)
- Bottles for solutions (at least 3)
- Tweezers
- Thermometer (up to 60 degrees Celsius at least)
- Kimtech wipes
- Powder free gloves
- Lab goggles
- Lab coat
- Deionized water (DIW)
- MilliQ - ultrapure water (UPW)
- Pure ethanol (high purity)
- Alconox
- Citranox
- Nitric acid (high purity)
- Fume hood
- Plastic bags from Polypropylen (PP)

2 Cleaning procedure for beakers, bottles and tools

This procedure must be followed every time the beaker, bottles or tools need to be cleaned.

- Wear coat, goggles and gloves
- Prepare 1% Alconox cleaning solution (1 % = 10 g per 1 l DIW) using warm DIW.
Follow vendor instructions to prepare it.
- Soak, rinse and wipe with 1% Alconox solution.
- Rinse with DIW
- Soak, circulate, wipe with pure ethanol
- Rinse with DIW
- Wipe with kimtech wipes
- Place on the counter on paper towel. Let it completely dry
- If not used immediately, once dry store them in sealed plastic bags

3 Outer and inner container cleaning procedure

This procedure must be followed to clean the outer and inner container parts. The cleaning should take place under a fume hood.

- **1. Preparations**

- Wear coat, goggles and gloves
- Prepare a working place with absorbent paper and place cleaned bottles, beakers and tweezers there
- Prepare Alconox cleaning solution (1 % = 10 g per 1l DIW) in a big beaker, preferably using warm DIW
- Label a bottle and fill with the 1% Alconox solution

- **2. Ultrasonic cleaning with Alconox**

- Place the inner and outer container pieces (bottom and lid) in a cleaned beaker and fill the beaker with Alconox until the parts are fully covered
- Fill the UB with DIW at room temperature
- Place the beaker containing the container parts in the UB. If possible use a proper holder for the beaker.
- Run the UB for 10 minutes
- Once the time is over, switch off the UB and remove the container parts with the help of tweezers and rinse them carefully with DIW
- Place the container parts on the counter on absorbent paper
- Remove the used beaker and the used Alconox solution
- Clean the tweezers with 1% Alconox solution and rinse them with DIW. Then dry them with Kimtech.

- **3. Ultrasonic cleaning with DIW**

- Place the container parts with the cleaned tweezers into a cleaned beaker and fill with DIW until they are fully covered
- Place the clean beaker in the UB and run for 15 minutes
- Clean the tweezers and the used beaker
- Once the time is over, switch off the UB and place the beaker on the counter on clean absorbent paper
- Clean the tweezers with 1% Alconox solution and rinse them with DIW. Then dry them with Kimtech.

- **4. Wipe with Alconox**

- Prepare a Kimwipe soaked in Alconox
- Hold the container parts with tweezers and wipe the surface with Kimwipe soaked in Alconox
- Rinse the container parts with DIW and place them on a clean absorbent paper

- Clean the tweezers with 1% Alconox solution and rinse them with DIW. Then dry them with Kimtech.

- 5. Ultrasonic cleaning with DIW and prepare nitric acid solution**

- Place the container parts with the cleaned tweezers into a cleaned beaker and fill with DIW until they are fully covered
- Place the clean beaker in the UB and run for 15 minutes
- Clean the tweezers and the used beaker
- Change gloves
- Prepare the nitric acid solution (1 mol/l) with UPW in a cleaned beaker
- Label a bottle and fill with the nitric acid solution, place it in the fume hood
- Clean the used beaker
- Change gloves
- Once the UB time is over, remove the container parts with the help of cleaned tweezers and place them on clean absorbent paper
- Turn on the UB heat
- Clean the used beaker

- 6. Ultrasonic cleaning with 1 mol nitric acid solution**

- Place the container's parts in a cleaned beaker with the help of tweezers and fill with nitric acid until fully covered
- Check that the UB temperature is at 40 °C, place the beaker with the inner container's parts
- Run the UB at 40 °C for 5 minutes
- Clean the tweezers
- Take the container's parts out with the help of tweezers and rinse them with UPW
- Put the container's parts in a cleaned beaker and fill with new nitric acid until fully covered
- Remove the used beaker
- Check that the UB temperature is still at 40 °C
- Place the beaker in the UB and run for other 5 minutes
- Dispose the used nitric acid solution
- Clean the tweezers and the used beaker with UPW
- Change gloves
- Once the time is over switch off the UB and the heater
- Take the container's parts out with the help of tweezers and rinse them with UPW
- Put the container's parts in a cleaned beaker and fill with new nitric acid until fully covered

- Change gloves
- Remove the old beaker and replace the DIW in the UB with new DIW at room temperature
- Place new beaker in the UB and run for 60 minutes
- Clean the tweezers and the beaker. For the last cleaning step use UPW
- Once the UB time is over, remove the container parts with the help of cleaned tweezers, rinse them with UPW and place them on clean absorbent paper on the counter
- Clean the tweezers and the beaker. For the last cleaning step use UPW
- Change gloves

- **7. Ultrasonic cleaning with UPW**

- Place the container parts into a cleaned beaker with the help of tweezers and fill with UPW until fully covered
 - Place the beaker in the UB and run for 15 minutes
 - Clean the tweezers with UPW
 - Dilute and/or dispose the left nitric acid solution
 - Once the UB time is over, remove the container parts with the help of cleaned tweezers, rinse them with UPW and place them on clean absorbent paper on the counter
 - Let the parts dry. If available use an oven to dry
 - Cleaned all the used material and empty the UB

- **8. Packing of the container**

- Wear new gloves
 - Wipe PP bag on the inside with Kimwipe soaked in Ethanol
 - Let the bag dry
 - Put the cleaned container parts in the bag
 - Heat seal the opening but leave a small hole
 - Fill the bag with nitrogen, then remove it
 - Fill with nitrogen a second time and immediately seal the bag completely

4 Cleaning procedure for the titanium slug and screws

This procedure should be followed to clean all the metals parts (titanium slug and screws).

• 1. Preparations

- Wear coat, goggles and gloves
- Prepare a working place with absorbent paper and place cleaned bottles, beakers and tweezers there
- Prepare Alconox cleaning solution (1 % = 10 g per 1l DIW) in a big beaker, preferably using warm DIW
- Label a bottle and fill with the Alconox

• 2. Ultrasonic cleaning with Alconox

- Place the slug/screws in a cleaned beaker and fill the beaker with Alconox until the parts are fully covered
- Fill the UB with DIW at room temperature
- Place the beaker containing the slug/screws in the UB. If possible use a proper holder for the beaker.
- Run the UB for 10 minutes
- Once the time is over, switch off the UB, remove the slug/screws with the help of tweezers and rinse them carefully with DIW
- Place the slug/screws on the counter on a absorbent paper
- Remove the used beaker and the used Alconox solution
- Clean the tweezers with 1% Alconox solution and rinse them with DIW. Then dry them with Kimtech.

• 3. Ultrasonic cleaning with ethanol

- Place the slug/screws with the cleaned tweezers into a cleaned beaker and fill with ethanol until they are fully covered
- Place the clean beaker in the UB and run for 60 minutes
- Clean the tweezers and the used beaker
- Once the time is over, switch off the UB remove the slug/screws with the help of tweezers and rinse them carefully with DIW
- Place the slug/screws on the counter on a clean absorbent paper
- Remove the used beaker and dispose the used ethanol solution
- Clean the tweezers with 1% Alconox solution and rinse them with DIW. Then dry them with Kimtech.
- Change gloves

• 4. Ultrasonic cleaning with DIW

- Place the slug/screws with the cleaned tweezers into a cleaned beaker and fill with DIW until they are fully covered

- Place the clean beaker in the UB and run for 15 minutes
- Clean the tweezers and the used beaker
- Once the time is over, switch off the UB and place the beaker on the counter on clean absorbent paper
- Clean the tweezers with 1% Alconox solution and rinse them with DIW. Then dry them with Kimtech

• 5. Wipe with Alconox

- Prepare a Kimwipe soaked in Alconox
- Hold the slug/screws with tweezers and wipe the surface with Kimwipe soaked in Alconox
- Rinse the slug/screws with DIW and place them on a clean absorbent paper
- Clean the tweezers with 1% Alconox solution and rinse them with DIW. Then dry them with Kimtech

• 6. Wipe with ethanol

- Prepare a Kimwipe soaked in ethanol
- Hold the slug/screws with tweezers and wipe the surface with Kimwipe soaked in ethanol
- Rinse the slug/screws with DIW and place them on a clean absorbent paper
- Clean the tweezers with 1% Alconox solution and rinse them with DIW. Then dry them with Kimtech

• 7. Ultrasonic cleaning with DIW and prepare Citranox solution

- Place the slug/screws with the cleaned tweezers into a cleaned beaker and fill with DIW until they are fully covered
- Place the clean beaker in the UB and run for 15 minutes
- Clean the tweezers and the used beaker
- Change gloves
- Prepare the Citranox solution (1% = 10 g per 1l DIW) with UPW in a cleaned beaker
- Label a bottle and fill with the Citranox solution, place it in the fume hood
- Clean the used beaker
- Change gloves
- Once the UB time is over, remove the container parts with the help of cleaned tweezers and place them on a clean absorbent paper
- Clean the used beaker

• 8. Ultrasonic cleaning with Citranox

- Place the slug/screws in a cleaned beaker with the help of tweezers and fill with Citranox solution until fully covered
- Place the beaker with the slug/screws in the UB

- Run for 15 minutes
- Clean the tweezers
- Take the slug/screws out with the help of tweezers and rinse them with UPW
- Place the slug/screws on a clean absorbent paper
- Clean the tweezers
- Change gloves

- **9. Ultrasonic cleaning with UPW**

- Place the slug/screws into a cleaned beaker with the help of tweezers and fill with UPW until fully covered
 - Place the beaker in the UB and run for 15 minutes
 - Clean the tweezers with UPW
 - Dilute and/or dispose the left Citranox solution
 - Once the UB time is over, remove the container parts with the help of cleaned tweezers, rinse them with UPW and place them on a clean absorbent paper
 - Let the parts dry. If available use an oven to dry
 - Clean all the used material and empty the UB

- **10. Packing of the slug/screws**

- Wear new gloves
 - Wipe PP bag on the inside with Kimwipe soaked in Ethanol
 - Let the bag dry
 - Put the cleaned container parts in the bag
 - Heat seal the opening but leave a small hole
 - Fill the bag with nitrogen, then remove it
 - Fill with nitrogen a second time and immediately seal the bag completely

5 Cleaning procedure for the FFKM O'rings

This procedure should be followed to clean the FFKM O'rings.

- **1. Preparations**

- Wear coat, goggles and gloves
- Prepare a working place with absorbent paper and place cleaned bottles, beakers and tweezers there
- Prepare Alconox cleaning solution (1 % = 10 g per 1 l DIW) in a big beaker, preferably using warm DIW
- Label a bottle and fill with the Alconox

- **2. Rinse with Alconox**

- Put the O'rings into a cleaned beaker with Alconox, rinse them
- Take the O'rings out with tweezers and placed them in a clean beaker filled with DIW
- Clean the tweezers with 1% Alconox solution and rinse them with DIW. Then dry them with Kimtech
- Rinse the O'rings and place them with the help of tweezers on a clean absorbent paper
- Clean the tweezers and beaker with 1% Alconox solution and rinse them with DIW. Then dry them with Kimtech

- **2. Wipe with Alconox**

- Prepare a Kimwipe soaked in Alconox
- Close the wipe around one part of the ring, then pull it through the wipe
- Place the O'rings in a cleaned beaker and rinse with DIW

- **3. Ultrasonic cleaning with Alconox**

- Place the O'rings in a cleaned beaker and fill the beaker with Alconox until the parts are fully covered
- Fill the UB with DIW at room temperature
- Place the beaker containing the O'rings in the UB. If possible use a proper holder for the beaker.
- Run the UB for 10 minutes
- Once the time is over, switch off the UB, remove the O'rings with the help of tweezers and rinse them carefully with DIW
- Repeat the step with UPW
- Place the O'rings on the counter on absorbent paper
- Remove the used beaker and the used Alconox solution
- Clean the tweezers and the beaker with 1% Alconox solution and rinse them with DIW. Then dry them with Kimtech.
- Change gloves

- **4. Ultrasonic cleaning with UPW**

- Place the O'rings with the cleaned tweezers into a cleaned beaker and fill with UPW until they are fully covered
- Place the clean beaker in the UB and run for 10 minutes
- Clean the tweezers
- Once the time is over, switch off the UB and place the beaker on the counter on clean absorbent paper
- Dry each ring with wipes
- Clean the tweezers with 1% Alconox solution and rinse them with DIW. Then dry them with Kimtech

- **5. Packing of the O'rings**

- Wear new gloves
- Wipe PP bag on the inside with Kimwipe soaked in Ethanol
- Let the bag dry
- Put the cleaned container parts in the bag
- Heat seal the opening but leave a small hole
- Fill the bag with nitrogen, then remove it
- Fill with nitrogen a second time and immediately seal the bag completely

Based on: Study and Development of a Scandium Calibration Source for the SNO+ Experiment, Diploma Thesis, Axel Boeltzig, 2013, SNO+-doc-2141-v1, p. 57

References

- [A⁺03] S. Agostinelli et al. *Geant4-a simulation toolkit*. Nuclear Instruments and Methods in Physics Research Section A: Accelerators, Spectrometers, Detectors and Associated Equipment 506 (3): 250, 2003.
- [A⁺08] C. Arpesella et al. *First real time detection of 7Be solar neutrinos by Borexino*. Phys. Lett. B 658 p. 101-108, 2008.
- [A⁺09] E. G. Adelberger et al. *Solar fusion cross sections II: the pp chain and CNO cycles*. 10.1103/Rev. Mod. Phys. 83.195, 2009.
- [A⁺13a] M. Agostini et al. *Results on Neutrinoless Double-beta Decay of ^{76}Ge from Phase I of the GERDA Experiment*. Phys. Rev. Lett. 111.122503, 2013.
- [A⁺13b] B. Aharmim et al. *Combined Analysis of all Three Phases of Solar Neutrino Data from the Sudbury Neutrino Observatory*. American Physical Society, 10.1103/Phys. Rev. C 88.025501, 2013.
- [Alc14] Website Alconox. *Alconox, Critical Cleaning Experts*. <http://wwwalconox.com>, 2014.
- [Ans12] L. Anselmo. *LAB Compatibility Testing*. SNO+-doc-1323-v1, 2012.
- [AWT03] G. Audi, A. H. Wapstra, and C. Thibault. *Atomic Mass Adjustment*. Nuclear Physics A729 p. 337-676, Dec 22, 2003.
- [B⁺00] J. Boger et al. *The Sudbury Neutrino Observatory*. Nucl.Instrum.Meth. A449, 172-207, 2000.
- [Bil13] S. Biller. *SNO+ with Tellurium*. Proceedings of the TAUP2013, Asilomar, California, submitted to Physics Procedia, [arXiv:1405.3401v1], 8-13 Sep 2013.
- [Bir51] J. B. Birks. *The efficiency of organic scintillators*. Proc. Phys. Soc. A64: 874, 1951.
- [BNL14] Website BNL. *Brookhaven National Laboratory, a passion for discovery*. <http://www.bnl.gov>, 2014.
- [Boe13] A. Boeltzig. *Study and Development of a Scandium Calibration Source for the SNO+ Experiment*. Diploma Thesis, 2013.

[Boe14] A. Boeltzig. *TCS correction factors from simulations on a germanium detector*. Private communication, 2014.

[BPG04] J. N. Bahcall and C. Pena-Garay. *Solar models and solar neutrino oscillations*. New J. Phys. 6 63, 2004.

[Cha32] J. Chadwick. *Possible Existence of a Neutron*. Nature p. 312, 1932.

[Che08] M. C. Chen. *The SNO+ Experiment*. 34th International Conference on High Energy Physics, 2008.

[Che11] M. C. Chen. *Solar Neutrino Experiments: Status and Prospects*. Physics of Particles and Nuclei, Volume 42, Issue 4, pp 558-565, July 2011.

[Cit14] Website Citranox. *Citranox, Acid Cleaner and Detergent*. http://wwwalconox.com/resources/StandardDocuments/TB/techbull_citranox.pdf, 2014.

[CUO14] Website CUORE. *CUORE at Berkeley*. <http://cuore.lbl.gov>, 2014.

[D⁺62] G. Danby et al. *Observation of high-energy neutrino reactions and the existence of two kinds of neutrinos*. Phys. Rev. Lett. 9, no. 1, p. 36-44, 1962.

[Dom13] A. Domula. *Drawing of the pressure chamber for the tightness test*. Private communication, 2013.

[DSG14] Website DSG. *Detector Systems GmbH*. <http://www.detector-systems.de>, Aug 2014.

[Dye12] S. Dye. *Geo-neutrinos and the Radioactive Power of the Earth*. Reviews of Geophysics 50, RG3007, 2012.

[F⁺11] R. Ford et al. *SNO+ Scintillator Purification and Assay*. AIP Conf. Proc. 1338, 183, 2011.

[Fer34] E. Fermi. *Attempt of a theory of beta rays (German)*. Zeitschrift für Physik 88, p. 161-177, 1934.

[FG14] N. Fatemi-Ghom. *Neutrinoless double beta decay with SNO+*. <http://neutrino2014.bu.edu>, Poster for Neutrino, 2014.

[Fir99] R. B. Firestone. *Table of Radioactive Isotopes*. <http://ie.lbl.gov>, 1999.

[Gan12] G. Orebi Gann. *Solar Neutrinos at SNO+*. Workshop on The Physics of the Sun and the Solar Neutrinos, LNGS, 8-10 Oct 2012.

[Gas13] L. Gastaldo. *ECHo Experiment*. International School of Nuclear Physics, 35th Course, Erice-Sicily, 16-24 Sep 2013.

[GER14] Website GERDA. *GERDA the GERmanium Detector Array*. <http://www.mpi-hd.mpg.de/gerda/home.html>, 2014.

[GG⁺12] M. C. Gonzalez-Garcia et al. *Global fit to three neutrino mixing: critical look at present precision*. Journal of High Energy Physics, p. 1-24, 2012.

[Gru14] S. Grullon. *Water-based Liquid Scintillator Light Yield and Time Profile Measurements*. Wb-LS LBNE Workshop in Berkeley, May 17, 2014.

[Hel11] R. Helmer. *Progress on SNO+*. Workshop on Double Beta Decay and Neutrinos, Osaka, Japan, 14-17 Nov 2011.

[J⁺56] C. L. Cowan Jr. et al. *Detection of the Free Neutrino: a Confirmation*. Science. 124, Nr. 3212, p. 103-104, 1956.

[Kan14] F. Kandzia. *Data for the energy spectrum of the neutron flux from the neutron source in HZDR*. Private communication, 2014.

[Kod01] K. Kodama. *Observation of Tau Neutrino Interactions*. Phys. Rev. Lett. B 504:218-224, 2001.

[KR13] A.J. Koning and D. Rochman. *TALYS-based Evaluated Nuclear Data Library*. Nuclear Research and Consultancy Group (NRG), Petten, Netherlands, 2013.

[Lan07] C. Lan. *SNO+ and Geoneutrino Physics*. Thesis for the degree Master of Science, Queen's University Kingston, Ontario, Canada, 2007.

[Loz11] V. Lozza. *Scintillator phase of the SNO+ experiment*. Proceedings of the TAUP2011, Munich, Germany, 5-9 Sep 2011.

[Loz14a] V. Lozza. *Neutrinoless double beta decay search with SNO+*. EPJ Web of Conferences 65, 01003, 2014.

[Loz14b] V. Lozza. *The SNO+ Experiment: Overview and Status*. Presentation at DPG Mainz, 24-28 March 2014.

[Mai14] Amélia Maio. *Search for Majorana Neutrinos with the SNO+ detector at SNOLAB*. Talk at Calor, Giessen, Germany, 6-11 Apr 2014.

[Maj37] E. Majorana. *Theory of the Symmetry of Electrons and Positrons (Italian)*. Il Nuovo Cimento, vol. 14, p. 171-184, 1937.

[Mot14] M. Mottram. *SNO+ Experiment Status*. PoS, 524, 2014.

[N⁺06] Sz. Nagy et al. *On the Q-value of the tritium beta-decay*. Europhys. Lett., 74 (3), p. 404, 2006.

[N⁺08] W. Nazarewicz et al. *Low-energy Radioactive Ion Beam Spectroscopy Station (LeRIBSS)*. <http://www.phy.ornl.gov/hribf/equipment/leribss>, 2008.

[Nau11] V. A. Naumov. *Solar neutrinos. Astrophysical aspects*. Physics of Particles and Nuclei Letters Volume 8, Issue 7, pp 683-703, 2011.

[NND14] National Nuclear Data Center NNDc. *Chart of Nuclides*. <http://www.nndc.bnl.gov>, March 2014.

[O'K09] H. O'Keeffe. *Temperature dependent measurement of the density of LAB*. SNO+-doc-276-v1, 2009.

[P⁺75] M. L. Perl et al. *Evidence for Anomalous Lepton Production in e+-e- Annihilation*. Phys. Rev. Lett. 35, no. 22, p. 1489-1492, 1975.

[Pau30] W. Pauli. *Open letter to the radioactives at the Gauverein meeting in Tübingen (German)*. Wissenschaftlicher Briefwechsel mit Bohr, Einstein, Heisenberg u.a., Band II, Springer, Berlin, 1930.

[Pee13] S. Peeters. *Calibration overview talk*. SNO+-doc-1812-v1, 2013.

[PV14] PFAHL-Verbindungstechnik. *Cross dowel, 8x20mm*. <http://pfahl-verbindungstechnik.de>, 2014.

[Sin13a] J. Sinclair. *Optical calibration of SNO+*. High Energy Particle Physics and Astro Particle Physics meeting, Liverpool, 8-10 Apr 2013.

[Sin13b] K. Singh. *Camera System for SNO+*. SNO+-doc-1680-v3, 2013.

[Sin14] K. Singh. *Pictures taken with camera system and underwater light*. SNO+-doc-2507-v1, 2014.

[SMKK90] A. Staudt, K. Muto, and H. V. Klapdor-Kleingrothaus. *Calculation of 2 and 0 Double-Beta Decay Rates*. *Europhys. Lett.* 13 31, 1990.

[SNO14a] Website SNO+. *The SNO+ RAT Companion*. <http://snopl.us/docs/rat/>, 2014.

[SNO14b] Website SNO+. *The SNO+ detector*. <http://snoplus.phy.queensu.ca/About.html>, May 2014.

[Tse11] H. S. Wan Chan Tseung. *Birks constant and alpha quenching factors from bucket*. SNO+-doc-905-v1, 2011.

[vK13] B. v. Krosigk. *Supernova Detection in SNO+ and HALO*. International School of Nuclear Physics, 35th Course, Erice-Sicily, 16-24 Sep 2013.

[vW35] C. F. von Weizsäcker. *Zur Theorie der Kernmassen*. *Zeitschrift für Physik* 96, p. 431458, 1935.

[Was11] O. Wasalski. *Lithium-8 Source*. SNO+ Collaboration Meeting, Seattle, SNO+-doc-788-v1, Feb 2011.

[Wat14] J. Waterfield. *Optical Sources*. Collaboration meeting in SNOLAB, SNO+-doc-2445-v1, 2014.

[Win14] L. Winslow. *Future Neutrinoless Double-Beta Decay Experiments*. Neutrino2014, Boston, 1-7 June 2014.

[Y⁺06] W. M. Yao et al. (*Particle Data Group*). *J. Phys. G* 33, 1, 2006.

[Zub12] K. Zuber. *Neutrino Physics. Second Edition*. CRC press, 2012.

Acknowledgements

I would like to thank all the people that made it possible to write this thesis.

First, I want to thank my supervisor Valentina Lozza. Her constant guidance and effort for numerous suggestions greatly improved this work. I thank Prof. Kai Zuber for the supervision and the possibility to participate in an interesting neutrinoless double beta experiment. I thank Prof. Arno Straessner for reviewing this thesis as second evaluator.

Axel Boeltzig supported me especially in the beginning to get familiar with SNO+ and RAT. The workshop of TUD under the direction of Martin Siegel was very persistent in the execution of our very particular needs of the source container design. The TUD radiation physics group (ASP) provided the chemical laboratory where the cleaning procedures were tested and performed. The simulations were partly done on the PC farm “Atlas” of the center for information services and high performance computing (ZIH) at TU Dresden. I thank Daniel Gehre for the organisation of the neutron irradiation and Uwe Gutsche for the annealing procedure.

My colleagues in the Kinderzimmer, Thomas Wester, Jan Thurn, Birgit Schneider, Stefan Zatschler and Felix Kandzia, I want to thank for the friendly and cooperative working atmosphere.

I thank my family, who were always there whenever I needed a hand. Special thanks go to Maria, who supported me especially during the final parts of this thesis.

Erklärung

Hiermit erkläre ich, dass ich die vorliegende Arbeit eigenständig und ohne unzulässige Hilfe Dritter angefertigt habe. Sämtliche verwendeten fremden Quellen sind als solche kenntlich gemacht. Die Arbeit ist in dieser oder ähnlicher Form bisher keiner anderen Prüfungsbehörde vorgelegt worden.

Marc Reinhard
Dresden, 29.08.2014